

Dissertation

**Phase transitions in strongly
interacting quantum field theories:
QED₃ vs. QCD**

J. A. Bonnet

July 2013

Justus-Liebig University Gießen
Institute For Theoretical Physics

To Helene Gimbel and René P. Bonnet.
To Leona and Lukas Kuhl.
- Nothing is impossible, if you want it. -

Contents

| | |
|---|-----------|
| 1. Introduction | 7 |
| 2. Basic aspects of strongly coupled theories | 11 |
| 2.1. Functional integral formalism in a nutshell | 11 |
| 2.2. Chiral Symmetry | 15 |
| 2.3. Aspects of phase transitions | 17 |
| 2.4. Confinement | 20 |
| 2.5. Dyson–Schwinger Equations | 22 |
| 3. QED₃ in an anisotropic spacetime | 25 |
| 3.1. QED ₃ at zero temperature | 27 |
| 3.1.1. QED ₃ as an effective theory for high-temperature superconductors | 27 |
| 3.1.2. QED ₃ Lagrangian for HTSs | 30 |
| 3.1.3. Dyson–Schwinger equations for anisotropic spacetime | 30 |
| 3.1.4. Numerical Results: The phase diagram of HTS at zero temperatures | 38 |
| 3.1.5. Summary | 45 |
| 3.2. QED ₃ at finite temperature | 47 |
| 3.2.1. Finite temperature DSEs | 47 |
| 3.2.2. Critical Scaling | 49 |
| 3.2.3. Numerical Results | 51 |
| 3.2.4. Summary | 55 |
| 4. Quenched QCD under strong external magnetic fields | 57 |
| 4.1. Formalism | 61 |
| 4.1.1. The Dyson–Schwinger equations of QCD with an external magnetic field | 63 |
| 4.1.2. Chiral condensate | 69 |
| 4.2. The dual condensate from external magnetic fields | 70 |
| 4.2.1. Numerical Results | 74 |
| 4.2.2. Summary | 85 |
| 4.3. Physical Magnetic Field Strengths | 87 |
| 4.3.1. Cutoff Scheme | 87 |
| 4.3.2. Numerical Results at zero T | 87 |
| 4.3.3. Summary | 89 |
| 5. Conclusions and Outlook | 91 |
| A. Aspects of QED₃ | 97 |
| A.1. Derivation of the QED ₃ Lagrangian | 97 |

| | |
|--|------------|
| A.2. Renormalization Point Dependencies in QED ₃ | 102 |
| A.3. QED ₃ :Anisotropic N_f^c in the Pisarski approximation | 103 |
| B. Aspects of QCD | 105 |
| B.1. Ritus' method for the quark propagator | 105 |
| B.2. The dressed quark propagator | 107 |
| B.3. The Dyson Schwinger equation in an external magnetic field | 108 |

1. Introduction

Strongly coupled systems are realized in a variety of physical situations. From superconductors, ultra cold quantum gases and neutron stars to heavy-ion collisions and the quark-gluon plasma, strong correlations between the respective degrees of freedom play a crucial *rôle* in understanding these scenarios. They give rise to nonperturbative phenomena such as for instance the dynamical generation of mass or the condensation of particles into bound states.

The tools for this analysis are nonperturbative methods such as the lattice gauge theory framework, functional methods, effective models or AdS/CFT approaches. Each of these approaches has its advantages and at the same time struggles with its characteristic drawbacks. As an example, lattice gauge theory has the great advantage to deal with the elementary degrees of freedom without loss of information. However, QCD investigations are limited to small baryon chemical potentials due to the notorious sign problem. QED_3 investigations are hampered because of the large separation of scales that needs large simulation volumes and is technically difficult at large numbers of fermion flavors. The Dyson–Schwinger approach also deals with the elementary degrees of freedom but suffers from the necessity to truncate the tower of coupled equations. Similar pros and cons also hold for other functional methods as the functional renormalization group method (FRG) or effective models such as the (Polyakov-)quark-meson model or the Nambu–Jona-Lasinio model. AdS/CFT approaches perturbatively investigate the weakly coupled limit of dual theory to QCD, respectively QED_3 . Altogether, it is desirable to attack problems from different perspectives and to obtain the bigger picture from complementary information. In the following, we will employ the Dyson–Schwinger method for our investigations. For an overview of Dyson–Schwinger equations and their application to strongly coupled theories, see [1–5].

This work concentrates on two strongly coupled quantum field theories: QCD and QED_3 . QCD is an integral constituent of the Standard Model and widely believed to be the underlying theory to the strong interaction between quarks and gluons. QED in two spatial and one temporal dimension, QED_3 , on the other hand was seen for a long time as a toy model for higher dimensional, 'more realistic' theories. However, the application as a low-energy effective theory for condensed matter systems helped to accentuate the variety of interesting properties of this theory for its own sake.

QED_3 and QCD might be considered rather diverse at the first glance, not least because of their Abelian, respectively non-Abelian nature. A closer look shows however that they share several features in common. The first is the displaying of chiral symmetry breaking by the dynamical generation of a fermionic mass. This mass serves as an order parameter to analyze the transition from chirally symmetric to the chirally broken phase under the variation of external parameters. Furthermore, both theories are asymptotically free. This feature of QCD is well-known since Gross, Politzer and Wilczek [6, 7] and allows access to QCD at high

energies via perturbative calculations. Although QED_3 has an *a priori* dimensionful coupling, it is asymptotically free in an RG sense, since it is possible to define a dimensionless (decreasing) running coupling with help of the gauge boson vacuum polarization. Speaking of the running coupling and asymptotic freedom, it is well known that QCD loses its asymptotic freedom when the number of fermion flavors is increased up to a critical number $N_{f,cr}^{a.f.}$. However, before this critical number is reached, there have been many arguments that QCD passes a conformal phase. This phase is separated by another critical number of fermion flavors $N_{f,cr}^{conf.}$ from the chirally broken phase. The range $N_{f,cr}^{conf.} < N_f < N_{f,cr}^{a.f.}$ was coined the 'conformal window' and is in itself a phase of high interest. On the one hand this interest arises due to the sensitivity of the conformal window to beyond standard model physics [8]. On the other hand, the lower transition from the chirally broken to the conformal phase gives rise to quantum critical scaling and has been analyzed in a number of works. Considering QED_3 under variation of the number of fermion flavors, several authors [9–11] argued that QED_3 displays an analogous behavior: Before losing asymptotic freedom, a so-called pseudo conformal phase emerges ('pseudo' due to the dimensionful coupling).

A third feature in common is confinement in the quenched approximation (neglect of quark loops in the gauge sector). However, the confinement in QED_3 is purely an issue of dimensionality (a heuristic argument can be found in *e.g.* [12]). In contrast, the mechanisms of confinement in QCD are suspected to have their origin in the topological structure of the theory (confinement by instantons, for a review see [13]) and are intensely debated.

Finally, we would like to point out that the experimental situation motivates the investigation of both theories under the aspect of inherent anisotropies. In the case of QED_3 , these anisotropies are motivated from condensed matter systems, in this case high temperature superconductors (HTSs). They arise from the anisotropic crystalline structure surrounding the superconducting plane. This results in an effective modification of the underlying spacetime. In QCD, the anisotropy is of a different nature and arises from external magnetic fields, realized for instance in heavy-ion collisions. The presence of the magnetic field destroys the translational invariance of the quark propagator. However, in this case, this does not mean that the spacetime itself is modified.

This thesis is naturally divided into two parts. These are organized as follows. Part I deals with QED_3 in an anisotropic spacetime as an effective low-energy theory for high temperature superconducting materials. We analyze the chiral phase transition at zero temperature under the influence of finite anisotropies of arbitrary sizes. At finite temperatures, we additionally investigate the scaling behavior close to the merger of the thermal phase transition line and the quantum critical point at zero temperature. The discussion of QED_3 can be found in chapter 3.

Part II reports about the investigations of three-color QCD under the influence of strong external magnetic fields. We perform our analysis under two main aspects: Firstly, we employ extremely strong magnetic fields as a probe for the string tension between two static quarks. We therefore strive to access a new observable for confinement in the framework of Dyson–Schwinger equations. Secondly, we study the effects of strong, but physically realized magnetic fields on chiral symmetry breaking at zero and finite temperatures. We present these investigations in chapter 4. In order to review the most important basic aspects of strongly coupled gauge theories, we prepend an introductory chapter to the two parts of this thesis.

Through this thesis, we will provide more introductory notes on the subject in focus. Furthermore, we will present only the most essential details of the investigated frameworks in chapter 3 and 4 and rather allow the presentation of our results to be in the center. Detailed derivations are collected in the appendices A and B.

2. Basic aspects of strongly coupled theories

In this chapter, we review some selected basic quantities and concepts that are essential to the following discussion. More aspects follow in a suited position in chapters 3 and 4. For more general information on basic quantities, we refer the reader to textbooks such as [14–18].

2.1. Functional integral formalism in a nutshell

The central quantity of quantum statistical field theory is the generating functional Z . It represents the analogous quantity to the classical partition function and contains the complete information of a given theory. The generating functional depends on the sources and is in Euclidean spacetime given by

$$Z[J(x)] = \int \mathcal{D}\Phi(x) \exp\left(-S(\Phi(x)) + \int d^d x' J(x') \cdot \Phi(x')\right), \quad (2.1)$$

in d -dimensional spacetime. Here, we employ the compact superfield notation for the sources J and the field variables Φ , *i.e.* the superfields are generalized field variables containing all fields and their associated source fields of a theory. For instance for QED, the superfield is given by $\Phi = (\bar{\psi}, \psi, A_\mu)^T$ with the fermion (antifermion) spinors ψ ($\bar{\psi}$) and the Abelian gauge field A_μ and $J = (\eta, \bar{\eta}, j_\mu)^T$ with the Grassmannian source fields η and $\bar{\eta}$ for the spinor fields and the source j for the gauge field. The path integral measure in the superfield notation is accordingly given by $\mathcal{D}\Phi(x) = \mathcal{D}\bar{\psi}\mathcal{D}\psi\mathcal{D}\mathcal{A}\dots$. Furthermore, $S(\Phi)$ denotes the classical action and is given by the d -dimensional spacetime integral over the Lagrangian, $S(\Phi) = \int d^d x \mathcal{L}(\Phi)$.

We will specify the field content and the form of the classical action separately for QED₃ and QCD below. In general, it is possible to compute the n -point functions of a theory from the generating functional, via functional derivatives with respect to the source fields,

$$\frac{\delta^n Z[J]}{\delta J_{i_1}(x_1) \dots \delta J_{i_n}(x_n)} = \langle \Phi_{i_1}(x_1) \dots \Phi_{i_n}(x_n) \rangle_J, \quad (2.2)$$

However, the n -point function on the right hand side of Eq. (2.2) contains redundant information in form of vacuum bubbles, and reducible diagrams. For practical purposes, it is helpful to define the Schwinger functional,

$$\mathcal{W}[J] = \ln Z[J]. \quad (2.3)$$

that generates only the connected Green's functions. A further reduction of redundancies is obtained by a Legendre transform of the Schwinger functional, finally leading to the generating functional of the 1PI-connected Green's functions [19]: the quantum effective action.

It is given by

$$\Gamma[\phi] = \sup_J \left\{ \int d^d x J(x) \phi(x) - \mathcal{W}[J] \right\}, \quad (2.4)$$

with the classical (super)field $\Phi_{cl}(x) = \langle \Phi(x) \rangle := (\langle \bar{\psi} \rangle, \langle \psi \rangle, \dots)^T$. From the quantum effective action, 1PI-connected n -point functions can be obtained via functional derivatives with respect to the classical fields $\Phi_{cl}(x)$ and subsequently setting the sources to zero. For instance, the propagator of the fields Φ_i and Φ_j is derived from the quantum effective action by

$$G_{ij}^{-1}(x, y) = \left. \frac{\delta^2 \Gamma[\Phi]}{\delta \Phi_{cl,i}(x) \delta \Phi_{cl,j}(y)} \right|_{J=0}. \quad (2.5)$$

We will come back to this point in section 2.5, when discussing the Dyson–Schwinger equations.

Generating functional of QED₃

The Lagrangian for isotropic QED in (2+1) dimensional Euclidean spacetime is given by

$$\mathcal{L}_{QED3} = N_f \bar{\psi} \left\{ \sum_{\mu=0}^2 \gamma_{\mu} (\partial_{\mu} + i e a_{\mu}) \right\} \psi - \frac{1}{4} F_{\mu\nu}^2, \quad (2.6)$$

where ψ and $\bar{\psi}$ denote spin-1/2 four spinors, a_{μ} the gauge boson fields and γ_{μ} the Dirac matrices. The field strength tensor is given by $F_{\mu\nu} = \partial_{\mu} a_{\nu} - \partial_{\nu} a_{\mu}$, with $\mu, \nu \in \{0, 1, 2\}$. We will come back to the discussion of the fermionic and the gauge boson fields in chapter 3. For now, we need to clarify the representation of the Dirac γ -matrices. We therefore consider the underlying Clifford algebra,

$$\{\gamma_{\mu}, \gamma_{\nu}\} = 2\delta_{\mu\nu} \mathbb{1}_{4 \times 4}. \quad (2.7)$$

With the minimum number of matrices, one can find a two dimensional representation which is given by the Pauli spin matrices

$$\sigma_1 = \begin{pmatrix} 0 & 1 \\ 1 & 0 \end{pmatrix}, \quad \sigma_2 = \begin{pmatrix} 0 & -i \\ i & 0 \end{pmatrix}, \quad \sigma_3 = \begin{pmatrix} 1 & 0 \\ 0 & -1 \end{pmatrix}. \quad (2.8)$$

However, in the minimal representation, there is no way to realize chiral symmetry, since there is no other matrix anticommuting with the Pauli-matrices above (except for the (trivial) unity matrix). We therefore need the next higher dimensional representation of the γ -matrices for the investigations of chapter 3. The four dimensional matrices are given by:

$$\gamma_0 = \begin{pmatrix} \sigma_3 & 0 \\ 0 & -\sigma_3 \end{pmatrix}, \quad \gamma_1 = -i \begin{pmatrix} \sigma_1 & 0 \\ 0 & -\sigma_1 \end{pmatrix}, \quad \gamma_2 = -i \begin{pmatrix} \sigma_2 & 0 \\ 0 & -\sigma_2 \end{pmatrix}. \quad (2.9)$$

Now, two additional matrices can be found that anticommute with $\gamma_0, \gamma_1, \gamma_2$ and with each other. They are denoted by γ_3 and γ_5 and read

$$\gamma_3 = i \begin{pmatrix} 0 & \mathbb{1} \\ \mathbb{1} & 0 \end{pmatrix}_{4 \times 4}, \quad \gamma_5 = i \begin{pmatrix} 0 & -\mathbb{1} \\ \mathbb{1} & 0 \end{pmatrix}_{4 \times 4}, \quad (2.10)$$

Finally, the commutator $[\gamma_3, \gamma_5] = \gamma_{35}$ defines another matrix that commutes with γ_3 and with γ_5 , but anticommutes with all other matrices. However, the associated mass term, $m \bar{\psi}(x) [\gamma_3, \gamma_5] \psi(x)$, does not respect parity invariance. Therefore, we will neglect this term in the further discussions. Nevertheless, these additional commutation relations define the Lie algebra

$$[\gamma_l, \gamma_m] = i \epsilon_{lmn} \gamma_n \quad \text{with } l, m, n \in \{3, 5, 35\}, \quad (2.11)$$

that forms a $SU(2)$ gauge group, when including a factor of $\frac{1}{2}$ into the definition of the matrices given in eq. (2.10). Thus, γ_{35} has to be taken into account at this point. Notice that the choice of the Clifford algebra that is imposed on the γ -matrices is not necessarily defined as in eq. (2.7). For example in [20], a different algebra is used.

With the Lagrangian fully defined, we proceed with the generating functional for QED_3 which is given by

$$Z_{QED_3}[\bar{\eta}, \eta, j] = \int \mathcal{D}[\bar{\psi}\psi a] \exp\left(-S(\bar{\psi}\psi, a) + \int d^3x' (\bar{\psi} \cdot \eta + \bar{\eta} \cdot \psi + j \cdot a)\right). \quad (2.12)$$

We introduced the Grassmann-valued sources $\bar{\eta}, \eta$ for the fermions, and the source j for the gauge bosons. The classical action $S(\bar{\psi}, \psi, a)$ is given by $\int d^3x' \mathcal{L}_{QED_3}$, with \mathcal{L}_{QED_3} defined in Eq. (2.6).

The generating functional in the form of 2.12 is plagued by a divergent functional integral that has its origin in the presence of gauge-equivalent modes on the gauge orbits defined by $a_\mu \rightarrow a_\mu + \frac{1}{e} \partial_\mu \alpha(x)$. The divergences can be removed with the help of the Faddeev-Popov gauge fixing procedure [21], that selects only the physical subspace of all gauge gauge configurations by allowing one gauge configuration per gauge orbit. This procedure leads to the gauge-fixed generating functional in the form of

$$Z_{QED_3}^{gf}[\bar{\eta}, \eta, j] = \mathcal{N}(\xi) \det\left(\frac{1}{e} \partial^2\right) \int \mathcal{D}\alpha Z_{QED_3}[\bar{\eta}, \eta, j] \exp\left(\int d^3x \frac{1}{2\xi} (\partial_\mu a_\mu)^2\right), \quad (2.13)$$

with a gauge dependent normalization $\mathcal{N}(\xi)$ and the Faddeev–Popov determinant¹ $\left(\frac{1}{e} \partial^2\right)$. Remember that in the actual calculation of correlation functions, the additional constant factors cancel with the normalization in the denominator. The remainder of the gauge fixing procedure is the gauge parameter ξ . We will further specify our choice of gauge in section 3.1.3.

Speaking of divergences, one last point remains to be discussed: the renormalized Lagrangian. Since QED_3 is a superrenormalizable theory and there are no UV divergences present. It is nevertheless possible to introduce renormalization constants for the fermion wave function Z_2 and for the gauge boson Z_3 , without changing the physical information of the theory. For completeness, the vertex renormalization constant $Z_1 = Z_2$ by means of the Ward-Takahashi identity. We will come back to the renormalization constants when discussing our truncation schemes for the Dyson–Schwinger equations.

¹for linear covariant gauge conditions $G(a) = \partial_\mu a_\mu - \bar{\alpha}(x)$, with any scalar function $\bar{\alpha}(x)$.

Generating functional of QCD

The generating functional for QCD₄ in Euclidean spacetime is given by

$$Z_{QCD}[\mathcal{J}, \eta, \bar{\eta}] = \int \mathcal{D}[\psi \bar{\psi} \mathcal{A}] \exp \left\{ - \int d^4x \left[\bar{\psi}(\mathcal{D} + m)\psi + \frac{1}{4} \mathcal{F}_{\mu\nu}^2 \right] + \int d^4x (\mathcal{A}_\mu^a \mathcal{J}_\mu^a + \bar{\eta}\psi + \bar{\psi}\eta) \right\}, \quad (2.14)$$

with the four-spinors ψ and $\bar{\psi}$ representing the quarks in fundamental representation. The non-Abelian gauge field \mathcal{A}_μ^a is given in adjoint representation and describes the gluonic degrees of freedom. The color indices are restricted to $a, b, c \in 1, 2, \dots, 8$. We further introduced Grassmann valued sources η and $\bar{\eta}$ for the quarks and the source \mathcal{J}_μ for the gluons. The covariant derivative in the fundamental representation is given by $\mathcal{D} = \gamma_\mu(\partial_\mu + ig\mathcal{A}_\mu)$, with the gauge coupling g and the gluon field $\mathcal{A}_\mu = \mathcal{A}_\mu^a t^a$. The generators t^a of the gauge group $SU(N_c = 3)$ form the Lie algebra $[t^a, t^b] = if^{abc}t^c$, with the structure constants of $SU(N_c)$ denoted by f^{abc} . Furthermore, the field strength tensor of the gluons reads

$$\mathcal{F}_{\mu\nu}^a = \partial_\mu \mathcal{A}_\nu^a - \partial_\nu \mathcal{A}_\mu^a - gf^{abc} \mathcal{A}_\mu^b \mathcal{A}_\nu^c. \quad (2.15)$$

Finally, the Dirac γ matrices obey the Clifford algebra

$$\{\gamma_\mu, \gamma_\nu\} = 2\delta_{\mu\nu} \mathbb{1}_{4 \times 4}. \quad (2.16)$$

Similar to QED₃, the path integral over all gauge field configurations in the generating functional in Eq. (2.15) contains an infinite number of gauge equivalent field configurations that need to be accounted for. However, in contrast to QED₃, the Faddeev–Popov gauge fixing prescription no longer cures this problem entirely. Gribov [22] firstly noticed that for non-Abelian fields, the gauge fixing condition is not unique due to topology of the gauge field configuration space. In consequence, multiple gauge configurations per gauge orbit remain also after the Faddeev–Popov gauge fixing procedure, the so-called Gribov copies. Since there is an arbitrary number of Gribov copies per gauge orbit, the original problem of divergences is not completely resolved². However, we know from lattice calculations that only deep infrared results are affected by Gribov copies³ [24], which is not relevant for the energy range we will investigate. We therefore retreat to the Faddeev–Popov gauge-fixed generating functional, which is given by

$$Z_{QCD}[\mathcal{J}, \eta, \bar{\eta}, \sigma, \bar{\sigma}] = \int \mathcal{D}[\psi \bar{\psi} \mathcal{A} c \bar{c}] \exp \left\{ - \int d^4x \left[\bar{\psi}(\mathcal{D} + m)\psi + \frac{1}{4} \mathcal{F}_{\mu\nu}^2 + \frac{(\partial_\mu \mathcal{A}_\mu)^2}{2\xi} - i\partial_\mu \bar{c} D_\mu c \right] + \int d^4x (\mathcal{A}_\mu^a \mathcal{J}_\mu^a + \bar{\eta}\psi + \bar{\psi}\eta + \bar{\sigma}c + \bar{c}\sigma) \right\}, \quad (2.17)$$

where ξ again denotes the gauge parameter. In the gauge fixing procedure, the Faddeev–Popov determinant was rewritten in terms of a functional integral over the ghost fields c and

²For a pedagogical discussion of Gribov copies in a toy model, the interested reader is referred to [23].

³Since we will work in Landau gauge that is not a Gribov-copy free gauge.

\bar{c} with the sources $\bar{\sigma}$ and σ . The QCD investigations presented in chapter 4 are performed in Landau gauge, *i.e.* $\xi = 0$.

Furthermore, to obtain the renormalized QCD Lagrangian, we introduce the renormalization 'constants',

$$\begin{aligned}
 Z_m : \quad m &\rightarrow Z_m m && \text{for the mass renormalization,} \\
 Z_2 : \quad \psi &\rightarrow \sqrt{Z_2} \psi && \text{for the fermion wave function renormalization,} \\
 Z_3 : \quad \mathcal{A}_\mu^a &\rightarrow \sqrt{Z_3} \mathcal{A}_\mu^a && \text{for the gluon renormalization,} \\
 \tilde{Z}_3 : \quad c, \bar{c} &\rightarrow \sqrt{\tilde{Z}_3} c, \bar{c} && \text{for the ghost renormalization,} \\
 Z_g : \quad g &\rightarrow Z_g g && \text{for the coupling renormalization.}
 \end{aligned}$$

Additional renormalization constants are needed for the vertices. However, these are related to the above introduced renormalization constants via Slavnov-Taylor identities for the vertices:

$$\begin{aligned}
 Z_1 &= Z_g Z_3^{3/2} && \text{for the three gluon vertex} \\
 Z_4 &= Z_g^2 Z_3^2 && \text{for the four gluon vertex} \\
 \tilde{Z}_1 &= Z_g \tilde{Z}_3 \sqrt{Z_3} && \text{for the ghost gluon vertex} \\
 Z_{1F} &= Z_g Z_2 \sqrt{Z_3} && \text{for the quark gluon vertex.}
 \end{aligned}$$

Not all of these will play a *rôle* in the following investigations, as will become clear when specifying our truncation scheme in chapter 4.1.

2.2. Chiral Symmetry

From the physical point of view, symmetries are the governing concepts of nature. By analysis of manifest, hidden or broken symmetries, we categorize and understand a broad range of problems.

Chiral symmetry is the invariance under a set of $U(N_f)$ transformations that distinguish between left- and right handed particles. It is broken by the presence of fermionic mass terms, explicitly inserted or dynamically generated, or by anomalies. The dynamical generation of a mass term depends on numerous conditions, for instance on temperature (in QED₃ and QCD) and baryon chemical potential (in QCD). Besides these, one can think of a number of other parameters that could influence the breaking of chiral symmetry. In this thesis, besides the 'classical' parameters such as temperature, we focus on external conditions such as an external magnetic field in QCD and a material's anisotropy in QED₃.

We shortly introduce the realization of chiral symmetry in both theories.

Chiral symmetry in QED₃

In general, QED₃ contains N_f fermion flavors (N_f kinds of spinors, see Eq. (2.6)), leading to an overall symmetry of the Lagrangian in four dimensional spinor representation given by

$$U(N_f) \times SU(2N_f) \simeq U(2N_f), \tag{2.18}$$

with the $U(N_f)$ symmetry generated by the unity matrix. In section 2.1, we made sure to chose a representation of the Dirac matrices that allow for the presence of chiral symmetry and its breaking. The associated chiral-like transformations are given by

$$\psi \rightarrow e^{i\gamma_5\alpha}\psi \quad (2.19)$$

$$\psi \rightarrow e^{i\gamma_3\alpha}\psi, \quad (2.20)$$

with the matrices γ_3 and γ_5 defined in Eq. (2.10). The transformations are chiral-like as they each have a related Noether current that is conserved if the ψ -associated mass term vanishes. This can easily be seen considering for example the current

$$j^{\mu 3}(x) = \bar{\psi}(x)\gamma^\mu\gamma^3\psi(x) \text{ for } \mu = 0,1,2. \quad (2.21)$$

Since the matrices γ^3 and γ^μ anticommute, the derivative of the current is given by

$$\begin{aligned} \partial_\mu j^\mu &= (\partial_\mu \bar{\psi}(x))\gamma^\mu\gamma^3\psi(x) - \bar{\psi}(x)\gamma^3\gamma^\mu(\partial_\mu\psi(x)) \\ &= m\bar{\psi}(x)\gamma^3\psi(x) + m\bar{\psi}(x)\gamma^3\psi \\ &= 2m\bar{\psi}(x)\gamma^3\psi(x), \end{aligned} \quad (2.22)$$

and thus the current is only conserved if $m = 0$. Any mass term in the theory, no matter if introduced explicitly or dynamically generated, necessarily breaks the Lagrangian's chiral symmetry

$$U(2N_f) \rightarrow U(N_f) \times U(N_f) \times SU(N_f) \times SU(N_f). \quad (2.23)$$

Chiral symmetry in QCD

The fermionic part of the four dimensional QCD Lagrangian without explicit mass terms separates in left- and right handed particles. Considering only the two lightest quarks, up (u) and down (d), the underlying

$$U(N_f = 2)_L \times U(2)_R \quad (2.24)$$

symmetry is isomorphic to

$$SU(2)_L \times SU(2)_R \times U(1)_V \times U(1)_A. \quad (2.25)$$

However, since the $U(1)_V$ is associated with baryon number conservation and the $U(1)_A$ is anomalously broken, the $SU(2)_L \times SU(2)_R$ symmetry represents the relevant part of the $U(2) \times U(2)$ symmetry for the following discussion.

The left- and right handed quark doublet is obtained from the projection

$$Q_L = \left(\frac{1-\gamma^5}{2}\right)\begin{pmatrix} u \\ d \end{pmatrix} \quad Q_R = \left(\frac{1+\gamma^5}{2}\right)\begin{pmatrix} u \\ d \end{pmatrix}. \quad (2.26)$$

If chiral symmetry is present, they are invariant under transformations of the form

$$\psi \rightarrow e^{i\gamma_5\alpha}\psi. \quad (2.27)$$

The associated conserved axial currents with an implicit sum over left- and right handed quarks are given by

$$j^{\mu 5} = \bar{Q} \gamma^\mu \gamma^5 Q \quad \text{and} \quad j^{\mu 5a} = \bar{Q} \gamma^\mu \gamma^5 \tau^a Q.$$

If one introduces fermionic mass terms into the Lagrangian, the $SU(2)_A$ part of the $SU(2)_L \times SU(2)_R$ symmetry is broken. Thus, spontaneous chiral symmetry breaking is described by

$$SU(2)_L \times SU(2)_R \rightarrow SU(2)_V. \quad (2.28)$$

Order parameters for chiral symmetry

In its general definition, an order parameter indicates the breaking of a symmetry, that is the transition between two phases. In the strict sense, the order parameter vanishes in one phase and has a finite value in the other.

An order parameter for chiral symmetry breaking is the dynamically generated fermion mass. If no explicit fermion mass terms are present on the level of the Lagrangian, it is chirally symmetric. As soon as fermion masses are generated dynamically, this symmetry is broken, as discussed above for the cases of QED_3 and QCD.

The dynamically generated fermion mass is a nonperturbative effect, resulting from the fermion-gauge boson interactions, and will be discussed extensively in the following chapters. For now, we consider the general form of a dressed fermion propagator in four dimensions in an isotropic spacetime. The propagator is given by

$$S_F(p) = \frac{B(p) - iA(p)\not{p}}{B^2(p) + A^2(p)p^2}, \quad (2.29)$$

with the scalar fermion dressing function $B(p)$ and the vectorial dressing function $A(p)$. The RG-invariant, momentum dependent fermion mass is given by the combination $M(p) = B(p)/A(p)$. However, already at this point it is obvious that the scalar fermion dressing function can serve as an order parameter for chirally symmetry breaking: for vanishing $B(p)$, also the RG-invariant mass vanishes and the theory is in the chiral symmetric phase. For finite $B(p)$, also $M(p)$ is finite and chiral symmetry is broken. We will investigate the scalar fermion dressing function as an order parameter for chiral symmetry breaking in QED_3 in chapter 3.

Another order parameter is the chiral condensate, $\langle \bar{\psi}\psi \rangle$, that is obtained from the Dirac trace over the fermion propagator and describes the affinity of the vacuum to create a fermion-antifermion pair. Since we will only employ the chiral condensate as an order parameter in chapter 4, we will provide a more detailed discussion in chapter 4.1.2.

2.3. Aspects of phase transitions

Understanding the transition between strongly coupled phases of a given theory is a formidable task. In general, one distinguishes first order phase transitions, that have a discontinuous change in the order parameter. Another group is formed by the continuous phase transitions. In this case, it is the n th derivative of the order parameter with respect to some critical quantity that develops a discontinuity.

An outstanding feature of continuous phase transitions is the behavior of the order parameters near the critical point that allows the grouping into universality classes. It can be described by power-laws with the same critical exponent for phase transitions belonging to the same universality class.

We will come back to the behavior close to a quantum critical point in chapter 3.2. For now, we turn our attention to a special group of continuous phase transitions, the conformal phase transitions.

(Pseudo) conformal phase transitions

There has been the proposal that the chiral phase transition in N_f in QED₃ belongs to a subclass of continuous phase transitions, the conformal phase transitions (CPTs). We will summarize the most important points of such a phase transition and follow along the lines of [9, 10].

CPTs are characterized by several remarkable features that clearly distinguish them from other continuous phase transitions: The behavior of the order parameter in the critical region and the kind of spectrum of light excitations in the symmetric and non-symmetric phase.

In more detail, the behavior of an order parameter X in the critical region can be described by

$$X \sim f(z), \quad (2.30)$$

where z is the quantity that can become critical. For general second order phase transitions, f is of the general form

$$f \sim (z - z_c)^\nu, \quad (2.31)$$

where $\nu > 0$.

For CPTs in contrast, the function f exhibits a different behaviour in the critical region, namely

$$f \sim \exp\left(\frac{a}{(z_c - z)^\nu}\right), \quad (2.32)$$

where again, $\nu > 0$ and a is a constant.

The conditions for a CPT are now fulfilled, if the function f contains an essential singularity in the way that

$$\lim_{z \searrow z_c} f(z) = 0 \quad (2.33)$$

$$\lim_{z \nearrow z_c} f(z) \neq 0, \quad (2.34)$$

where $z \nearrow z_c$ denotes that z approaches z_c from the symmetric phase, while $z \searrow z_c$ means that z is approaching from the non-symmetric phase. The continuity of the phase transition is guaranteed since the limit from the non-symmetric side goes to zero, including a vanishing order parameter. In the symmetric phase, the order parameter is zero anyway (remember e.g. the chiral symmetric phase).

Notice, that the scaling behavior Eq. (2.32) has also been found in two dimensional models, where it was coined the ‘‘Berezinskii–Kosterlitz–Thouless’’ (BKT) phase transition [25–27]. The underlying mechanism of the BKT phase transition was found to be the struggle between the entropy of a single vortex and the binding energy of a vortex pair that finally leads

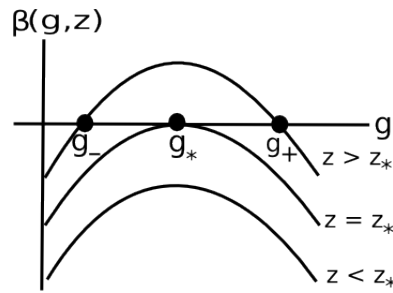


Figure 2.A: The β function for a toy model with coupling g and external parameter z . Critical values have the subscript “*“. The fixed points are indicated with a dot.

to a vortex condensation. In the derivation of the QED₃ Lagrangian, it will become clear that a similar competition is also responsible for the phase transition taking place in high temperature superconductors.

As for the relevance of the conformal phase transitions for this work, we need to mention that QED₃, similar to many-flavor QCD, is a candidate theory to contain a pseudo-CPT, respectively a CPT. The prefix ‘pseudo’ in the case of QED₃ is in order as the conformal symmetry is broken in both, the chirally symmetric and the chirally broken phase. In the massive phase, conformal symmetry is broken anyway by the mass term. In the chirally symmetric phase, the dimensionful coupling of QED₃ breaks the conformal symmetry. With respect to the second distinguishing feature of CPTs, the spectrum of light excitations, we add that QED₃ is super-renormalizable (contains only a finite number of divergent Feynman-diagrams) and UV-divergences in principle can be removed. Nevertheless, one can observe an abrupt change in the spectrum of light excitations at the critical point, as argued in [9, 10].

We will come back to the pseudo conformal nature of the chiral phase transition and the scaling property close to the quantum critical point in chapter 3.2.

Phase transitions and fixed points

The critical points of second order phase transitions, *e.g.* of the previously discussed CPTs, can be identified with fixed points of according RG-equations [28]. The analysis of flow equations further helps not only to locate a critical point, but also to understand the quantum critical behavior, *i.e.* the critical scaling in its vicinity. Critical scaling is characterized by critical exponents. These allow to group theories into universality classes, that is, theories with the same critical exponents and therefore the same critical behavior.

One of the outstanding features of (pseudo)conformal phase transitions is the scaling behavior approaching the quantum critical point from the chirally broken phase. The exponential Miransky- or generalized BKT scaling can be understood in terms of fixed point mergers, as was argued by [29, 30].

We follow [30] in illustrating the emergence of BKT/Miransky scaling from the fixed point dynamics in a simplistic toy model. For this, we assume a dimensionless coupling g for convenience. The theory may depend on some external parameter z that can become critical.

The β -function is of the form

$$\beta(g; z) = \frac{\partial g}{\partial t} = (z - z_*) - (g - g_*)^2, \quad (2.35)$$

with the critical values indicated by subscript “*” and $t = \ln \mu$, where μ denotes the renormalization scale. One can calculate the fixed points of the coupling in the parameter range $(z - z_*) > 0$ via the zeroes of the β function. This leads to an IR and a UV stable fixed point marking the transition to a conformal phase. They are given by

$$g_{\pm} = g_* \pm \sqrt{(z - z_*)}. \quad (2.36)$$

It is now clear from Eq. (2.36) that the appearance and the number of fixed points depends on the value of the critical parameter z . With $z \rightarrow z_*$, the two fixed points approach each other until they merge at $g_+ = g_- = g_*$ for $z = z_*$. Further decreasing z , thus leading to complex solutions for Eq. (2.36), results in the loss of the conformal phase.

To recover the exponential scaling, we consider the external parameter to be in the vicinity of its critical value in the symmetric phase, $z \lesssim z_*$, and the coupling at some initial UV scale $g_{UV} < g_*$. We obtain the scaling relation from integrating the β function Eq. (2.35), leading to

$$\frac{\Lambda_{IR}}{\Lambda_{UV}} = \exp \left(\int_{t_{UV}}^{t_{IR}} dt \right) = \exp \left(\int_{g_{UV}}^{g_{IR}} \frac{dg}{\beta(g; z \lesssim z_*)} \right) \quad (2.37)$$

$$\approx \exp \left(-\frac{\pi}{\sqrt{(z_* - z)}} \right). \quad (2.38)$$

The approximation in the last step includes the assumption that $|g_{IR,UV} - g_*| \gg |z - z_*|$, for which we can replace the arctan emerging from the integration by $\pi/2$.

Similar arguments as for this toy model also hold for many-flavor QCD and QED₃. Here, the critical parameter is the number of fermion flavors. Before the critical number of fermions for the loss of asymptotic freedom is reached, an infrared stable fixed point separates another phase: the (pseudo)conformal window. This so-called Caswell-Banks-Zaks fixed point [31, 32] governs the conformal dynamics and is destabilized for smaller and smaller numbers of fermion flavors by the onset of chiral symmetry breaking. This lower end of the pseudo conformal window in QED₃ will be analyzed in section 3.2.

2.4. Confinement

Besides chiral symmetry breaking, confinement is another central nonperturbative phenomenon of QCD. However, in contrast to the above discussed clear definition of chiral symmetry, confinement is a much more debated subject. There exist several notions of confinement in the literature, that can basically be divided into the two scenarios of color confinement and quark confinement. For the scenario of color confinement, the absence of free color charges from the spectrum of physical particles is central. According criteria for color confinement

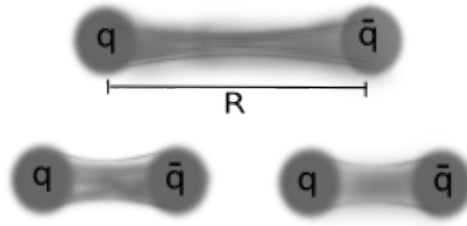


Figure 2.B: Sketch of a quark-antiquark pair separated by a distance R (upper panel) connected by a color flux tube and after string breaking with another quark-antiquark pair generated (lower panel).

are the Kugo–Ojima [33] and the Gribov–Zwanziger [34] confinement criteria, that represent constraints for the form of the gluon and ghost propagator in the deep infrared.

The scenario of quark confinement uses the presence of a linear rising potential between an (infinitely) heavy quark-antiquark pair as a criterion. In this picture, the quarks are connected by so-called color flux tubes, as indicated in the sketch of Fig. 2.B. With an increasing distance R between quark and antiquark, the potential energy between the two particles increases with a slope that defines the string tension. In a strict form of this criterion, a theory is only confining if the potential between the quark-antiquark pair is infinitely rising with increasing R . In QCD however, at some point the potential energy between quark and antiquark will be large enough to create another $q\bar{q}$ -pair: the string, or flux tube breaks (see lower panel of Fig. 2.B), which renders QCD, in a strict sense, not confining.

For this work however, we will consider the presence of a linear rising potential as a sufficient criterion for confinement and investigate the associated string tension.

Wilson loop and string tension

The Wilson loop was originally defined as the spacetime area that is enclosed by the world-line around the creation of a static quark-antiquark pair at some initial time t_i and their annihilation at a final time t_f . In the Heisenberg picture, this reads

$$W(t_i, t_f, \Delta r) = \langle 0 | \bar{\psi}(t_i, r_1) \psi(t_f, r_2) | 0 \rangle. \quad (2.39)$$

Switching to the Schrödinger picture and imaginary time formalism, we shift the time dependence to the states. Thus, the Wilson loop is given by

$$W(t_i, t_f, \Delta r) = \langle 0 | \exp(H \tau_i) \bar{\psi}(r_1) \exp(-H \tau_i) \exp(H \tau_f) \psi(r_2) \exp(-H \tau_f) | 0 \rangle. \quad (2.40)$$

Inserting two trivial unit matrices in the *eigenbasis* of the Hamiltonian, we use the cooling mechanism to recover the lowest energy contribution by sending $\beta \rightarrow \infty$,

$$W(t_i, t_f, \Delta r) \sim \exp((E_1 - E_0)(\tau_i - \tau_f)) \quad (2.41)$$

$$W(\Delta t, \Delta r) \sim \exp(-V(\Delta r)\Delta\tau), \quad (2.42)$$

where the potential $V(\Delta r)$ measures the excitation energy between the ground (vacuum) state and the vacuum state plus two static charges separated by a distance Δr . In a confining theory,

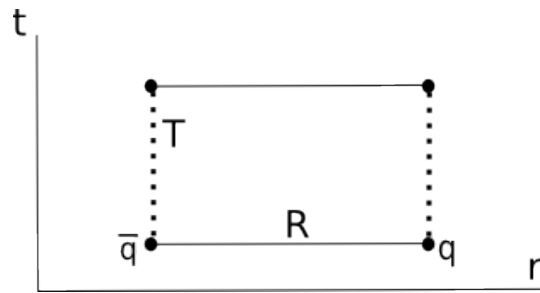


Figure 2.C: Sketch of a Wilson loop winding around spacetime.

this potential is for large separation distances R given by

$$V(R) \sim \sigma R, \quad (2.43)$$

with the proportionality constant σ , that describes the so-called string tension. If confinement is present, thus the Wilson loop behaves like

$$W(T, R) = \exp(-\sigma TR), \quad (2.44)$$

with a spacetime area in the argument of the exponential. Therefore the area-law fall-off of the Wilson loop is an indicator of confinement.

In the following, the so-called spatial Wilson loop will be important. It is defined in an analogous way to Eq. (2.44), except that the charges are created at a fixed position in one spatial direction, propagate in another spatial direction before they are annihilated. The so-called spatial string tension is equal to the spacetime string tension from Eq. (2.43) due to Lorentz invariance.

2.5. Dyson–Schwinger Equations

Dyson–Schwinger equations (DSEs) are the quantum equations of motion. They come as an infinite tower of coupled integral equations, interrelating a theory’s n -point functions with each other. The DSEs are derived from the identity

$$\int [d\varphi]_{ren} \frac{\delta}{\delta\varphi} e^{-S[\varphi] + \int d^n x' J(x')\varphi(x')} = 0, \quad (2.45)$$

with the action S , the source J and the dummy field variable φ , expressing the translational invariance of the quantum effective action in the field φ . The identity Eq. (2.45) can be transformed into

$$\frac{\delta\Gamma}{\delta\phi(x)} = \frac{\delta S}{\delta\varphi(x)} \left[\varphi = \int G \frac{\delta}{\delta\phi} + \phi \right], \quad (2.46)$$

with the help of general functional relations between the source field and the quantum effective action. In the master equation, Eq. (2.46), Γ denotes the quantum effective action as defined in Eq. (2.4) of the theory in consideration. Already at this point, it is visible that the one-point function on the left hand side of Eq. (2.46) depends on higher n -point functions on

$$\text{---} \circ \text{---}^{-1} = \text{---}^{-1} + \text{---} \circ \text{---}^{-1}$$

Figure 2.D: The pictorial representation of the Dyson–Schwinger equation for a fermion propagator. The curly lines represent gauge boson propagators, straight ones fermion propagators. We indicate dressed propagators by adding filled circles to the basic lines. The dressed fermion–boson vertex is encoded by the empty circle.

the right hand side. Further functional derivatives with respect to the fields and subsequently setting the sources to zero yield $n + 1$ -point, $n + 2$ -point functions, *etc.*.

The resulting infinite set of coupled equations still contains all information of the original degrees of freedom of the theory as it is, without any expansion schemes involved. A diagrammatic representation of the fermion DSE is exemplarily displayed in Fig. 2.D. The vertex, as well as the gauge boson, obey their own DSEs that are of a similar structure as the fermion DSE.

Solving the complete system of equations therefore is equivalent to solving the theory itself. For Landau gauge Yang–Mills theory, such an analytical solution for the deep infrared was obtained in [35, 36]. Numerically, one has to truncate the equations to make them accessible. The choice of the truncation scheme decides on the quality of the results and is therefore of paramount importance. In any case, the scheme has to obey general constraints such as the conservation of global and local symmetries, multiplicative renormalizability or the reproduction of perturbative results in the weak coupling limit.

It is common practice to truncate the equations by considering a more or less sophisticated ansatz for the fermion–boson vertex function, since the vertex DSE involves the computation of a four point function of which only very little is known to date⁴. The vertex *ansatz* is designed such that it compensates for as many features of the omitted functions as possible. In practice, this construction procedure is a formidable task as can be seen from the numerous different types of vertex *ansätze* available [37–45].

For a complete derivation of the DSEs, we refer the interested reader to the works [1, 2]. In the following parts, we will state the DSEs for the dressed propagators and then project onto the dressing functions.

⁴for more information, see *e.g.*[37]

3. QED₃ in an anisotropic spacetime

Quantum electrodynamics in two spatial- and one temporal dimension, QED₃, is the most simple elementary gauge theory that displays nontrivial nonperturbative dynamics. It furthermore offers a rather agreeable environment for nonperturbative studies that is characterized by several key features: firstly, due to its Abelian nature, it is free of gauge boson self-interactions. Furthermore, the dimensionality guarantees its super renormalizability, *i.e.* only a finite number of Feynman diagrams is divergent. Nevertheless the number of dimensions still allows for a dynamical mass generation, that would be forbidden [46] in a lower dimensional theory (→ the Schwinger model, see [47, 48]).

Over the decades, the investigation of QED₃ received a lot of attention. Besides its function as a potential toy model for QCD, the application of QED₃ as a low-energy effective theory for strongly correlated condensed matter systems catalyzed the interest in the theory for its own sake.

In this first part of the work at hand, we report on the investigations of anisotropic QED₃ from a finite-volume Dyson–Schwinger perspective. We focus on an incarnation of QED₃ that could serve as a low-energy effective theory for high temperature superconductors (HTSs). Our analysis concentrates on the phase transition between the chirally broken and symmetric phase.

This chapter is organized as follows: section 3.1 reports on investigations of the phase diagram for the critical number of fermion flavors for chiral symmetry breaking in dependence on the anisotropies at vanishing temperature. The central questions are

- How large is the critical number of fermion flavors for chiral symmetry breaking?
- How is this number influenced by anisotropies of arbitrary size?
- Which consequences does that have for the physical number of fermion flavors $N_f = 2$?

Section 3.2 resumes the analysis of chiral symmetry breaking in anisotropic spacetime at finite temperatures. Apart from approaching more realistic conditions for HTS materials, the finite temperature scenario offers the possibility to study the generic scaling behavior of the thermal phase transition line close to the quantum critical point. We consider the following questions to be at the heart of our investigations:

- What is the effect of finite temperatures on the critical number of fermion flavors at finite anisotropies?
- How does the thermal phase transition line merge with the quantum critical point?

- Is the scaling behavior influenced by finite anisotropies?

The results of these chapters have been published in [49] and [50].

3.1. QED₃ at zero temperature

3.1.1. QED₃ as an effective theory for high-temperature superconductors

The application of QED₃ as a low energy effective theory for condensed matter systems received a respectable amount of interest over the last decades. The reinterpretation of the fermions and gauge bosons as the low energy quasi-particles relevant for phase transitions between the strongly coupled phases of *e.g.* superconducting materials opened up a completely new perspective on phenomena that are technically applied for years. Since there is no such thing as confinement of the quasiparticles, the broad range of experimental input permanently offers new interesting scenarios with an immediate relevance to applied physics.

The attention for QED₃ was not least triggered by the Nobel Prize of Novoselov and Geim for their works on graphene in 2010, *e.g.* [51]. To summarize briefly, graphenes are made up of two carbon sub-lattices. Close to the crossing points of the energy bands of the sub-lattices, electrons and holes behave like massless relativistic quasiparticles with a linear dispersion relation. As electrons and holes are not independent particles, they do not obey separate Schrödinger-equations but are combined into a two component spinor wave function obeying the massless Dirac-equation. These characteristics motivate the description of graphenes with the help of Quantum Electrodynamics [52].

Another very prominent application of QED₃ to condensed matter physics are high-temperature superconductors. Their description in terms of a QED₃-like theory was motivated from several experimental (ARPES) findings, amongst others again the linear dispersion relation of the quasiparticles relevant for HTSs. The works of [53–59] provided the necessary derivations for a form of QED₃ that allows to capture the features of the so-called pseudo gap phase of HTSs.

Though both condensed matter systems were shown to be describable by QED₃-theories, there are important differences in these descriptions. For instance, both effective theories have different fermion-boson couplings and neither are the velocities of the quasiparticles close to the nodes of the energy-gap function equal. Furthermore, in HTSs, gauge bosons are confined to the (2+1) dimensional setting from the very start, while the description of graphene includes 'real', four dimensional photons. In that sense, the critical behavior is non-universal. In this work, we concentrate on the application of QED₃ as an effective low-energy theory for HTSs. We now summarize their key features as well as the most important aspects of the deduction of the QED₃ Lagrangian that is at the center of all subsequently presented investigations.

Superconductors are generally divided into two subclasses: conventional (type I) and unconventional (type II) ones. While conventional superconductors are known since 1911, unconventional ones were discovered rather recently, in 1986 [60]. However, while the type I and also the low-temperature type II superconductors can be described very precisely by Bardeen–Cooper–Schrieffer (BCS) theory [61, 62], no such matching description is known for a subgroup of type II materials, the high-temperature superconductors.

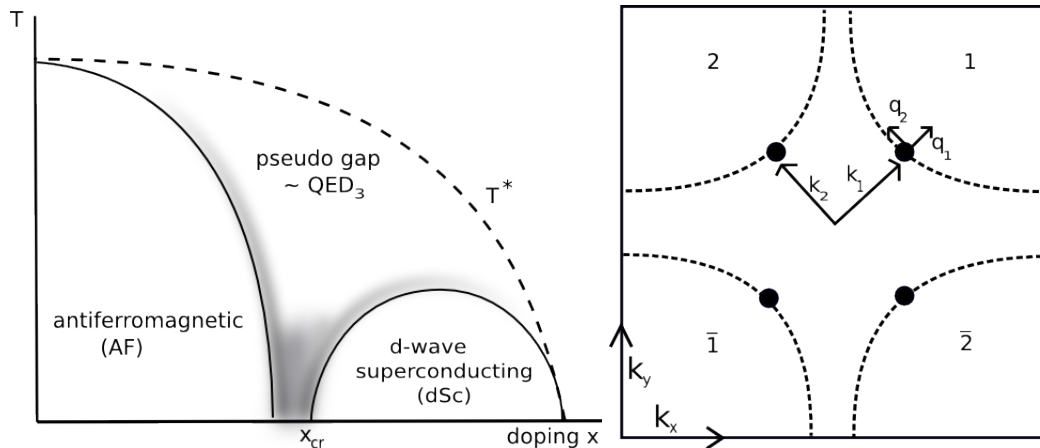


Figure 3.A: Left panel: The phase diagram of cuprate superconductors, dependent on the doping x and temperature T . Indicated are the anti-ferromagnetic phase (AF), the pseudo-gap phase (described by QED₃) and the superconducting phase with d-wave-symmetric order parameter (dSc). The shaded area indicates that the course of the phase transition lines are not clear. The temperature T^* is the Néel temperature. Right panel: The sketch of the Fermi surface of HTS materials. Indicated by dots are the pairwise related nodes of the energy gap function that happen to lie on the Fermi surface. We further suggest the rotation into a coordinate system located at the node(s). It is in the vicinity of the nodes where the QED₃ derivation holds.

There are several reasons for this. One is that in conventional superconductors, the 'normal' phase displays a metallic behavior, which can be modeled in a reliable way. Furthermore, the order parameter of the transition to the superconducting phase, the energy gap function has s-wave symmetry and therefore no zeroes. The energy gap function describes the energy gap between the valence and the conduction band. The non-vanishing gap implies that there are no fermionic excited states. In contrast, an attractive phonon-mediated pairing interaction between electrons leads to the formation of bosonic Cooper pairs. They obey Bose–Einstein statistics and occupy an energetically favorable state protected by the energy gap. Since the bosonic quasiparticles can occupy the same state at the same time, it is additionally possible to describe them by an overall wave function that extends over the entire crystal.

HTS materials however form a subgroup of the unconventional superconductors. They are distinguished by their high critical temperature $T_c > 77$ K and made up by ceramic compounds, the cuprates. Their outstanding feature are copper-oxide planes in the crystalline lattice. These planes are embedded in insulating layers and provide the necessary conditions for superconduction if a critical doping is guaranteed¹. Furthermore, unconventional superconductors display the Meissner–Ochsenfeld effect for magnetic field strengths in the region $H_{cr1} \ll H \ll H_{cr2}$. For magnetic field strengths below H_{cr1} the field is completely expelled from the superconductor, as for conventional superconductors. For larger fields, up

¹Doping means that an atom of one sort is replaced by one of another sort. This replacement has to be done in a certain ratio in order to provide the environment for superconduction.

to a second critical value, H_{c2} , the magnetic field penetrates the material, but is confined to so-called flux tubes (or vortices) [58]. These create topological defects that become relevant in turn of the derivation of the QED₃ Lagrangian. Above the second critical field strengths, superconductivity beaks down.

Coming back to the missing overall theory to describe the HTS materials, a first important difference to conventional superconductors is the anti-ferromagnetic (AF) non-superconducting phase (see the phase diagram in Fig. 3.A). The Mott-insulator itself is a strongly correlated system [63] and hard to describe in terms of microscopic degrees of freedom. Further, the energy gap function, that governs the phase transition from superconducting to insulating phase was shown experimentally to have $d_{x^2-y^2}$ -wave symmetry [64]. The different symmetry gives rise to profound changes. On the one hand, the quasiparticles' spectral properties [54] are changed. On the other hand, the d-wave symmetry energy gap has zeroes that were shown to lie on the quasiparticles Fermi surface (see right panel of Fig. 3.A). This leads to quasiparticles, *i.e.* fermionic excitations, of arbitrary low energies that can exist near the nodes of the energy gap function. These quasiparticles were found to have a linear dispersion relation, thus behaving like massless Dirac particles. Furthermore, the speeds of the quasiparticles were measured to be different in direction parallel and orthogonal to the Fermi surface. The ratio of these two speeds turned out to be in the order of 10, thus not at all negligibly small. Thus, in comparison to pure BCS superconductors, fermionic excitations exceedingly complicate the interactions and dynamics of HTSs.

It turned out that a description of unconventional superconductors is best approached in an inverted way, as applied [65]. 'Inverted' refers to starting with the description of the superconducting phase and the investigation of the mechanisms that drive the system to the anti-ferromagnetic phase (in contrast to the approach of conventional superconductors). The reason for this is the antiferromagnetic phase, a Mott insulator, that represents itself a strongly coupled system. This approach lead to the finding of another phase, in between the superconducting and the antiferromagnetic phase, the so called pseudo gap. This phase is limited by the Néel temperature T^* (see again Fig. 3.A, left panel), above which any magnetic ordering is destroyed and the materials become paramagnetic. The distinguishing features of the pseudo-gap phase is a non-zero energy gap amplitude, as in the superconducting phase while at the same time the phase coherence of the gap function is lost (as in the AF phase) [20]. The destruction of phase coherence results from vortex fluctuations.

The shaded borders of the pseudo-gap phase in the phase diagram of Fig. 3.A indicate that it is not clear how it behaves exactly. In particular, it is not certain if there is a pseudo-gap phase at vanishing temperature for critical doping, or if the antiferromagnetic and the superconducting phases meet. With a QED₃ description of the pseudo-gap phase, we will study the course of the phase borders. In the frame of the QED₃ description of the pseudo-gap phase, the transition to the antiferromagnetic phase is identified with the breakdown of chiral symmetry. Therefore, we analyze the chiral phase transition at vanishing and finite temperatures under the influence of an anisotropic spacetime.

3.1.2. QED₃ Lagrangian for HTSs

In this chapter, we wish to state the Lagrangian for anisotropic QED₃ as it was derived by [20, 56, 66]. A more detailed summary on the derivation procedure from a BCS-like Hamiltonian to the actual Lagrangian QED₃ formulation can be found in App. A.1.

In the following, we apply the notation as it was introduced by [56]. We chose the four dimensional spinor representation of the (2+1) dimensional fermions, as discussed in chapter 2.1. These obey the Clifford algebra $\{\gamma_\mu, \gamma_\nu\} = 2\delta_{\mu\nu}$. We allow for general N_f fermion flavors, since we wish to study the influence of the anisotropic velocities on the criticality of N_f . Furthermore, we introduce the anisotropic fermionic velocities v_f and v_Δ as they arise during the derivation procedure. They describe the quasiparticles' speed orthogonal and perpendicular to the Fermi surface of the HTS materials and are distinct from the characteristic speed for the vortex-antivortex excitations, c_s . This includes the fact, that both v_f and v_Δ may be larger than c_s , as discussed in Ref. [59].

The anisotropic velocities enter the theory via the metric-like structure $g_{i,\mu\nu}$. The 'metric' has an additional index i that denotes the node under description. The nodes in HTS materials are zeroes of the quasiparticles energy-gap function that were shown to lie on the Fermi surface of the electrons and holes [64]. Due to symmetry reasons, only two out of four zeroes need to be considered separately [63] (see also right panel of Fig. 3.A). For convenience, we chose the anisotropic velocities relative to c_s which we normalize to 1. Thus, the metric is given in form of

$$\left(g_1^{\mu\nu}\right) = \begin{pmatrix} 1 & 0 & 0 \\ 0 & v_f^2 & 0 \\ 0 & 0 & v_\Delta^2 \end{pmatrix} \quad \left(g_2^{\mu\nu}\right) = \begin{pmatrix} 1 & 0 & 0 \\ 0 & v_\Delta^2 & 0 \\ 0 & 0 & v_f^2 \end{pmatrix}. \quad (3.1)$$

With the necessary building blocks, the fermionic part of the Lagrangian is given by

$$\mathcal{L}^{aniso} = \frac{N_f}{2} \sum_{j=1,2} \bar{\Psi}_j \left\{ \sum_{\mu=0}^2 \gamma_\nu \sqrt{g_{j,\nu\mu}} (\partial_\mu + i a_\mu) \right\} \Psi_j. \quad (3.2)$$

In contrast to the more familiar isotropic QED₃ Lagrangian, we now have the additional metric-like factors and the sum over the nodal index j included.

We can now proceed to derive the Dyson–Schwinger equations in momentum space from the quantum effective action as described in chapter 2.5.

3.1.3. Dyson–Schwinger equations for anisotropic spacetime

The spacetime anisotropies introduced via the metric-like tensor $g_{\mu\nu}$ do not influence the functional form of the DSEs. Diagrammatically, they are represented in the standard way as displayed in Fig. 3.B. Nevertheless, the influence of the anisotropies becomes obvious when considering the propagator DSEs, here given in Euclidean spacetime.

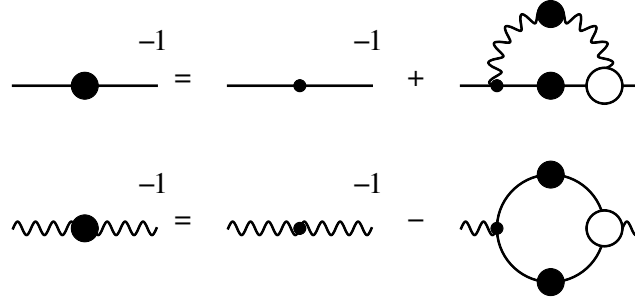


Figure 3.B: The Dyson–Schwinger equations in their diagrammatic form. The upper panel displays the fermion, the lower panel the gauge boson DSE. The straight lines with indicate fermion-, the wiggly lines gauge boson propagators. The dressed propagators are furthermore distinguished by filled blobs, while the bare propagators have dots. The open circle represents a dressed fermion-boson vertex.

$$S_{F,i}^{-1}(\vec{p}) = S_0^{-1}(\vec{p}) + Z_1 e^2 \int \frac{d^3 q}{(2\pi)^3} (\sqrt{g_{i,\mu\alpha}} \gamma^\alpha S_{F,i}(\vec{q}) \sqrt{g_{i,\nu\beta}} \Gamma^\beta(\vec{q}, \vec{p}) D_{\mu\nu}(\vec{k})), \quad (3.3)$$

$$D_{\mu\nu}^{-1}(\vec{p}) = D_{0,\mu\nu}^{-1}(\vec{p}) - Z_1 e^2 \frac{N_f}{2} \sum_{i=1,2} \int \frac{d^3 q}{(2\pi)^3} \text{Tr} \left[\sqrt{g_{i,\mu\alpha}} \gamma^\alpha S_{F,i}(\vec{q}) \sqrt{g_{i,\nu\beta}} \Gamma^\beta(\vec{p}, \vec{q}) S_{F,i}(\vec{k}) \right]. \quad (3.4)$$

The gauge boson hereby depends on the difference of the momenta of the fermions, thus $\vec{p} - \vec{q} = \vec{k}$. The nodal index is denoted by i and sums again over the two nodes of the energy-gap function on the Fermi surface. Furthermore, the equations include the fermion-boson vertex renormalization constant Z_1 . The vertex itself is denoted by $\Gamma^\beta(\vec{p}, \vec{q})$.

The number of ‘metric’ insertions in Eq. (3.3) and Eq. (3.4) already hint at the more complex structure of the DSEs for the dressing functions. In order to simplify keeping track of the equations, we define two shorthands.

Firstly, we introduce

$$\bar{p}_i^2 := p_\mu g_i^{\mu\nu} p_\nu \quad (3.5)$$

whenever two quantities are contracted in a similar way. Recall that the nodes of the (energy) gap function on the Fermi surface of the electrons each demanded its own metric tensor. The bar-momentum squared thus represents a typical quantity that naturally arises out of the structure of the equations. Notice also that the bar-momentum squared reduces to the ordinary squared momentum if the isotropic limit is carried out.

Secondly, we define

$$\bar{p}_{\mu,i} := A_{\mu,i}(\vec{p}) p_\mu, \quad (\text{no summation convention!}), \quad (3.6)$$

where $A_{\mu,i}$ denotes the vectorial fermionic dressing function at node i . It affects only the combination of the fermion vector dressing function $A_\mu(\vec{p})$ and an arbitrary momentum p_μ above. In the isotropic limit, Eq. (3.6) will reduce to $A(p^2)\vec{p}$, as there is only one vectorial dressing function for all momentum components in the isotropic case.

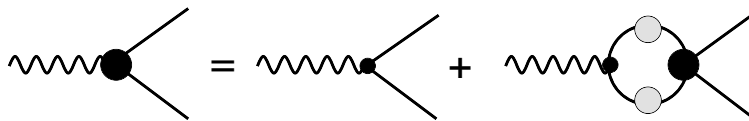


Figure 3.C: The diagrammatic representation of the vertex DSE. Wiggly lines denote gauge boson propagators, straight lines fermion propagators. The dressed vertices are indicated by black dots, dressed propagators by gray dots.

With these abbreviations, we write down the general form for dressed fermion propagator in the anisotropic spacetime,

$$S_{F,i}^{-1}(\vec{p}) = B_i(\vec{p}) + i \sqrt{g_i^{\mu\nu}} \gamma_\nu \tilde{p}_{\mu,i}, \quad (3.7)$$

The scalar fermion dressing function at node i is denoted as B_i . In contrast to isotropic spacetime, the function depends on every momentum component, not only on the squared vector. The full gauge boson propagator is decomposed into the bare contribution and the self-energy $\Pi_{\mu\nu}(\vec{p})$,

$$D_{\mu\nu}(\vec{p})^{-1} = p^2 \left(\delta_{\mu\nu} - (1 - \xi) \frac{p_\mu p_\nu}{p^2} \right) + \Pi_{\mu\nu}(\vec{p}). \quad (3.8)$$

Notice, that the bare part of the gauge boson propagator is still the isotropic bare propagator. Since we work in Landau gauge in the following, the gauge parameter is given by $\xi = 0$.

Vertex Specification

As a next step, we need to define the input for the fermion-boson vertex Γ^β . The vertex in principle has its own DSE that has to be solved. However, the endeavor of solving the vertex DSE is rather involved. The reason for this is can be found in the structure of the DSEs: the equation for the n -point function involves m -point functions, with $m > n$. In the case of the vertex DSE, the fermion four-point function appears on the right hand side of the equation (see Fig. 3.C). To date, only very little information is available on this function.

An alternative is the application of a vertex *ansatz*. Though there are a rather large number of vertex *ansätze* available [41, 67, 68], studies in isotropic spacetime [11] have shown that the critical number of fermion flavors for chiral symmetry breaking is only slightly sensitive to the more elaborate structures of the vertex. In fact, the deviation of the critical number for a bare vertex (*i.e.* $\Gamma_\mu \sim \gamma_\mu$) and very sophisticated vertex constructions remained smaller than five percent. For the investigations presented in this work, we already increased the complexity of the DSEs enormously when considering a maximally anisotropic spacetime. To keep the computational effort in reasonable limits, we uphold the findings in isotropic spacetime to apply the simplest available vertex construction that is consistent with our approximations in the gauge boson sector. In particular, we use the leading term of the Ball-Chiu (MinBC or 1BC) vertex construction [69] transferred to an anisotropic spacetime as an *ansatz* for the

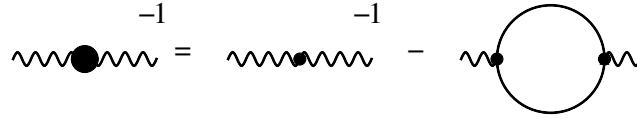


Figure 3.D: Diagrammatic form of the leading order large- N_f vacuum polarization of the gauge bosons. Wiggly lines represent gauge boson propagators, straight lines fermions. Small dots indicate bare quantities, filled blobs dressed ones.

fermion-boson vertex,

$$\Gamma_i^\beta(\vec{p}, \vec{q}) = \gamma^\beta \frac{A_i^\beta(\vec{p}) + A_i^\beta(\vec{q})}{2}, \quad (3.9)$$

where we did not apply the summation convention. The momenta p, q denote the in- and outgoing fermionic momenta at the vertex. As was shown by [70], the MinBC vertex represents a reasonable approximation to the full Ball-Chiu vertex that is constructed to satisfy the Ward identity exactly. Besides the MinBC vertex, we will employ the bare vertex in the context of the large- N_f or the Pisarski approximation [71]

Gauge boson specification - scheme 1

In this work, we investigate two different approximation schemes for the dressed gauge boson. In particular, we firstly analyze the large- N_f approximation. From this analysis we hope to obtain a first rough idea of the influence of anisotropy onto the transition from the chirally symmetric to the chirally broken phase. As a next step, we proceed to a more elaborate model, that includes the anomalous dimension of the fermion vector dressing function. In this sense, our model builds on the results obtained in [11].

The large- N_f approximation for isotropic QED₃ was investigated in great detail in [72, 73]. The results of these investigations qualitatively still hold in comparison with less approximated studies [11].

Considering anisotropic spacetime, investigations of small anisotropic velocities in leading order large- N_f were performed by [20, 56]. One objective of this work is to overcome these limitations, especially the restriction to small anisotropies. We consider the maximal influence of anisotropies, that is to say all three velocities (c_s, v_f, v_Δ), whereas we normalize the velocities such that $c_s = 1$. The analytically integrated vacuum polarization reads [20, 56]

$$\begin{aligned} \Pi^{\mu\nu}(\vec{p}) &= \sum_i \sqrt{\bar{p}_i^2} \left(g_i^{\mu\nu} - \frac{g_i^{\mu\alpha} p_\alpha g_i^{\nu\delta} p_\delta}{\bar{p}_i^2} \right) \Pi_i(\vec{p}), \\ \Pi_i(\vec{p}) &= \frac{e^2 N_f}{16 v_F v_\Delta} \frac{1}{\sqrt{\bar{p}_i^2}}. \end{aligned} \quad (3.10)$$

The diagrammatic representation of the large- N_f vacuum polarization is displayed in Fig. 3.D.

Gauge boson specification - scheme 2

The large- N_f approximation is a very rewarding approximation scheme to obtain a first idea of the effects of new parameters, considering the balance between complexity of the equations and obtained results. Nevertheless, the large- N_f scheme is clearly an approximation that needs improvement.

A main reason for this is the fact that the fermionic vector dressing functions are $A_i = 1$ for the complete range of momenta. This is a severe limitation, since isotropic investigations have shown the fermion vector dressing function and the boson vacuum polarization both develop power laws in the infrared region in the chirally symmetric phase [11].

Additionally, the values of the A -functions at zero momenta in anisotropic spacetime enter the definition of renormalized anisotropic velocities (c_s^R, v_f^R, v_Δ^R). It is questionable, if there exists a nontrivial definition of the renormalized velocities in the large- N_f scheme.

In order to account for these shortcomings, our first steps beyond large- N_f are built on the findings of [11]. In [11], the authors derived, amongst others, power-law solutions for the gauge boson vacuum polarization $\Pi(k^2)$ and the fermion vector dressing function $A(p^2)$ in Landau gauge from a self-consistent infrared analysis of the DSEs in the chirally symmetric phase. For the vertex, the minimal Ball-Chiu *ansatz* (see Eq. (3.9)) was chosen. In particular, they found the power-law solutions given by

$$A(p^2) \sim p^{2\kappa}, \quad (3.11)$$

$$\Pi_{1BC}(k^2) \sim k^{-1-2\kappa}, \quad (3.12)$$

with the fermionic momentum p , the bosonic momentum k and the anomalous dimension of the fermionic vector dressing function, κ . The infrared exponent is sensitive to the employed vertex *ansatz*. From a numerical study of the fermion wave function and the gauge boson DSE, including the 1BC-vertex (Eq. (3.9)), the anomalous dimension for κ was determined as

$$\kappa_{1BC} = \frac{0.115}{N_f} + \frac{0.044}{N_f^2} + \mathcal{O}(1/N_f^3). \quad (3.13)$$

Based on these findings, we can formulate the isotropic approximation of the vacuum polarization in the chirally symmetric phase, including the infrared exponent κ ,

$$\Pi(k) = \frac{e^2 N_f}{8} \left(\frac{1}{k} \frac{k^2}{k^2 + e^2} + \frac{1}{k^{1+2\kappa}} \frac{e^2}{k^2 + e^2} \right). \quad (3.14)$$

For the vertex *ansatz* (3.9) and the model for the vacuum polarization, Eq. (3.14), the anomalous dimension was determined from $N_f^{c,model}$ as $\kappa = 0.0358$ in isotropic spacetime (see discussion in chapter 3.1.4). We employ this value of κ for our calculations although the anomalous dimension may, in principle, be a function of the anisotropic velocities $\kappa(v_f, v_\Delta)$ as well. However, at this point we cannot calculate this dependence and therefore assume κ to be constant in the following investigations. Notice that for $\kappa = 0$, this approximation reduces to the large- N_f limit.

Generalized to an anisotropic spacetime with a constant anomalous dimension, the isotropic

model for the vacuum polarization (3.14) transforms into

$$\Pi_i(\vec{p}) = \frac{e^2 N_f}{16 v_F v_\Delta} \left(\frac{1}{\sqrt{\bar{p}_i^2}} \frac{\bar{p}_i^2}{\bar{p}_i^2 + e^2} + \frac{1}{\bar{p}_i^{1+2\kappa}} \frac{e^2}{\bar{p}_i^2 + e^2} \right). \quad (3.15)$$

Here, we used the shorthand \bar{p}_i^2 that we introduced in Eq. (3.5).

We conclude the introduction of our approximation schemes with some words on the combination of the vertex and gauge boson schemes.

Therefore, we wish to point out in the first place that when truncating the equations, it is important to define a set of consistent approximation and truncation schemes for the vertex and the gauge boson. An inconsistent combination of approximations would be to employ the vertex *ansatz* (3.9) in the fermionic DSEs and at the same time work in the large- N_f approximation for the gauge boson. As a consequence, the critical number of fermion flavors would go to infinity, $N_f^c \rightarrow \infty$, and the fermions remain massive in all cases. This finding is in contrast to the findings in the pure $1/N_f$ approximation in both DSEs, where $N_f^c \approx 3.24$ [72] and to the improved MinBC/boson model results, where $N_f^c \approx 3.56$ [11]. Therefore, we will concentrate our investigations of anisotropic spacetime on two approximation schemes: the large- N_f /bare vertex and the MinBC/boson model approximation scheme. The results are presented in chapter 3.1.4.

DSEs for dressing functions

With the truncation of the vertex and the approximations in the gauge boson sector introduced, we return to the DSEs for the fermionic dressing functions. We obtain these DSEs from Eq. (3.3) by projecting onto the scalar, respectively the components of the vector dressing function and tracing.

The resulting equations are given by

$$B_i(\vec{p}) = Z_2^2 e^2 \int \frac{d^3 q}{(2\pi)^3} \frac{B_i(\vec{q}) g_i^{\mu\nu} D_{\mu\nu}(\vec{k})}{B_i(\vec{q})^2 + (\vec{q}_i)^2}, \quad (3.16)$$

$$A_{\mu,i}(\vec{p}) = Z_2 - \frac{Z_2^2 e^2}{p_\mu} \int \frac{d^3 q}{(2\pi)^3} \left\{ \frac{2(\vec{q}_{\lambda,i} g_i^{\lambda\nu} D_{\mu\nu}(\vec{k})) - \vec{q}_{\mu,i} g_i^{\lambda\nu} D_{\lambda\nu}(\vec{k})}{B_i(\vec{q})^2 + (\vec{q}_i)^2} \right\} \frac{A_{\mu,i}(\vec{p}) + A_{\mu,i}(\vec{q})}{2}. \quad (3.17)$$

Remember that there is no summation over the index μ in the vectorial fermion dressing function. In fact, Eq. (3.17) encodes three DSEs for the dressing functions of each momentum component. Together with the nodal index i , this would result in eight DSEs for the fermionic dressing functions alone. However, a closer look at the symmetries of the metric-like tensor $g_{\mu\nu}$ shows that this number can be reduced by interchanging the arguments of the fermionic functions,

$$B_1(p_0, p_1, p_2) = B_2(p_0, p_2, p_1), \quad (3.18)$$

$$A_{\mu,1}(p_0, p_1, p_2) = A_{\mu,2}(p_0, p_2, p_1). \quad (3.19)$$

This reduces the number of equations to solve to four. Similar symmetries can also be identified for the vacuum polarization, which reduces the number of components to compute from six to four,

$$\Pi^{11}(p_0, p_1, p_2) = \Pi^{22}(p_0, p_2, p_1), \quad (3.20)$$

$$\Pi^{10}(p_0, p_1, p_2) = \Pi^{20}(p_0, p_2, p_1). \quad (3.21)$$

Notice that if we wanted to solve the full boson DSE, we needed to find the self-consistent solution for the DSEs of four components of the anisotropic gauge boson vacuum polarization. In contrast, there are only four DSEs to solve in total (fermionic and bosonic) in an isotropic spacetime.

For our investigations of Eq. (3.16) and Eq. (3.17), we will furthermore set the fermion wave function renormalization constant $Z_2 = 1$ which is convenient in continuum calculations². This corresponds to a renormalization point that is far enough in the UV, such that the dressing functions are insensitive to the exact choice.

Finite volume DSEs

As the previous section explained, the introduction of finite anisotropies leads to a considerable increase in complexity and computational demand of the DSEs. Any possible simplification on the numerical side is therefore highly welcome.

One possibility to preserve computational resources is by choosing a problem-suited underlying manifold and coordinates. In our case, this corresponds to a three dimensional compactified Euclidean manifold, a three torus. Solving Dyson–Schwinger equations on a three torus was studied in great detail in *e.g.* [74, 75], where the interested reader can find an extended discussion of the transition from infinite to finite volume. In the following, we only state the most important points of the finite volume formalism.

The compactification is performed by confining the quarks into a ‘box’ of finite size and imposing (anti)periodic boundary conditions onto the (fermionic) bosonic wave functions. The box length in direction μ is denoted by L_μ , the volume by $V = L_0 \cdot L_1 \cdot L_2$. In principle, only the time direction of the particles has restrictions on periodicity due to the Kubo–Martin–Schwinger (KMS) relation (see *e.g.* [15]). We are free to choose the boundary conditions for the spatial directions³. However, for convenience, we impose the same boundary conditions in temporal and spatial directions. In consequence, the fermionic momenta are discretized and denoted by

$$k_\mu = \frac{2\pi}{L} n_\mu \quad \text{for bosons,} \quad (3.22)$$

$$k_\mu = \frac{2\pi}{L} \left(n_\mu + \frac{1}{2} \right) \quad \text{for fermions,} \quad (3.23)$$

with the integer numbers $n_\mu \in \mathbb{Z}$. The discretized momentum spacetime leads to a summation over Matsubara modes instead of previous continuous integration.

$$\int \frac{d^3 q}{(2\pi)^3} (\dots) \rightarrow \frac{1}{L^3} \sum_{n_1, n_2, n_3} (\dots). \quad (3.24)$$

²A study of the renormalization point dependence can be found in App. A.2

³Earlier investigations of periodic spatial boundary conditions have shown that the results change only marginally.

In isotropic spacetime, the O(3) symmetry would now allow the transformation⁴ of Cartesian to hyperspherical coordinates that saves a respectable amount of computational resources. For anisotropic spacetime however, this is no longer possible since the sphere would be deformed into a triaxial ellipsoid. At maximum, we can find a cylindrical symmetry in the case of finite temperatures and equal anisotropic velocities $v_f = v_\Delta$, that will be discussed in chapter 3.2. Therefore the Cartesian summation, as it emerges automatically in the torus formulation, is the most 'natural' way to attack the anisotropic DSEs. The solution process itself is the same as for isotropic spacetime. A detailed discussion thereof can be found in Ref. [75].

However, speaking of the advantages of the torus formulation in anisotropic spacetime, we need to mention its drawbacks for completeness. Similar to lattice gauge theory calculations, we have to deal with finite volume, and potentially finite size effects. In isotropic spacetime, finite volume effects were investigated in great detail in [75]. Unfortunately, a comparable study in anisotropic spacetime is out of reach, due to the enormous increase in computational demand. We will come back to this point when discussing the numerical results in sections 3.1.4 and 3.2.3. However, our volumes are large compared to lattice settings. This is the reason why we are not restricted to certain ranges of anisotropy as the lattice calculations [66, 78, 79]. Finite size effects on the other hand are expected to be small in our calculations.

⁴applied in *e.g.* [75–77]

3.1.4. Numerical Results: The phase diagram of HTS at zero temperatures

We now proceed to the discussion of our numerical results. To this end, we solved the Dyson–Schwinger equations in a finite volume as described in the previous section. We employed three different approximation schemes including more and more sophisticated *ansätze*.

To set our results into context with earlier studies, we firstly summarize some main findings in isotropic spacetime. Subsequently, we start the discussion of our results for an anisotropic spacetime with the Pisarski approximation scheme, originally introduced in [71]. Secondly, we present a first phase diagram for leading order large- N_f expansion (and bare vertices). Finally, we present the phase diagram for the boson model/MinBC approximation scheme, specified in Eq. (3.9) and Eq. (3.15).

To complete this numerical results chapter, we add the discussion of finite volume effects and possible locations of physically realized HTS materials.

The critical N_f^c in the isotropic case

Pisarski’s approximation scheme [71] includes a bare vertex as an *ansatz* for the fermion-boson vertex and a scalar fermion dressing function for all momenta, $B(\vec{p}) = B(0) = m$. Due to these approximations, it is possible to solve the Dyson–Schwinger equation for the scalar fermion dressing function analytically,

$$m = B(0) = c \alpha e^{-\pi^2 N_f / 8}. \quad (3.25)$$

Hereby c is a positive constant and the coupling constant is given by $\alpha = e^2 N_f$. As can be seen from this expression, chiral symmetry always remains broken, regardless of the number of fermion flavors N_f .

However, $N_f^c \rightarrow \infty$ is in conflict with results from less restrictive approximations, that find a finite number of critical fermion flavors. In consequence, we can conclude that Pisarski’s scheme in isotropic spacetime is not suited to extract any information on chiral dynamics, since it forbids the restoration of chiral symmetry.

More elaborate approximation schemes that allow to study chiral dynamics, are the above mentioned large- N_f /bare vertex, the fully self-consistent DSE solution with the MinBC vertex and the boson model/MinBC vertex scheme. For isotropic spacetime, continuum studies of the second approximation scheme as well as for more complex vertex *ansätze* were performed in [11].

Building on these results, we can evaluate the new gauge boson model in its isotropic form 3.14 and compare the scalar fermion dressing functions in both approximation schemes. The results are shown in Fig. 3.E

The three approximation schemes all lead to an exponentially decreasing order parameter in dependence on the number of fermion flavors. This behavior is known as Miransky scaling [80] and will play a major *rôle* in chapter ?? (finite temperature QED₃). However, despite this common behavior, the critical number of fermion flavors differs for the three truncation schemes. While analytic $1/N_f$ calculations yield $N_f^{c,1/N_f} \approx 3.24$ [72], the self-consistent DSE calculation including the more elaborate 1BC-vertex leads to $N_f^{c,1BC} \approx 3.56$. Judging from Fig. 3.E, $N_f^{c,model}$ is smaller than $N_f^{c,1/N_f}$ but still $N_f^{c,model} \approx 3$.

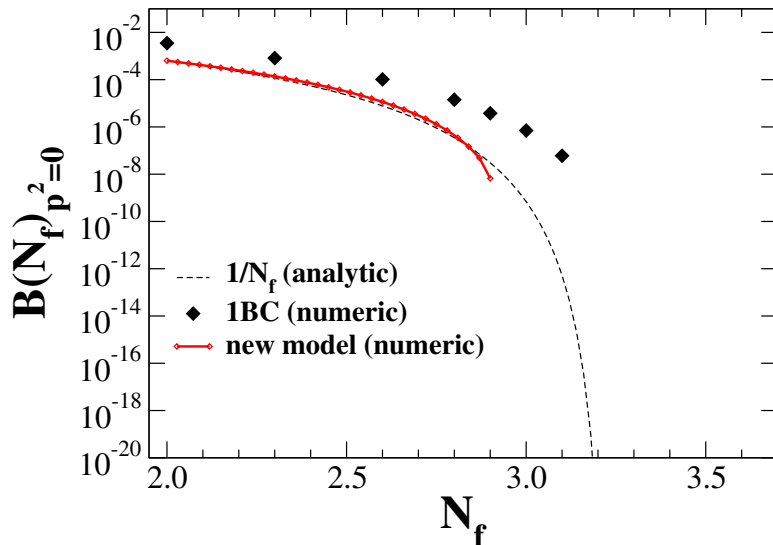


Figure 3.E: The scalar fermionic dressing function evaluated at zero momentum for three different approximation schemes: The large- N_f /bare vertex-, large- N_f /1BC vertex and the boson model/MinBC vertex approximation. The scalar fermion dressing function serves as an order parameter for chiral symmetry breaking. Figure courtesy of Christian Fischer.

The reason for this smallness can be understood by comparing the gauge boson in the self-consistent MinBC calculation and in the new model. While the gauge boson is constant in the deep infrared for $N_f < N_f^c$ and decays with a power law only for $N_f > N_f^c$ the model is designed such that the power-law decay is realized also for $N_f < N_f^c$. We therefore suppress the gauge boson's influence in this region, which results in a smaller N_f^c in total. Since this is only a quantitative change, we expect the boson model/MinBC approximation to be a reliable scheme for our qualitative investigation of chiral symmetry breaking in anisotropic spacetime.

The critical N_f^c in the anisotropic case

Before we discuss any results, we specify the chosen finite volume setting. Both phase diagrams discussed in this section were obtained by solving the DSEs on a torus with $L = 600/e^2$ and 20^3 momentum points.

We begin our discussion of the effects of maximal finite anisotropies with the investigation of Pisarski's scheme. Although Pisarski's scheme is based on an assumption that was found to be insufficient [72, 73] it was used recently by [59] for several general arguments.

With Pisarski's assumptions, it is possible to analytically derive an expression for the scalar fermion dressing function, that is to say the fermionic mass in this scheme. We obtain the analytic expression for equal anisotropic velocities $v_f = v_\Delta$, with the details given in

App. A.3. Our derivation yields

$$m = B(0) = c \alpha \exp \left[\left(-\pi^2 N_f \sqrt{v_f^2 - 1} \right) / \right. \\ \left. \left(2 \sqrt{v_f^2 - 1} + 2(2 + v_f^2) \arctan(\sqrt{v_f^2 - 1}) \right) \right]. \quad (3.26)$$

This result is clearly different from the result presented [59] that we consider erroneous since it does not reduce to the expected isotropic limit as discussed by Pisarski [71]. In contrast, when examining our formula (Eq. (3.26)), we find that it indeed reduces to the expected isotropic limit. Furthermore, it implies that chiral symmetry is always broken in Pisarski's scheme in three dimensions, since $N_f^c \rightarrow \infty$.

We therefore consider Eq. (3.26) to be a reasonable generalization of the isotropic approximation. Consequently, we consider this approximation inappropriate for any further analysis of the quantitative behavior of N_f^c with (c_s, v_f, v_Δ) .

This conclusion leads us to the investigation of the more sophisticated approximation schemes. The next improvement would be to consider the $1/N_f$ -approximation/bare vertex scheme. The resulting phase diagram for the critical number of fermion flavors in dependence on the anisotropic velocities is shown in Fig. 3.F. We encode the critical N_f in a colored density plot, including contour lines to guide the eye. Notice that the coarseness of the contour lines results from the interpolation between the evaluated points. If evaluated at infinitely many points, we would expect the contour lines to smoothen.

As remarkable points, we find a plateau around the isotropic point at $v_f = v_\Delta = 1$ with a critical number of fermion flavors of $N_f^{c,1/N_f} \approx 1.0$. Compared to the isotropic continuum results, we obtain an estimate of the size of our finite volume effects. The comparison yields roughly a factor of three difference between the continuum and our finite volume calculations. This estimate is, strictly speaking, only valid at the isotropic point in the phase diagram since the finite volume effects could depend on the anisotropic velocities, too. This needs to be investigated in a separate study that we will discuss in the next section.

Changing the anisotropic velocities beyond the plateau around the isotropic point, we find an increasing critical number of fermion flavors. This finding remains no matter if v_f and v_Δ are varied simultaneously or independently. Comparing this result to earlier Dyson–Schwinger studies in the $1/N_f$ -expansion under the constraint of small anisotropies of Lee and Herbut, we confirm the results of [20]. In addition, our studies demonstrate that the findings remain also valid for large anisotropies within the frame of the $1/N_f$ -approximation/bare vertex scheme.

We proceed to investigate the validity of these results in an improved approximation scheme, in particular because of the above discussed concerns with respect to the $1/N_f$ -approximation. Our last and most elaborate approximation scheme investigated in this work is the boson model Eq. (3.15)/MinBC Eq. (3.9) scheme. The phase diagram obtained from this scheme is depicted in Fig. 3.G. The critical number of fermion flavors is color-coded and additionally indicated by contour lines, same as in the previous phase diagram. Already at first glance, we find a widely changed behavior of the critical number of fermion flavors compared to the previous approximation scheme.

We firstly focus on the isotropic point and find a critical value for the fermion flavors of $N_f^{c,model} \approx 1.1$. This value is only slightly deviating from the findings in the $1/N_f$ -

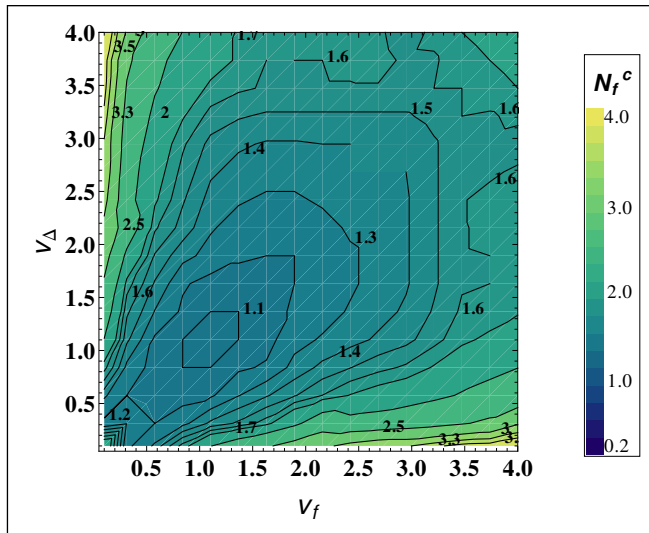


Figure 3.F: The phase diagram for the critical number of fermion flavors N_f^c in dependence on the fermionic anisotropic velocities (v_f, v_Δ). To obtain this diagram, we solved the DSEs as given in Eq. (3.16) and Eq. (3.17) self-consistently in the $1/N_f$ -approximation/bare vertex approximation scheme. The contours serve to guide the eye.

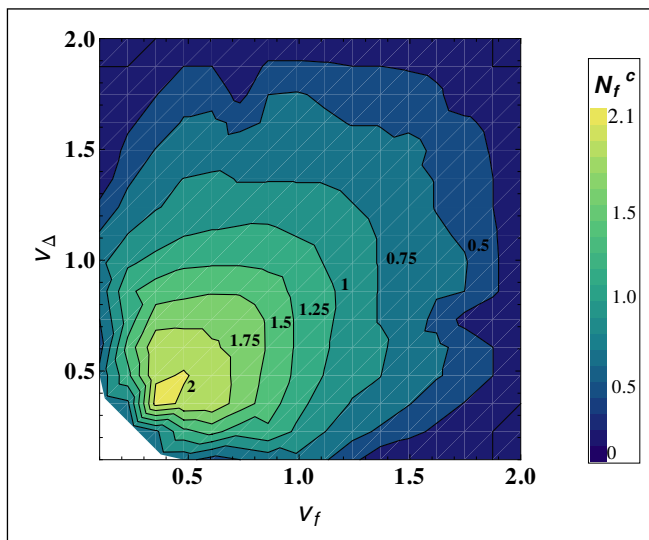


Figure 3.G: The phase diagram for the critical number of fermion flavors N_f^c in dependence on the fermionic anisotropic velocities (v_f, v_Δ). To obtain this diagram, we solved the DSEs as given in Eq. (3.16) and Eq. (3.17) self-consistently in the boson model Eq. (3.15)/MinBC vertex Eq. (3.9) approximation scheme. The contours serve to guide the eye.

approximation/bare vertex scheme. Consequently, the comparison with the continuum results yields the same estimate of finite volume effects. However, as far as remarkable points in the phase diagram are concerned, the isotropic point is no longer featured. In fact, we find

instead a small plateau around $(v_f, v_\Delta) = (0.4, 0.4)$ with a critical number of fermion flavors of $N_f^{c,model} \approx 2$. The plateau around this value furthermore represents a region of maxima - a variation of the anisotropic velocities yields a decreasing critical number of fermion flavors. Varying the anisotropic velocities, the critical number of fermion flavors now decreases. However, it never vanishes for v_f and v_Δ smaller than $c_s = 1$. In contrast, if one of the velocities v_f or $v_\Delta \approx 2$ the critical number of fermion flavors vanishes and the theory always remains in the chirally symmetric phase. On a qualitative level, our findings are in accordance with other, complementary approaches.

On the one hand, a corresponding investigation was conducted by [59]. The authors analyzed the strength of a one-boson exchange between two fermions in order to access the critical number of fermions. Their underlying assumption is the so-called 'Lindemann-criterion' for QED₃, that does not claim to be exact but in general provides an accurate description. It states that a fermion mass will be dynamically generated as soon as the photon exchange interaction between two fermions is stronger than some threshold value A_c . This threshold value, and the related critical number of fermion flavors is obtained from an analysis of the according S-matrix up to second order perturbation theory with another assumption: that this threshold value is not influenced by anisotropy. The framework of [59] represents a rather different perspective on the problems considered in this chapter. Although our results agree with the findings in the one-boson exchange model, the advantage of the DSE formalism can be seen in the fact that there is no need for assumptions as strong as in [59], no matter how plausible they may be.

On the other hand, our findings from Fig. 3.G are in agreement with lattice calculations of Hands et al. [66, 79] that provide results at only few distinct points of the phase diagram. While the setting of lattice gauge theory and our finite volume DSE approach are very similar at the first sight, the lattice gauge theory approach struggles with the large separation of scales in QED₃. As we discussed above, this scale separation requires large volumes, that are hardly accessible on the lattice. Employing smaller lattices however has the drawback that the infrared and UV cutoff influence the results considerably. On the torus, in contrast, the effects of the infrared cutoff can be removed by an appropriate choice of the lattice spacing L , *i.e.* larger box volumes. However, we should remark again that the critical numbers in Fig. 3.G nevertheless suffer from rather large finite volume effects, reducing their absolute value. In summary, we consider our finite volume DSE approach to be better suited than the lattice to investigate the anisotropic phase diagram, since our approach is not restricted to certain values of anisotropy.

We conclude the presentation of the phase diagrams with a comment on the large- N_f /bare vertex approximation scheme. It ignores essential features regarding the criticality of N_f in dependence on the anisotropic velocities. The results in this approximation scheme are conflictive with findings in more elaborate approximation schemes. Therefore, to our mind, the large- N_f /bare vertex scheme should not be used for further analysis in HTS-QED₃.

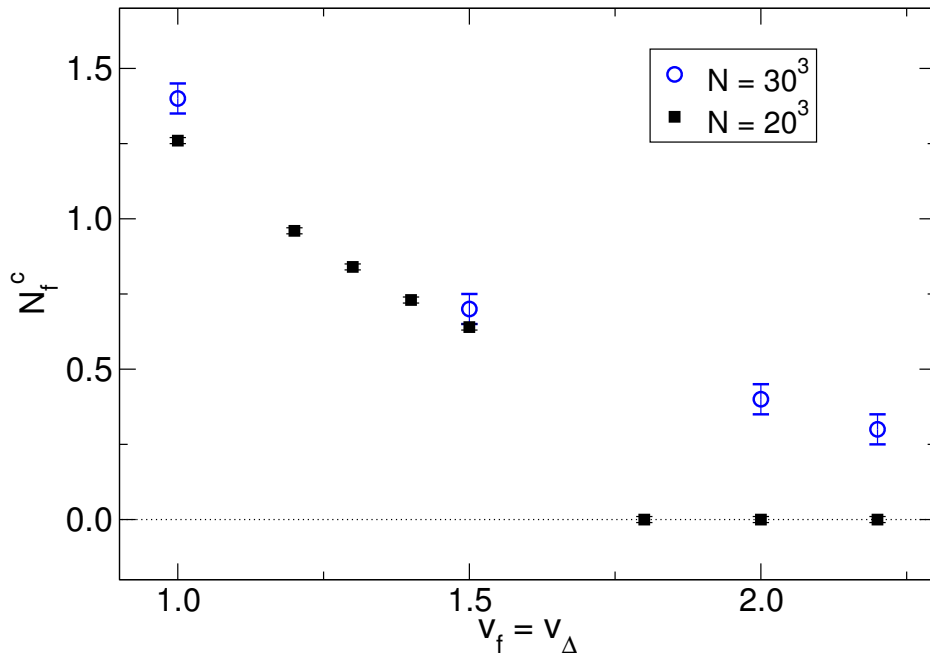


Figure 3.H: We show the critical number of fermion flavors obtained from two different tori with $N = 20^3$ and $N = 30^3$ corresponding to box lengths of $Le^2 = 600$ and $Le^2 = 900$, for four selected points on the $v_f = v_\Delta$ -axis.

Volume effects

From the comparison with the isotropic continuum results, we already found a sizable difference in the critical number of fermion flavors. At the isotropic point $v_f = v_\Delta = c_s = 1$, the finite volume reduced the critical number of fermion flavors by about a factor of three. So far, we stated that we assume these differences to finite volume effects without further investigations. We now come back this issue.

For isotropic spacetime, a detailed volume study with torus sizes up to $N = 512^3$ was discussed in [75]. Although it would be preferable to perform an analogous analysis in anisotropic spacetime, the enormously increased demand of CPU time renders this an impossible endeavor. In anisotropic spacetime, already the solution of the equations on a torus with $N = 20^3$ consumes a considerable amount of time. Since it is nevertheless desirable to have at least a first estimate of the dependence of the finite volume effects on the anisotropic velocities, we picked four points on the $v_f = v_\Delta$ axis and solved the DSEs on a torus of $N = 30^3$ points. The results of this study is displayed in Fig. 3.H.

Firstly, we find a larger value of N_f^c for all four values of $v_f = v_\Delta$ in the larger volume. This was expected from the comparison at the isotropic point. However, we also find that the amount by which the critical number of fermion flavors is shifted, is rather similar at $v_f = v_\Delta = 1$ and $v_f = v_\Delta = 1.5$. We therefore do not expect qualitative changes concerning the overall behavior of N_f^c in the phase diagram that was discussed above. Furthermore, we observe that the vanishing of N_f^c shifts to anisotropies $v_f = v_\Delta > 2.2$ for the larger volume. This strong volume behavior supports the necessity of further, more detailed volume studies as they were presented in [75]. Finally, it would be even more desirable to have a comparison with continuum results. A detailed continuum study of the case $v_f = v_\Delta$ is under way.

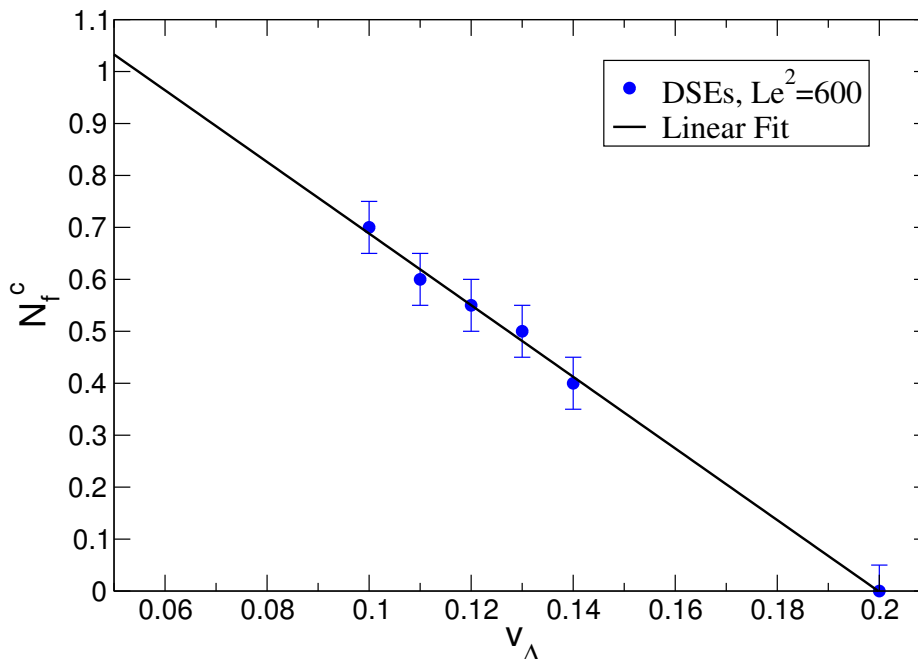


Figure 3.I: Selected results for the critical number of fermion flavors at $(v_f, v_\Delta) = (10v_\Delta, v_\Delta)$ from a torus with $Le^2 = 600$. The error bars correspond to our step size when searching for N_f^c .

The 'physical' case $v_f/v_\Delta \sim 10$

Finally, we return to the experimental motivation behind this QED₃ study in an anisotropic spacetime, the HTS materials. As we mentioned earlier, experiments find an intrinsic anisotropy, that is the ratio $\lambda = v_f/v_\Delta$, in the range of 10 - 20 for different HTS materials. For instance, ref. [81] reports $\lambda = 14$ for optimally doped YBa₂Cu₃O₇ and $\lambda = 19$ for Bi₂Sr₂CaCu₂O₈ compounds. Unfortunately, only the ratios of the anisotropic velocities seem to be accessible for the experiment up to now.

It is therefore impossible to identify the exact location of a certain material in the anisotropic phase diagram. Nevertheless, one can highlight the regions in the phase diagram, where the measured anisotropy ratios could be located. We chose $(10v_\Delta, v_\Delta)$ to represent a possible set of anisotropies and evaluated the region of the phase diagram that is accessible for our model. The results are shown in Fig. 3.I, with the calculated points indicated by circles. The black line represents a linear fit to our data, that approximates the points in an adequate way.

As we already discussed above, the critical numbers of fermion flavors are affected by finite volume artifacts. However, as we have seen from Fig. 3.H, these artifacts are only mildly depending on the anisotropic velocities for finite numbers of fermion flavors. In a first volume extrapolation, we therefore make use of the results obtained in isotropic spacetime (see [75]). In this work, a functional form of the linearly extrapolated critical number of fermion flavors for infinite volumes was given by

$$N_f^c = a - \frac{b}{(Le^2)^{1/3}}. \quad (3.27)$$

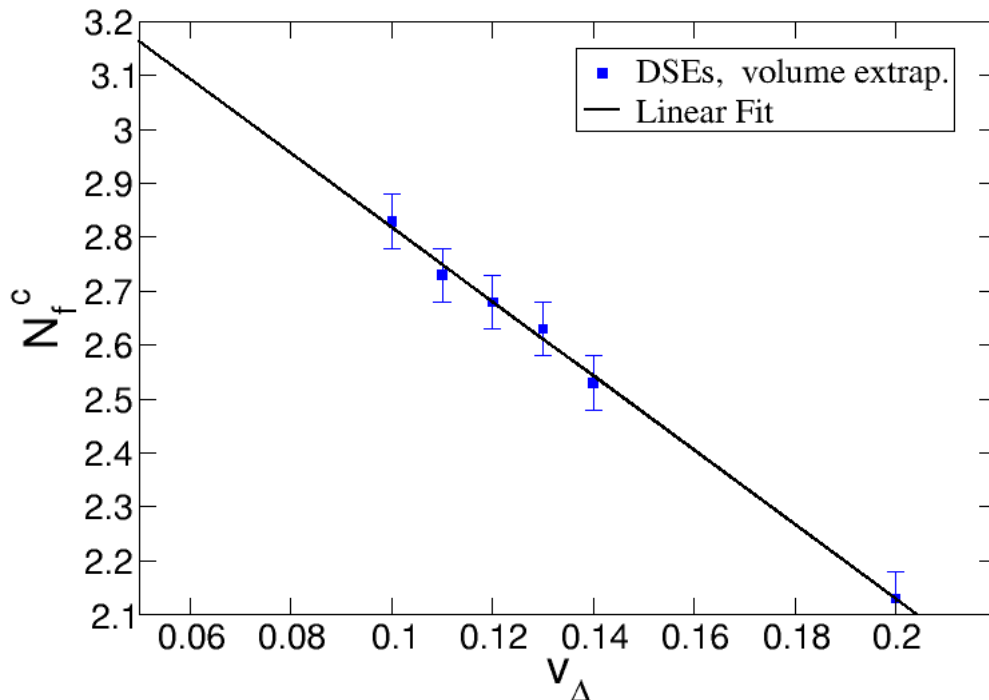


Figure 3.J: Volume extrapolated critical numbers of fermion flavors at $(v_f, v_\Delta) = (10v_\Delta, v_\Delta)$, originally obtained from a torus of $Le^2=600$. The error bars correspond to our step size when searching for N_f^c .

With the help of the isotropic point in the phase diagram 3.G and the isotropic critical number of fermion flavors $N_f^{c,isol} = 3.24$, we determine the parameter $b = 17.97$. It is then possible to compute the volume extrapolated critical numbers of fermion flavors (in Eq. (3.27) denoted by a) from the finite volume critical numbers of fermion flavors displayed in Fig. 3.I. The results are shown in Fig. 3.J.

Nevertheless, one has to keep in mind that this linear behavior might be changed in the infinite volume limit. This clearly represents a next point that needs to be studied carefully in future investigations.

3.1.5. Summary

This chapter reported on the investigations of finite anisotropies of in principle arbitrary size in QED₃ in a Dyson–Schwinger framework. To obtain these results, we introduced a consistent approximation scheme beyond the leading order large- N_f expansion and analyzed the criticality of the number of fermion flavors for chiral symmetry breaking.

Our findings include an increasing critical number of fermion flavors with increasing anisotropic velocities as long as $v_f < 1$ and $v_\Delta < 1$ are both satisfied. For v_f or $v_\Delta > 1$, we find the opposite behavior, that is a decreasing N_f^c . These results agree with both results from lattice gauge theory [66, 79] and from continuum analysis of the fermion-photon interaction strength [59] on a qualitative level.

However, we found that our results are affected quantitatively by considerable finite volume artifacts. Due to the large demand of computational effort, a detailed volume study as done in isotropic spacetime [75] is not possible to date. First steps towards larger volumes in anisotropic spacetime showed only a small qualitative impact of the anisotropic velocities on finite volume effects. Therefore, we consider it a reasonable approximation to neglect this possible dependence and hence to employ the finite-volume correction deduced from detailed studies at the isotropic point to the anisotropic case. We employed the linear extrapolation of the critical number of fermion flavors to formulate predictive critical numbers of fermion flavors for 'physical' regions of the anisotropic phase diagram. Nevertheless, a detailed finite volume study is desirable to quantify the finite volume effects beyond this approximation.

Additionally, future investigations should address two more central aspects of our investigations. Firstly, it is desirable to perform an analysis of different fermion-boson vertex *ansätze*. Though we know from isotropic investigations [11] that our vertex truncation errors should be moderate, a detailed study for anisotropic spacetime is pending and could overcome any doubts. A second point concerns the gauge boson approximation. Although our model for the gauge boson vacuum polarization includes important features of the infrared behavior of the full function, more elaboration on the self-consistent solution of the gauge boson DSE is necessary.

Despite these important points for future investigations, we consider our results to be a further, qualitatively reliable step towards an understanding of QED₃ with respect to its application to high temperature superconductors.

3.2. QED₃ at finite temperature

Introducing finite temperatures to QED₃ is interesting for several reasons. On the one hand, considering finite temperatures clearly is a step towards a more realistic description of HTS materials and therefore a reasoned extension of the investigations presented in the previous chapter.

On the other hand, QED₃ is a strongly coupled and asymptotically free theory. Several works argued for the existence of a pseudo conformal window, in analogy to many flavor QCD that received a lot of attention recently, especially in the frame of renormalization group studies [29, 82–86]. An aspect of great interest in these studies was the scaling close to the quantum critical point of chiral symmetry breaking. It was argued, that pure exponential Miransky scaling is only valid in certain limits of a more general, universal scaling law [86]. The assumptions under which this universal scaling was derived, are also fulfilled by QED₃ and a closer investigation of the scaling region is in order.

To perform this analysis, we generalize the boson model/MinBC approximation scheme that was already employed in zero temperature calculations (see previous chapter and also [49]). The results of these investigations agreed with corresponding ones in complementary approaches [59, 79] on a qualitative level. With the feasibility at vanishing temperatures shown, we dare to firstly tackle the combined problem of finite anisotropies and finite temperatures in our approach. To our knowledge, this problem has not been approached either in a Dyson–Schwinger framework or in any other approach.

The employed finite volume setting was introduced in section 3.1.3. In this framework, the consideration of finite temperatures is comparably easy: Since the finite box lengths leads to sums over discrete Matsubara frequencies, the setting more or less lends itself for the intended investigations. However, we need to take care to guarantee a large enough aspect ratio between the number of modes in temporal and spatial direction for the temperature interpretation to hold.

This chapter is organized as follows: in section 3.2.1, we will introduce the DSEs at finite temperature as they are employed for all following investigations in this chapter. As a next step, we will summarize the most important aspects of the universal scaling law introduced by [84, 86] in section 3.2.2. Finally, we will present our numerical results in section 3.2.3 regarding the chiral phase transition in finite temperature QED₃ in an anisotropic spacetime. Here, we first discuss the finite temperature phase diagram for the critical number of fermion flavors depending on the anisotropic velocities. Next, we address the investigations of the scaling behavior of the critical temperature in dependence on the number of fermion flavors.

3.2.1. Finite temperature DSEs

Since we work in the identical approximation scheme as for vanishing temperature, the Dyson–Schwinger equation formulation in the finite volume does not change. However, the introduction of finite temperatures slightly changes the continuum formulation of the equations that represents our starting point. We therefore shortly discuss the equations for completeness.

Finite temperature is introduced by compactifying the time direction. In Euclidean spacetime, the DSE for the quark propagator is then explicitly given by

$$S_{F,j}^{-1}(\omega_p, \vec{p}) = S_{0,j}^{-1}(\omega_p, \vec{p}) + Z_1 e^2 T \sum_{n_i} \int \frac{d^2 q}{(2\pi)^2} (\sqrt{g_{j,\mu\alpha}} \gamma^\alpha S_{F,j}(\omega_q, \vec{q}) \times \sqrt{g_{j,\nu\beta}} \Gamma^\beta(\omega_q, \vec{q}, \omega_p, \vec{p}) D_{\mu\nu}(\omega_k, \vec{k})), \quad (3.28)$$

$$D_{\mu\nu}^{-1}(\omega_p, \vec{p}) = D_{0,\mu\nu}^{-1}(\omega_p, \vec{p}) - \frac{Z_1 e^2 T N_f}{2} \sum_{j=1,2} \int \frac{d^2 q}{(2\pi)^2} \text{Tr} \left[\sqrt{g_{j,\mu\alpha}} \gamma^\alpha S_{F,j}(\omega_q, \vec{q}) \times \sqrt{g_{j,\nu\beta}} \Gamma^\beta(\omega_p, \vec{p}, \omega_q, \vec{q}) S_{F,j}(\omega_k, \vec{k}) \right]. \quad (3.29)$$

Here, the bosonic momentum k_μ is defined by the difference of the external and the internal fermion momenta $p_\mu - q_\mu$. The nodal index is denoted by $i = 1, 2$.

$S_{0,j}^{-1}(p) = Z_2 i \gamma_\nu \sqrt{g_{j,\nu\mu}} p_\mu$ denotes the inverse bare fermion propagator that depends on the momenta $p = (\omega_p, \vec{p})$ with the Matsubara frequency ω_p . The inverse bare gauge boson propagator reads $D_{0,\mu\nu}^{-1}(p) = Z_3 p^2 P_{\mu\nu}^T(p)$, with the transverse projector denoted by P^T .

The dressed fermion-boson vertex is denoted by $\Gamma^\beta(p_\mu, q_\mu)$ and will be replaced by the ansatz Eq. (3.9). Furthermore, the equations Eq. (3.28) and Eq. (3.29) include the renormalization constants Z_1 , Z_2 and Z_3 of the vertex, fermion and gauge boson. They are defined by the ratio between renormalized to unrenormalized dressing function of the corresponding one-particle irreducible Green's function. However, due to the UV-finiteness of QED₃, we can set the renormalization constants to one. Notice that the Ward identity $Z_1 = Z_2$ is then trivially satisfied. The dressed fermion and gauge boson propagator read

$$S_{F,i}^{-1}(\omega_p, \vec{p}) = B_i(\omega_p, \vec{p}) + i \sqrt{g_i^{\mu\nu}} \gamma_\nu \tilde{p}_{\mu,i}, \quad (3.30)$$

$$D_{\mu\nu}(\omega_p, \vec{p})^{-1} = p^2 \left(\delta_{\mu\nu} - \frac{p_\mu p_\nu}{p^2} \right) + \Pi_{\mu\nu}(\omega_p, \vec{p}), \quad (3.31)$$

where we inserted the explicit form of the transverse projector P^T and made use of the shorthand notation introduced in Eq. (3.5) and Eq. (3.6).

We conclude the collection of finite temperature DSEs by stating the projected and traced DSEs for the fermionic dressing functions. They are given by

$$B_i(\omega_p, \vec{p}) = T e^2 \sum_{n_i} \int \frac{d^2 q}{(2\pi)^2} \frac{B_i(\omega_q, \vec{q}) g_i^{\mu\nu} D_{\mu\nu}(\omega_k, \vec{k})}{B_i(\omega_q, \vec{q})^2 + (\tilde{q}_{i,\mu})^2}, \quad (3.32)$$

$$A_{\mu,i}(\omega_p, \vec{p}) = 1 - \frac{T e^2}{p_\mu} \sum_{n_i} \int \frac{d^2 q}{(2\pi)^2} \left\{ \frac{2(\tilde{q}_{\lambda,i} g_i^{\lambda\nu} D_{\mu\nu}(\omega_k, \vec{k})) - \tilde{q}_{\mu,i} g_i^{\lambda\nu} D_{\lambda\nu}(\omega_k, \vec{k})}{B_i(\omega_q, \vec{q})^2 + (\tilde{q}_{i,\mu})^2} \right\} \times \frac{A_{\mu,i}(\omega_p, \vec{p}) + A_{\mu,i}(\omega_q, \vec{q})}{2}. \quad (3.33)$$

Notice that the above equations still do not include the summation over the external index μ . For the gauge boson vacuum polarization, we employ our model ansatz Eq. (3.15). For more information on this ansatz, see section 3.1.3. We proceed with the evaluation of Eq. (3.32) and Eq. (3.33) for equal fermionic velocities $v_f = v_\Delta$. This choice reduces the number of vectorial fermion dressing functions, since $A_0(\omega_p, \vec{p}) \neq A_1(\omega_p, \vec{p}) = A_2(\omega_p, \vec{p})$. Furthermore, the nodes are no longer distinguishable and we can drop the nodal index i .

3.2.2. Critical Scaling

Critical scaling in the vicinity of quantum critical points allows the definition of universality classes. A distinguishing feature of pseudo conformal phase transitions is the so-called Miransky scaling that can be seen as a higher dimensional generalization of BKT scaling. A candidate for such a phase transition are the chiral phase transitions in QED₃ and QCD, triggered by an increase in the number of fermion flavors. Discussions thereof can be found in several works, *e.g.* [9–11, 30, 80].

The derivation of Miransky-type scaling is based on rather general assumptions, including the fixed point structure of a gauge theory, as we shortly discussed in sec. 2.3 with the help of a toy model. In close analogy to this toy model, Miransky scaling is derived from the β function of the four fermion coupling in *e.g.* QED₃. In the gauge theory, one assumes a constant gauge coupling g ,

$$\partial_t g^2 = 0. \quad (3.34)$$

This can be seen as a reasonable approach close to an IR fixed point of the gauge coupling. From the flow equation of the four fermion coupling, one can then derive the scaling behavior of the symmetry breaking scale, which we denote by k_{SB} ,

$$k_{SB}^M \sim \Lambda \theta(g^2 - g_{cr}^2) \exp\left(-\frac{\pi}{2\epsilon \sqrt{g^2 - g_{cr}^2}}\right). \quad (3.35)$$

The coupling g_{cr} is the critical value for the fixed point merger that we discussed briefly in sec. 2.3. The constant ϵ has to be determined from the actual theory in consideration. The scaling behavior of the critical scale can be transferred to the scaling behavior of IR observables, that was found in *e.g.* isotropic QED₃ [11].

However, a more careful analysis of the dependence of the symmetry breaking scale on the number of fermion flavors has been performed in [84, 86]. In this work, the RG flow of the running coupling has been taken into account. To leading order the scaling of the symmetry breaking scale is then given by

$$k_{SB} \sim k_0 \theta(N_f^c - N_f) |N_{f,0}^c - N_f|^{-\frac{1}{\Theta_0}} \exp\left(\frac{\pi}{2\epsilon \sqrt{|N_f^c - N_f|}}\right). \quad (3.36)$$

The constant k_0 serves to fix the scale and the critical number of fermion flavors for chiral symmetry breaking is denoted by N_f^c . The exponent Θ_0 is the leading order term in a Taylor expansion of the critical exponent Θ in N_f and further, the theory dependent parameter ϵ (see Ref. [86] for details). It is furthermore possible to relate the scaling behavior of the symmetry breaking scale to the scaling behavior of observables as *e.g.* the critical temperature. This leads to

$$T_{cr} \sim k_0 |N_{f,0}^c - N_f|^{-\frac{1}{\Theta_0}} \exp\left(-\frac{\pi}{2\epsilon \sqrt{|N_{f,0}^c - N_f|}}\right), \quad (3.37)$$

with a scale k_0 and the critical value $N_{f,0}^c$ of fermion flavors at zero temperature. More details on the parameters and their dependence on the theory in question can be found in Ref. [86]. In leading order, this yields a power law decay

$$T_{cr} = k_0 |N_{f,0}^c - N_f|^{-\frac{1}{\Theta_0}}. \quad (3.38)$$

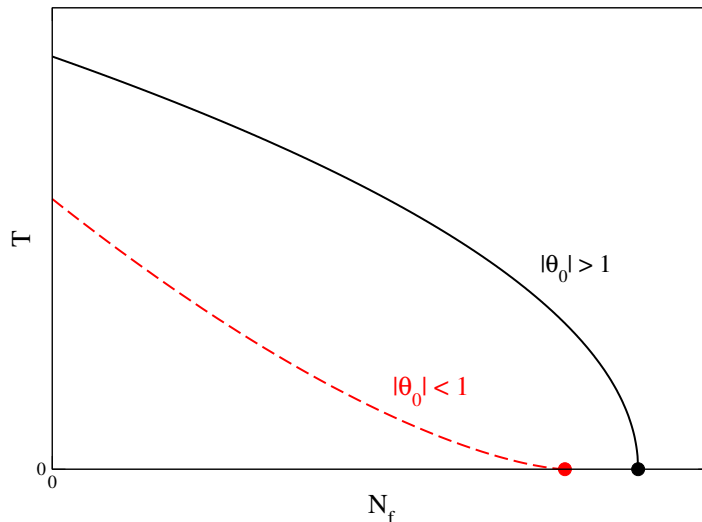


Figure 3.K: The generic thermal transition lines for the cases $|\Theta_0| < 1$ and $|\Theta_0| > 1$. The quantum critical points for zero temperature are marked with filled circles.

This relation (Eq. (3.38)) only represents an upper bound for the chiral critical temperature, as it is insensitive to deep infrared behavior of the [86, 87]. Especially fluctuations of Goldstone modes can affect the chiral condensate in the deep IR and consequently the critical temperature. In general, it is a very challenging task to investigate the full scaling law as introduced in Eq. (3.36) in a finite volume setting, as *e.g.* our three torus⁵. The reason for this challenge are the scales present in QED₃: The scale set by the dimensionful coupling $\alpha = N_f e^2 / 4\pi$ and that of the dynamically generated fermion mass. Close to the critical number of fermion flavors at vanishing temperature, $N_{f,0}^c$, these two scales differ largely. In principle one therefore needs large volumes, respectively a DSE continuum formulation [75], in order to fully analyze the scaling features.

However, even though we cannot resolve the exponential Miransky scaling that dominates only in the close vicinity of $N_{f,0}^c$ (see Table 2 in Ref. [88] for an estimate of the size of this region) in our torus setting, we can concentrate on the 'intermediate' scaling behavior. That is, we strive to find and analyze the power law part of the scaling relation Eq. (3.36) that dominates further away from $N_{f,0}^c$ before the end of the scaling region around $N_{f,0}^c$ is reached. In consequence, we consider (Eq. (3.38)) as a reasonable approximation for our investigations. Considering Eq. (3.38) there are two possible generic scaling scenarios. They emerge from the absolute value of the critical exponent $|\Theta_0| < 1$ or $|\Theta_0| > 1$. Both scenarios are illustrated in Fig. 3.K. In the case of $|\Theta_0| > 1$ the thermal phase transition line approaches the quantum critical point with an infinite slope. For $|\Theta_0| < 1$ the slope vanishes at the quantum critical point, which corresponds to large power law corrections to the exponential Miransky scaling.

⁵or Lattice gauge theory

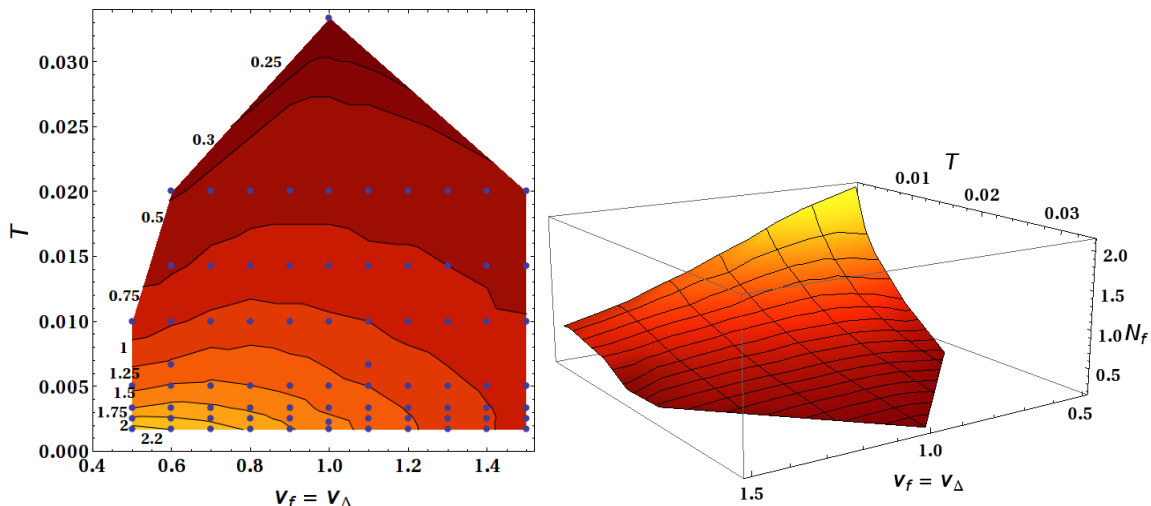


Figure 3.L: The phase diagram for the critical number of fermion flavors N_f^c in dependence on the anisotropic velocities $v_f = v_\Delta$ and temperature T . The left panel shows the planar phase diagram with N_f^c highlighted in different colors and separated by contour lines. Dots indicate the actually evaluated parameter sets. The right panel shows the same phase diagram with N_f^c as vertical axis. The slope of decreasing N_f^c with increasing T clearly is larger for $v_f = v_\Delta \geq 1$ than for $v_f = v_\Delta \leq 1$

3.2.3. Numerical Results

This section presents our numerical results of the investigation of QED₃ at finite temperatures and anisotropies. We will mainly discuss the case $v_f = v_\Delta$ and $c_s = 1$, which correspond to the diagonal of the anisotropy phase diagrams presented in chapter 3.1.4. We chose this cut through the phase diagram to make our results better presentable. It is no problem to compute finite temperature phase diagrams for any off-diagonal anisotropy $v_f \neq v_\Delta$. We will start with the discussion of the generalized phase diagram for the critical number of fermion flavors depending on temperature and anisotropic velocities. Next, we proceed with a closer analysis of 'slices' of the computed phase diagram: We are interested in the critical behavior of the thermal phase transition line in the vicinity of the quantum critical point.

The critical N_f^c in the anisotropic case $v_f = v_\Delta$

We start our discussion with the phase diagram for the critical number of fermion flavors depending on the anisotropies $v_f = v_\Delta$ (with $c_s = 1$) and the temperature T . The results are obtained from solving the DSEs (Eq. (3.16)) and (Eq. (3.17)) on a three torus of $(N_X^2 = 39^2) \times (N_T = 23)$ points and a box length of $e^2 L_X = 600$. By introducing finite temperatures on the torus, we have to take care to guarantee a reasonable aspect ratio between the temporal and the spatial number of lattice points. The choice of $N_T = 23$ satisfies this demand.

We are interested in the influence of temperature and anisotropy on the restoration of chiral symmetry. As we discussed in chapter 2, a natural order parameter sensitive to the breaking/restoration of this symmetry would be the chiral condensate, with tr_D indicating the trace

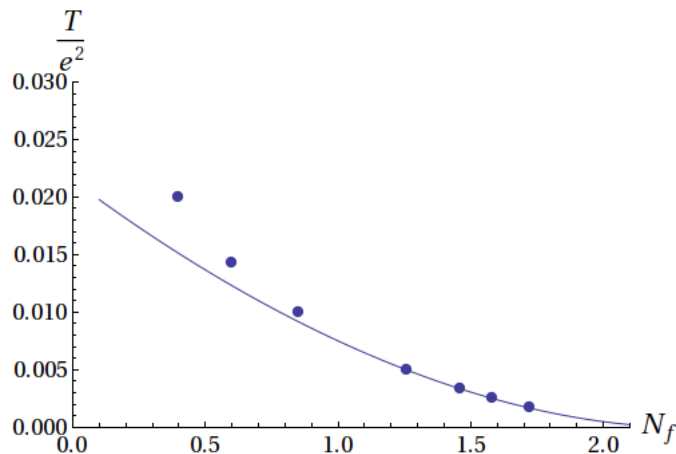


Figure 3.M: Fit to the critical temperature for chiral symmetry breaking in dependence on the number of fermion flavors for a fixed anisotropy $v_f = v_\Delta = 0.8$. The blue dots represent our data that is fitted by a power law (3.38) (straight line). The fit region encompasses the region close to the quantum critical point, for this case $N_f > 1.25$.

over Dirac indices,

$$\langle \bar{\Psi}\Psi \rangle = T \sum_{n_t} \int \frac{d^2q}{(2\pi)^2} \text{tr}_D S_F(\omega_q, \vec{q}). \quad (3.39)$$

In close connection to the chiral condensate, the scalar fermion dressing function at any momentum serves equally well as an order parameter. We chose to analyze the behavior of $B(\omega_q, \vec{q})$ at the lowest Matsubara frequency and two-momentum in order to determine the critical number of fermion flavors. The results of this analysis are shown in Fig. 3.L.

The phase diagram displays the critical number of fermion flavors, distinguishable by color and by contour lines, depending on temperature and anisotropic velocities $v_f = v_\Delta$. The grid of evaluated points is indicated by dots and the contour lines serve to guide the eye. Their edged structure results from the (Mathematica) interpolation of the coarse grid and is assumed to smoothen for a finer and finer grid. In the white regions of the phase diagram, the convergence criterion of the iterative solution process is not matched for any nontrivial number of fermion flavors.

For effectively vanishing temperature, we find a decreasing N_f^c for increasing anisotropies. This is in accordance with the findings discussed in chapter 3.1.4. However, the actual values for N_f^c differ slightly since we used similar but not identical torus sizes. At fixed anisotropy, the critical number of fermion flavors also decreases with an increasing temperature. This behavior generally holds for any studied degree of anisotropy. However, for $v_f = v_\Delta \geq 1$ the slope of the decrease is considerably smaller than for $v_f = v_\Delta \leq 1$ (see right panel in Fig. 3.L).

Critical Scaling

We now proceed to analyze the critical scaling of the temperature in dependence on the number of fermion flavors. As we discussed above, we do not expect to see the full scaling

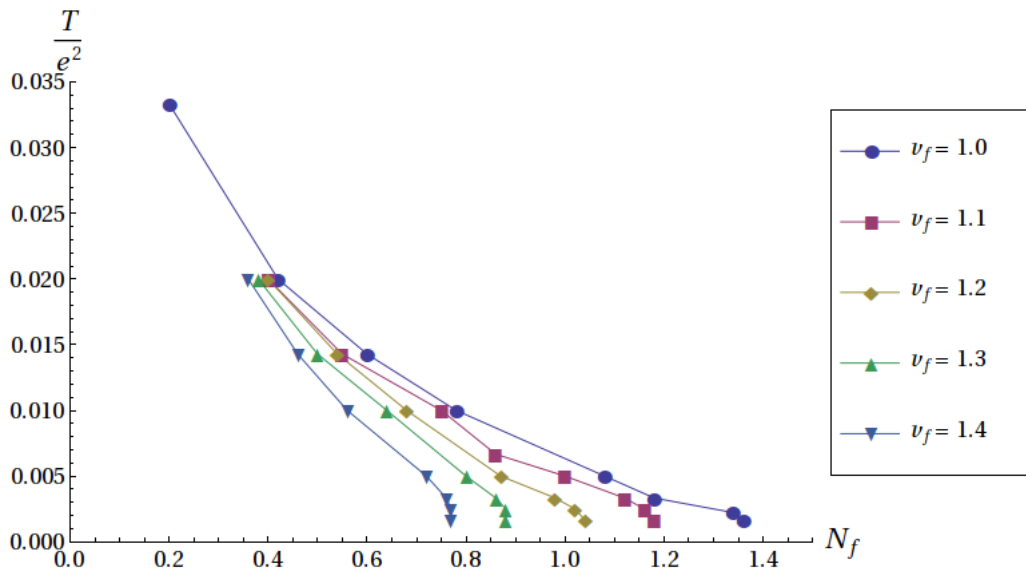


Figure 3.N: The critical temperature in dependence on the number of fermion flavors for anisotropic velocities from $v_f = v_\Delta = 1.0$ to $v_f = v_\Delta = 1.4$. The connecting lines between the dots are added for clarity, they do not represent a fitting function. We concentrated on this velocity range since the curves are nicely distinguishable. It could be extended to larger anisotropic velocities without any problems, however the clarity of demonstration would suffer. It is clearly visible that the size of the region of power law scaling decreases. Compare also the transition between the two generic scaling scenarios in Fig. 3.K.

behavior of Eq. (3.36) in our three torus setting, since we are limited in volume and lattice size. We therefore focus on an analysis of the intermediate scaling region. To this end, we need to identify the region where the power law scaling

$$T_{cr} \sim k_0 |N_{f,0}^c - N_f|^{-\frac{1}{\Theta_0}} \quad (3.40)$$

provides a valid description, separately for all anisotropic velocities $v_f = v_\Delta$. For instance, we consider the case $v_f = v_\Delta = 0.8$. Figure 3.M displays the calculated critical temperatures depending on the number of fermion flavors (the blue dots). The straight line shows a power law fit of the form Eq. (3.38) in the region $1.25 < N_f < 1.75$. While this N_f range is well matched by the fit function, the region $N_f < 0.9$ clearly lies outside the scaling region. The value of $N_f \approx 0.9$ marks its lower end. Furthermore, we do not find the critical region where Miransky scaling dominates the power law scaling. As we discussed above, this is expected due to the limited resolution in the finite volume. However, this region can be located at $N_f > 1.75$, somewhere close to $N_{f,0}^c$. A more thorough investigation of this scaling region is a possible subject for a future investigation, based on a continuum formulation of the DSEs. The fit of the data points in Fig. 3.M yields the value for the critical exponent $|\Theta_0| = 0.5$ and for the critical number of fermion flavors at zero temperature, $N_{f,0}^c = 2.2$. We proceed with the same analysis of the critical temperatures for anisotropic velocities in the range of $v_f = v_\Delta = 0.6 - 1.5$. A first finding is that the extent of the region where we can identify the power law scaling is correlated with the amount of anisotropy. While the intermediate

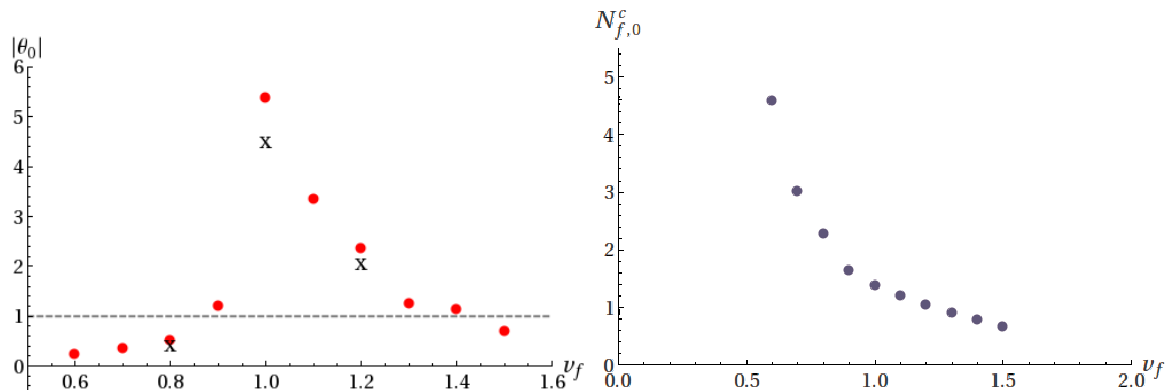


Figure 3.O: The critical exponent Θ_0 plotted as a function of the fermionic velocities $v_f = v_\Delta$. Shown are results for the self-consistent photon model Eq. (3.15) and the 1BC-vertex, in the fermion-DSE.

scaling region is large for $v_f = v_\Delta < 1$, it decreases significantly for $v_f = v_\Delta > 1$. An illustration of this decrease in the size of the power law scaling region can be found in Fig. 3.N.

The complete set of critical exponents $|\Theta_0|$ and critical numbers of fermion flavors for vanishing temperatures, $N_{f,0}^c$ (right panel), can be found in Fig. 3.O. The behavior of the critical exponents (left panel) depending on the anisotropies shows that the fermionic velocities provide an external parameter that allows to tune the generic scaling behavior in the vicinity of the quantum critical point (compare Fig. 3.K and also Fig. 3.N). The red dots indicate the results obtained from a torus of $(N_X^2 = 39^2) \times (N_T = 23)$ points, with a spatial box length of $e^2 L_X = 600$.

The critical exponent peaks at the isotropic point, with a significantly larger value than for smaller or larger anisotropies. While the decrease of $|\Theta_0|$ is rather rapid for $0.5 < v_f = v_\Delta < 0.9$, it decays more slowly with larger anisotropies, $1.1 < v_f = v_\Delta < 1.5$.

In order to get a first intuition for the size of finite volume effects, we further included the critical exponents for selected points obtained from a larger torus. This torus consisted of $(N_X^2 = 59^2) \times (N_T = 23)$ points and we assumed a box length of $e^2 L_X = 900$. We concentrated on these few points since the increase in volume represents an enormous increase in computational time. Thus, we picked representable points at, below and above the isotropic point. The according values of the critical exponent are marked by crosses. As expected from the results in the previous chapter 3.1.4, our critical values are sensitive to finite volume effects. In the case of the critical exponent, these effects augment the actual value of $|\Theta_0|$ at all three anisotropies. We consider this behavior comparable to our findings at zero temperature, presented in the previous section, and conclude that the finite volume affects our critical values mainly quantitatively. As far as finite size effects are concerned, we remind the reader that the dimensionful coupling of QED₃ acts as a UV cutoff for large momenta. In consequence, we expect only mild influence of finite size effects as long as we keep the lattice spacing smaller than this scale, which is true in our calculations. Altogether, we expect the qualitative behavior of $|\Theta_0|(v_f)$ to also hold for larger volumes.

Speaking of the qualitative behavior in the critical region, we recall from [86] that the size of Θ_0 determines the size of power law corrections to exponential Miransky scaling in the close vicinity of the quantum critical point. From the results in Fig. 3.O, we find small corrections for $|\Theta_0| \gg 1$ and large corrections for $|\Theta_0| \ll 1$. $|\Theta_0| \approx 5$ for the isotropic point therefore leads us to expect dominant exponential Miransky-scaling, also in the intermediate scaling region and only very small power law corrections. For large anisotropies and anisotropies $v_f = v_\Delta < 0.9$, the power law scaling dominates. More detailed statements on the scaling behavior are currently not possible due to our finite volume setting, respectively the smallness of the region of exponential Miransky scaling.

However, we can comment on the size of the 'intermediate' scaling region, further away from $N_{f,0}^c$. As we shortly mentioned above, the scaling region for $|\Theta_0| \leq 1$ is rather large, while it is much smaller for $|\Theta_0| > 1$ (compare also Fig. 3.N). This finding agrees with our considerations above and in Ref. [86].

Finally, we address the zero-temperature critical number of fermion flavors that is shown in the right panel of Fig. 3.O. $N_{f,0}^c$ decreases for increasing anisotropies. This finding is in accordance with earlier studies in a zero-temperature torus setting (see sec.3.1). We remark again that the actual critical numbers differ slightly to our previous findings. The reason for this is the usage of similar, but not identical tori as an underlying manifold.

3.2.4. Summary

Section 3.2 presented the results of our investigations of QED₃ at finite temperatures in an anisotropic spacetime. We were interested in the conditions for chiral symmetry breaking, whereas we considered variations of the temperature, the anisotropic velocities and the number of fermion flavors. To carry out our analysis, we solved a coupled set of truncated DSEs for the anisotropic fermion propagator together with model input for the photon self energy determined from the isotropic case at $T = 0$.

Motivated by the application of QED₃ as a low-energy effective theory for high temperature superconductors, we firstly extended the zero temperature phase diagram presented in section 3.1.4 to finite temperatures. We found an overall decreasing critical number of fermion flavors with increasing temperature for all anisotropies. However, we also found that the slope of the decrease in the critical number of fermion flavors depends on the amount of anisotropy and is steeper for $v_f = v_\Delta < 1$ than for $v_f = v_\Delta > 1$.

Secondly, we concentrated on an analysis of the behavior of the critical temperature depending on the number of fermion flavors close to the merger of the thermal phase transition line and the quantum critical point. Refs. [84, 86] suggested the presence of a universal scaling law for strongly coupled asymptotically free gauge theories, if the running of the gauge coupling is taken into consideration. Our results could verify the presence of such a universal scaling law. Furthermore, we were able to extract the critical exponent $|\Theta_0|$ for various values of the anisotropic velocities. This led us to the finding that the anisotropic velocities provide a parameter that changes the generic scaling scenario of QED₃ from $|\Theta_0|$ smaller than one to a region with large values of the critical exponent $|\Theta_0| \gg 1$.

Concerning future investigations, it is desirable to improve our results by a fully self-consistent treatment of the gauge boson sector.

The results discussed in the section above represent the very first exploratory study of the effects of anisotropy in finite temperature QED₃. To our knowledge, there are no results available from other approaches or from other DSE calculations analyzing a comparable scenario.

4. Quenched QCD under strong external magnetic fields

Quantum chromodynamics (QCD) is widely accepted to be the appropriate description of the strong interaction between the fundamental particles, the quarks. Besides the common features with QED₃ mentioned above (chap. 1), QCD distinguishes itself fundamentally by its non-Abelian nature, including the presence of multiple gauge boson self-interaction vertices, respectively (color)charged gauge bosons. At high energies or small distances, these lead to the anti-screening property of the QCD vacuum, respectively a decrease of the running coupling¹. This asymptotic freedom allows to approach QCD with perturbative methods at large energies in the first place. However, at low energies or large distances where the coupling gets strong, nonperturbative phenomena become crucial ingredients to a full understanding of QCD. Especially the mechanisms of confinement and chiral symmetry breaking in vacuum as well as under nontrivial external conditions are of paramount interest. In the case of finite temperatures and baryonic densities, different states of matter emerge and the transitions between the distinct phases still offer challenges for both, theory and experiment.

Theoretical investigations of the QCD phase diagram are performed in the frameworks of lattice gauge theory, functional methods (such as Dyson–Schwinger equations and the functional renormalization group) and effective model approaches (such as *e.g.* the (Polyakov)-Nambu–Jona-Lasinio model, for a review see [91, 92] and the (Polyakov)-Quark-Meson model, for reviews see *e.g.* [93–95]).

Based on insights from all of these methods, the structure of the QCD phase diagram became more and more diverse over the decades (for a very early version see *e.g.* [96]), especially under extreme conditions (see Fig. 4.A). Extreme conditions hereby mean *e.g.* high temperatures, high baryonic densities/chemical potential, but also strong external magnetic fields. The effects of this third extreme condition are at the center of this work’s investigations.

Historically, Schwinger was the first to address the problem of a relativistic fermion in an external magnetic field [97]. Since then, many debates on the influence and the realization of strong magnetic fields arose, especially in the last two decades. Hereby, first approaches including nonperturbative effects probed the QCD vacuum at zero temperature under the influence of magnetic fields. The investigations were performed in both lattice and effective model calculations and agreed on an increasing chiral condensate with increasing magnetic field. This enhancement of chiral symmetry breaking was coined ‘magnetic catalysis’ [98–104] by earlier studies. (For a pedagogical review see [105].)

¹To be precise, this is true as long as the sign of the beta function stays negative. This is (for three color QCD) the case as long as the number of quark flavors is smaller than 16.

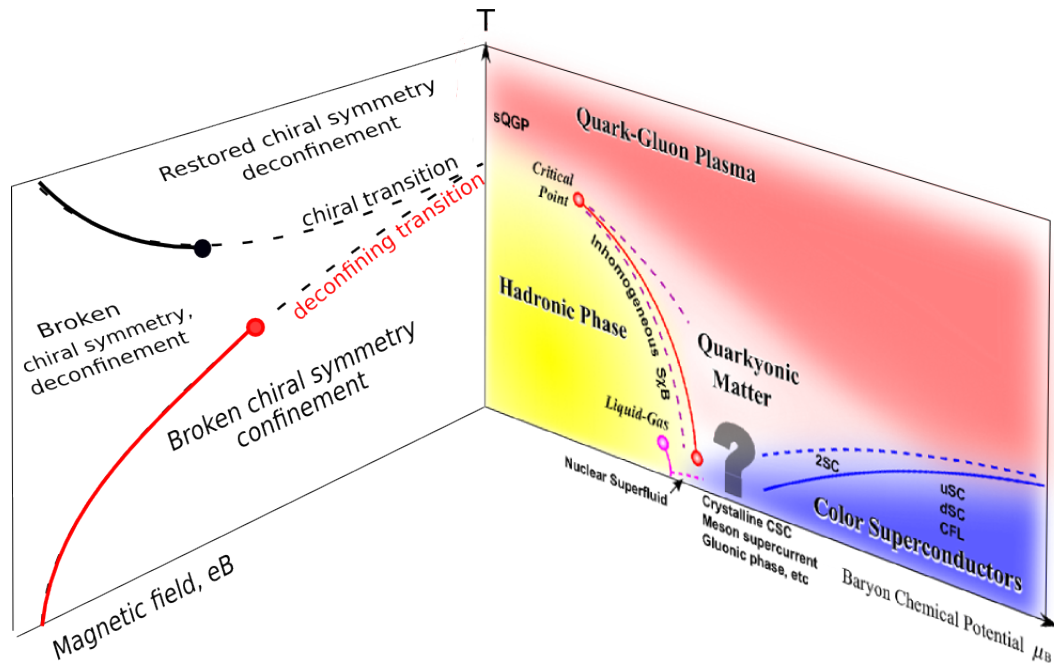


Figure 4.A: A tentative version of the QCD phase diagram, extended with a third axis displaying the magnetic field. The figure is a manipulation of the phase diagrams of Fukushima [89] and Chernodub [90].

In recent years, the extension of the 'standard' $(T-\mu)$ -phase diagram by a third, -the magnetic field- axis led to controversial results². One of these was the possible increase of the chiral phase transition temperature in the $(T-(eB))$ plane. Findings from effective model calculations [90, 101, 103, 104, 108–133] and lattice simulations in quenched approximation [134, 135] and in QC_2D with non-physical pion masses [136, 137] showed opposite behavior to the results of the Budapest-Wuppertal collaboration [138]. The model calculations still extracted the magnetic catalysis. As a consequence, the critical temperature for chiral symmetry breaking increased. Contrary to this, the lattice results of [138] found a suppression of the chiral condensate, so called inverse magnetic catalysis and a decreasing critical temperature. After several attempts [133, 139, 140], this controversy could be explained and understood only very recently [141]: small (physical) quark masses and ordering effects in the Polyakov loop³ were identified to play a crucial *rôle* for the lowest part of the spectrum of the Dirac operator. Depending on the response of these modes at different temperatures, magnetic catalysis or inverse magnetic catalysis is observable in the chiral condensate.

In principle, after the identification of the degrees of freedom that cause the inverse catalysis in full QCD, the way is paved for further investigations at non-vanishing chemical potential in the frame of functional methods or effective models⁴.

Therefore, a first aspect of this work is to investigate the implementation of magnetic fields in a Dyson–Schwinger framework. Furthermore we want to understand underlying mecha-

²General reviews on QCD under extreme conditions can be found in [89, 106, 107].

³More remarks will follow in sec. 4.2, for an exhausting discussion of the subject, refer to [141]

⁴Since they do not suffer from the fermion sign problem.

nisms of magnetic catalysis in light of the established, state of the art approximation schemes [142]. In the longterm future, these first steps should lead to the possibility to contribute to the research on the $(T-\mu-(e\mathcal{B}))$ phase diagram.

Besides the purely academic interest in understanding of the general structure of this three dimensional QCD phase diagram, strong external magnetic fields are realized in at least three physical systems. These are heavy ion collisions [143–145], magnetars [146] and the early universe electroweak phase transition [147, 148]. For instance, in heavy-ion experiments at RHIC, LHC (ALICE) and in future also at FAIR (CBM) nuclei collide with high enough energies to produce a quark-gluon plasma [149, 150]. For non-central collisions, so called spectator quarks produce fields $|e\mathcal{B}|$ of the order of Λ_{QCD}^2 that may influence especially the nonperturbative dynamics. It was proposed that the additional magnetic field may lead to *e.g.* the chiral magnetic effect [143, 151].

This brings us to another aspect of this work. We chose to work in a finite volume DSE setting. One motivation for this setting arises from the strongly interacting system of finite size [152, 153] created in heavy ion collisions. Though this finite interaction volume cannot be trivially matched with a simulated system in a box, due to *e.g.* differing boundary conditions, such finite volume studies can clearly help to understand possible effects on observables. While these effects are expected to alter the phase structure of QCD already without external magnetic fields (compared to the thermodynamic limit), the amount and kind of modification is not clear⁵.

Finally, there is one more aspect of strong external magnetic fields, that is central to the investigations presented in this chapter. Besides their presence in experimental situations and the extension of the 'standard' QCD phase diagram, they have a more technical application in researching confinement. This connection was introduced in form of a dual condensate in [156]. The dual condensate with respect to the magnetic fields, the dressed Wilson loop, is an observable that is sensitive to confinement while at the same time derived from the chiral condensate. It is equal to the conventional Wilson loop in the case of infinitely heavy quarks and thus allows to probe the string tension between two static quarks. The conventional Wilson loop is in the first place defined on the lattice, and not directly accessible from functional methods. In consequence, the dressed Wilson loop could be a very useful observable for functional methods, due to its derivation from the chiral condensate. Nevertheless, there is no work reporting on dressed Wilson loops from other approaches than from lattice gauge theory. Therefore, we strive to investigate the possibility to recover the dressed Wilson loop with the help of external magnetic fields in a Dyson–Schwinger framework.

This chapter is organized as follows: we will firstly reintroduce the Dyson–Schwinger equations for quenched QCD under the influence of external magnetic fields in section 4.1. To this end, we discuss the implementation of the magnetic field in the quark propagator before

⁵Very recently, the relevance of magnetic fields in heavy ion collisions became an even more controversial point of discussion. Estimates in [154] of the equilibration- and lifetime of the magnetic fields suggest that the produced magnetic fields might decay too quickly to be of a relevant size to influence the quark-gluon plasma, which was strictly denied by [155]. However, since there is no definite conclusion on this subject yet.

we write down the DSEs in quenched approximation. Hereafter we review the truncation scheme for the gluonic and vertex input. Having specified the basic setting, we proceed to a discussion of the most important points of our finite volume setting. The last step of this formal section is the introduction of the order parameter for the subsequent sections: The chiral condensate.

Section 4.2 deals with the results on the dual condensate or dressed Wilson loop, probed with help of the external magnetic field. To this end, we summarize the concept of the dressed Wilson loop as introduced in the lattice gauge theory framework and discuss the main features of our finite volume approach compared to the lattice setting. We then present the numerical results of the dual condensate from Dyson–Schwinger equations in varying settings before we give a short summary. Section 4.3 presents first results for the chiral condensate for physical magnetic field strengths at vanishing temperature. We close the chapter with a summary of the advances and outlook on possible next steps concerning the study of physical magnetic field strengths in a DSE approach.

4.1. Formalism

The bare propagator in an external field

We introduce a constant external magnetic field via the principle of minimal substitution, $\partial_\mu \rightarrow D_\mu = \partial_\mu - ieA_\mu$. For convenience, we choose the field pointing in z-direction, namely $A = (0, \mathcal{B}y, 0, 0)^T$, without loss of generality. The minimal substitution procedure introduces an Abelian correction term $F_{\mu\nu}$ to the non-Abelian field strength tensor

$$\mathcal{F}_{\mu\nu,ab,\mathcal{B}} = \mathcal{F}_{\mu\nu,ab} + F_{\mu\nu} \otimes \mathbb{1}_{ab}. \quad (4.1)$$

The Abelian field strength tensor is denoted by $F_{\mu\nu}(x) = \text{const} = \mathcal{B}[\delta_{\mu 3}, \delta_{\nu 1}]$ and it is coupled to the 'trivial' unity matrix in color space, $\mathbb{1}_{ab}$. The modified Lagrangian with suppressed color indices is then denoted by

$$\mathcal{L}_{\mathcal{B}} = \bar{\psi} (i\mathcal{D}_{\mathcal{B}} - m)\psi + \frac{1}{4} \mathcal{F}_{\mu\nu,\mathcal{B}} \mathcal{F}_{\mu\nu,\mathcal{B}}. \quad (4.2)$$

To avoid confusion, let us emphasize that since only constant Abelian terms are considered, there is no dynamical term for the magnetic field in our Lagrangian.

In a scenario without external magnetic field, we could in a next step deduce the DSE for the quark propagator in coordinate space. This would be done along the lines of the standard procedure described in section 2.5. Though, with the magnetic background field included, the transformation of the propagator to momentum space is no longer done in a straightforward plane wave decomposition. The inadequacy of this procedure results from the fact that the propagator now depends on two points in coordinate space, x and x' , and no longer only on their difference. To circumvent this problem and nevertheless recover a diagonal propagator, there exist several equivalent methods. These are specially tailored for the case of constant fields and need to be reconsidered when dropping this constraint. The approaches, namely the Fock–Schwinger eigentime, the Nikishov or the Ritus method were discussed and shown to be connected by Ritus in [157].

In this work, we apply Ritus' method and recover the diagonal quark propagator in a constant magnetic background field along the lines of [157, 158]. This diagonalization finally enables us to perform the Fourier transformation and to obtain the propagator in momentum space as input for our DSEs. We now summarize the most important steps of Ritus' diagonalization procedure. The interested reader is referred to Appendix B.1 for a more detailed overview of the derivation.

Ritus' method is based on two main observations. First of all, the quark propagator can only depend on maximally four independent Lorentz-scalar structures [159]

$$\mathcal{D}, \sigma \cdot F, (F \cdot \mathcal{D})^2, \gamma_5(F \cdot \widetilde{F}), \quad (4.3)$$

or combinations thereof in order to preserve Lorentz- and gauge covariance as well as charge conjugation symmetry. In Eq. (4.3), $\sigma_{\mu\nu} = \frac{i}{2}[\gamma_\mu, \gamma_\nu]$ and $\widetilde{F}_{\mu\nu} = \frac{1}{2}\epsilon_{\mu\nu\alpha\beta}F_{\alpha\beta}$ denotes the dual field strength tensor to $F_{\mu\nu}$ as introduced above. Secondly, the Lorentz-scalar structures in Eq. (4.3) commute with the operator \mathcal{D}^2 . In consequence, we can solve the eigenvalue problem of \mathcal{D}^2 and use its eigenfunctions in order to diagonalize the quark propagator. From

this diagonalization, we find that the bare quark propagator is of the same structure as the bare propagator without external magnetic field.

$$S(\bar{p}) = (i\gamma \cdot \bar{p} - m)^{-1}.$$

However, the propagator now depends on a different subset of momenta \bar{p} that is restricted by the solution of the eigenvalue equation of \mathcal{D}^2 . The momenta \bar{p} are denoted as

$$\bar{p} = (p_0, 0, (p_2)_{n,\sigma}, p_3)^T. \quad (4.4)$$

The momentum restriction is realized in the way that the momenta in the plane perpendicular to the magnetic field now only take distinct, discrete values $(p_2)_{n,\sigma}$. These momentum components encode the Landau level quantization with the index $n \in \mathbb{Z}_0^+$ and are given by

$$(p_2)_{n,\sigma} = \sqrt{|e\mathcal{B}|(2n+1) + \sigma|e\mathcal{B}|}. \quad (4.5)$$

The second index σ in Eq. (4.5) describes the spin projection eigenvalue and can take the values $\sigma = \pm 1$. Considering the actual values of the momenta $(p_2)_{n,\sigma}$, we notice that the momenta for the Landau levels n are spin degenerate, since $(p_2)_{n,1} = (p_2)_{n+1,-1}$ for $n \neq 0$. Only the energetically lowest momentum component $(p_2)_{n=0}$, the lowest Landau level (LLL), is spin polarized as only the eigenvalue $\sigma = -1$ contributes. For further convenience, we rearrange the momentum components p_2 according to their overall magnitude and sum the two indices n, σ in the overall quantum number κ , such that the momentum components now read

$$(p_2)_\kappa = \sqrt{2\kappa|e\mathcal{B}|}, \quad (4.6)$$

with $\kappa = 0, 1, 2, \dots$. In summary, Ritus' diagonalization procedure results in a radial-like discrete momentum in the momentum space plane perpendicular to the associated magnetic field direction. With the diagonal bare propagator with the restricted momenta Eq. (4.6) at hand, we need to reconsider the integration over p_1 and p_2 in the quark DSE. The integral over the previously continuous momenta is now replaced by a sum over all Landau levels and all spin projections, equivalently a sum over the new index κ , to account for all possible momentum states in the p_1 - p_2 plane:

$$\int \frac{dp_1 dp_2}{(2\pi)^2} \dots \longrightarrow \sum_{k_{n,\sigma}} d(n, \sigma) \dots \cong \sum_{\kappa} d(\kappa) \dots \quad (4.7)$$

Upon the change from integration to summation over energy levels, the additional factor $d(\kappa)$ compensates for the degeneracy of the eigenenergies with respect to p_y . We encountered these degeneracies explicitly while solving the eigenequations for \mathcal{D} in App. B.1. The degeneracy factor counts the number of momentum states per unit area and is denoted by

$$d(\kappa) = \frac{|e\mathcal{B}|}{2\pi} \quad \text{for } \kappa = 0, \quad (4.8)$$

$$d(\kappa) = \frac{|e\mathcal{B}|}{\pi} \quad \text{for } \kappa \geq 1. \quad (4.9)$$

The distinction of the degeneracy factors for $\kappa = 0$ and $\kappa > 0$ arises from the previously mentioned spin polarization of the LLL. Since only states with $\sigma = -1$ contribute, the number of states per unit area has to differ from the higher Landau levels, respectively from higher κ s, too.

The dressed propagator

With the bare quark propagator in an external magnetic field along the lines of Ritus' method, we can now write down the dressed propagator. To this end, we need to include -in principle- all four Lorentz-scalar terms (according to in Eq. (4.3)) to account for the most general structure of the propagator and allow for their dynamical generation in the evaluation process. However, the immediate inclusion of all four terms with their dressing functions would result in an immense computational effort (for a more detailed comment see App.B.2). Therefore, we chose to start with the simplest form of the dressed propagator that neglects all non-standard⁶ terms. The dressed propagator is given by

$$S_F(\bar{p})^{-1} = B(\bar{p}) + i(A_0(\bar{p})\gamma^0\omega_p + A_2(\bar{p})\gamma^2(p_2)_\kappa + A_3(\bar{p})\gamma^3 p_3). \quad (4.10)$$

The scalar dressing function is denoted by $B(\bar{p})$, while the functions $A_i(\bar{p})$ with $i = 0, 2, 3$ refer to the vectorial quark dressing functions. We have to include separate vectorial dressing functions for different momentum components, as the magnetic field distinguishes the dynamics in the p_1 - p_2 plane from the p_3 -direction. The introduction of finite temperature further requires additionally considering another dressing function A_0 for the temporal direction. For vanishing temperature, the dressing function in time direction and in the direction of the magnetic field are identical, $A_0(\bar{p}) = A_3(\bar{p})$. Note that we do not need another dressed term for p_1 since our diagonalization procedure in the previous section restricted the momenta such that p_1 vanishes (see Eq. (4.4)).

In any case, our approximation, Eq. (4.10), is certainly valid in the limit of small magnetic fields. For the time being, it therefore represents the starting point for a following systematic elaboration of the influence of higher spin structures in the quark propagator. The effects of these terms and the shortcomings of our approximation in the range of intermediate and large magnetic fields have to be investigated in a future work.

4.1.1. The Dyson–Schwinger equations of QCD with an external magnetic field

In the following, we specify the underlying Dyson–Schwinger equations and the approximations for the results presented in the following chapters.

The derivation of the Dyson–Schwinger equations from the generating functional follows the procedure described in chapter 2.5. Since there are no source terms for the magnetic field, we arrive at the 'standard' QCD DSEs in coordinate space. However, the Fourier transformation to momentum space is more complicated than without an external field due to the Ritus *eigenfunctions*. A summary of the most important steps of this Fourier transformation can be found in App. B.3.

In a very first approach, we postpone a large part of these complications and retreat to solving the 'standard' DSE for the Ritus quark propagator Eq. (4.10). This corresponds to considering a spin-summed propagator in a bare vertex approximation, which includes the omission

⁶The expression 'standard' refers to the spin-structure terms utilized for DSE investigations of QCD or QED₃ without external magnetic field

Figure 4.B: The pictorial representation of the Dyson–Schwinger equation for the quark propagator. The curly lines represent gluon propagators, straight ones fermion propagators. We indicate dressed propagators by adding filled circles to the basic lines. The dressed quark-gluon vertex is encoded by the empty circle.

of an exponential damping factor for the gluon momentum in the directions perpendicular to the magnetic field (see App. B.3). The qualitative effects of this approximation clearly have to be investigated in a future work. The quark propagator DSE is then given by

$$S_F^{-1}(\bar{p}) = Z_2 S^{-1}(\bar{p}) - C_F g^2 \frac{Z_2}{Z_3} \int \frac{dq_0}{2\pi} \sum_{\kappa} d(\kappa) \int \frac{dq_3}{2\pi} \left(\gamma_{\mu} S_F(\bar{q}) \Gamma_{\nu}(\bar{q}, \bar{p}) D_{\mu\nu}(\bar{p} - \bar{q}) \right). \quad (4.11)$$

The equation includes the renormalization constants Z_2 for the quark wave function and \tilde{Z}_3 for the ghost. The ghost renormalization constant in the dressed quark propagator will cancel with another factor \tilde{Z}_3 in the ghost-gluon vertex, respectively in our phenomenological vertex *ansatz* (Eq. (4.12)). Furthermore we will chose $Z_2 = 1$ for convenience. For a first, qualitative study, this choice of the quark renormalization is sufficient⁷. The Casimir $C_F = (N_c^2 - 1)/2N_c$ stems from the trace over the color degrees of freedom that amounts to $C_F = 4/3$ for SU(3) QCD. In Eq. (4.11) we already replaced the integration over the loop momenta q_1 and q_2 with the summation over the Landau index κ as discussed in the previous section. Pictorially, the equations are represented as displayed in Fig. 4.B. Introducing a finite temperature via compactification of the time-direction in the Matsubara formalism (see *e.g.* [15]) leads to a replacement of the integral over q_0 by the sum over the Matsubara frequencies $\omega_q = 2\pi T n_t$,

$$S_F^{-1}(\bar{p}) = Z_2 S^{-1}(\bar{p}) - C_F g^2 \frac{Z_2}{Z_3} T \sum_{n_t} \sum_{\kappa} d(\kappa) \int \frac{dq_3}{2\pi} \left(\gamma_{\mu} S_F(\bar{q}) \Gamma_{\nu}(\bar{q}, \bar{p}) D_{\mu\nu}(\bar{p} - \bar{q}) \right). \quad (4.12)$$

In this work, we will solve the Dyson–Schwinger equations in quenched approximation, *i.e.* we neglect quark loops in the gluon self-energy. This choice is on the one hand motivated by the objective to calculate the dual condensate in chapter 4.2. This observable allows to recover the string tension between a static quark-antiquark pair. It can be recovered from the quenched system only, since the string tension is, in a strict sense, only defined for non-dynamic quarks⁸. On the other hand, the quenched approximation clearly is a necessary starting point for physical magnetic field strength calculations, too. We will explore this setting in section 4.3 in order to estimate the quality of our approximations.

Furthermore, we will use a temperature dependent fit to lattice data as input for $D_{\mu\nu}(k)$. The fit function was firstly obtained by Ref.[42], and served as input for DSE calculations in the

⁷ In future, quantitative investigations of renormalization point dependent observables such as the chiral condensate, a proper fixing of the renormalization point has to be performed in order to obtain comparable absolute values.

⁸ Unquenched QCD is in a strict sense not confining since we expect string breaking at a finite distance.

frame of various investigations, *e.g.* [142, 160]. The dressed gluon propagator is decomposed as

$$D_{\mu\nu}(k) = \frac{Z_T(k)}{k^2} P_{\mu\nu}^T(k) + \frac{Z_L(k)}{k^2} P_{\mu\nu}^L(k), \quad (4.13)$$

with the momentum $k = p - q = (\omega_k, \vec{k})$. The propagator is decomposed into the transversal and longitudinal contribution with respect to the heat bath. These components can be addressed by projection via $P_{\mu\nu}^T(k)$ onto the transversal and $P_{\mu\nu}^L(k)$ onto the longitudinal part. The functions $Z_T(k)$, respectively $Z_L(k)$, denote the according dressing functions. We start from the projector onto the gluon's transverse degrees of freedom (with respect to its momentum k),

$$P_{\mu\nu}(k) = \left(\delta_{\mu\nu} - \frac{k_\mu k_\nu}{k^2} \right), \quad (4.14)$$

with $(\mu, \nu = 0, 1, 2, 3)$. For finite temperature calculations we then can define the transverse and longitudinal projectors with respect to the heat bath as a next step. They are given by

$$\begin{aligned} P_{\mu\nu}^T(k) &= \left(\delta_{ij} - \frac{k_i k_j}{\vec{k}^2} \right) \delta_{i\mu} \delta_{j\nu}, \\ P_{\mu\nu}^L(k) &= P_{\mu\nu}(k) - P_{\mu\nu}^T(k) \end{aligned} \quad (4.15)$$

with indices $(i, j = 1, 2, 3)$. The dressing functions in transversal (T) and longitudinal (L) directions are fitted by the functions

$$Z_{T,L}(k) = \frac{k^2 \Lambda^2}{(k^2 + \Lambda^2)^2} \left\{ \left(\frac{c}{k^2 + \Lambda^2 a_{T,L}(T)} \right)^{b_{T,L}(T)} + \frac{k^2}{\Lambda^2} \left(\frac{\beta_0 \alpha(\mu) \ln[k^2/\Lambda^2 + 1]}{4\pi} \right)^\gamma \right\}. \quad (4.16)$$

The functions $a_{T,L}(T)$ and $b_{T,L}(T)$ are determined and tabled in [42], as are the remaining fit parameters: The scale is given by $\Lambda = 1.4\text{GeV}$ and the coupling constant at the renormalization point by $\alpha(\mu) = 0.3$. The constant c equals 11.5GeV^{-2} . Finally, $\beta_0 = \frac{11N_c - 2N_f}{3} = 11$ and the exponent $\gamma = -\frac{13N_c + 4N_f}{22N_c - 4N_f} = -13/22$, since $N_c = 3$ and due to the quenched approximation the number of flavors is $N_f = 0$. The anomalous dimension of the ghost and gluon propagator, δ and γ , obey the relation $2\delta + \gamma = -1$. This leads to $\delta = -9\frac{N_c}{44N_c - 8N_f} = -9/44$.

In the case of vanishing temperature, the distinction between longitudinal and transversal part of the gluon propagator vanishes. The gluon propagator $D_{\mu\nu}$ only includes the projector on the direction transverse to its momentum Eq. (4.14). The dressing function Eq. (4.16) is now simply denoted by Z and reduces to

$$Z(k) = \frac{k^2 \Lambda^2}{(k^2 + \Lambda^2)^2} \left\{ \left(\frac{c}{k^2 + \Lambda^2 a} \right)^b + \frac{k^2}{\Lambda^2} \left(\frac{\beta_0 \alpha(\mu) \ln[k^2/\Lambda^2 + 1]}{4\pi} \right)^\gamma \right\}. \quad (4.17)$$

Finally, we need to specify the input for the dressed vertex function in Eq. (4.12). The solution of the full set of Dyson–Schwinger equations for the propagators and the vertex is not feasible at the time. For this reason, we use a model for our vertex function including a bare vertex, modified by a phenomenological fit function $\Gamma_\nu(p, q, k)$,

$$\Gamma_\nu(q, k, p) = \tilde{Z}_3 \gamma_\nu \left(\frac{d_1}{d_2 + q^2} + \frac{q^2}{\Lambda^2 + q^2} \left(\frac{\beta_0 \alpha(\mu) \ln[q^2/\Lambda^2 + 1]}{4\pi} \right)^{2\delta} \right), \quad (4.18)$$

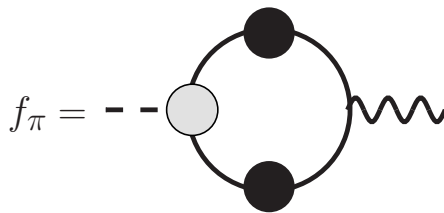


Figure 4.C: The pictorial representation of the Pagels–Stokar formula connecting the pion decay constant with the quark propagator in the chiral limit. The dashed line denotes the pion propagator, the straight lines quark propagators. The wiggly line represents an axial vector current, $\sim \gamma_5 \gamma_\mu$. The dressings of the quark propagators are indicated by black dots, the pion BSA by a gray blob.

It is tailored such that the first summand reproduces $f_\pi = 88\text{MeV}$ in the infrared. To this end, we fix the value of $d_2 = 0.5 \text{ GeV}^2$ and then adjust $d_1 = 7.9 \text{ GeV}^2$ to reproduce f_π^2 for a vanishing magnetic field⁹.

In practice, we follow the the work of [161], that provides a fully nonperturbative derivation of the Pagels–Stokar formula [162], connecting the pion decay constant with the pion Bethe–Salpeter amplitude (BSA) in terms of the quark propagator. This relation holds in the chiral limit and is given by

$$\Gamma_\pi(p, 0) = \gamma_5 \frac{B(p^2)}{f_\pi}, \quad (4.19)$$

where $\Gamma_\pi(k, 0)$ is the pion Bethe–Salpeter amplitude for a vanishing pion momentum and the quark momentum k . One can firstly solve the DSE for the quark propagator and then use the BSA according to Eq. (4.19) as an input for the Pagels–Stokar equation that is diagrammatically given in Fig. 4.C.

The second term dominates in the perturbative limit and reproduces the behavior of the running coupling together with the gluon dressing function. It vanishes for small momenta. As already indicated above, the ghost renormalization constant \tilde{Z}_3 cancels with the \tilde{Z}_3 provided by the prefactor of the integrand in Eq. (4.12). We therefore do not need to fix its value in the turn of the calculations.

With the input for the propagator DSE Eq. (4.12) specified, we obtain the actual equations for the dressing functions $A_0(\bar{p})$, $A_2(\bar{p})$, $A_3(\bar{p})$ and $B(\bar{p})$ after insertion of the propagator Eq. (4.10) and projection on the dressing functions. We will solve the DSEs for the dressing functions on a compact manifold and discuss the features of this setting in the following section.

The Dyson–Schwinger equations in a finite volume

We solve the Dyson–Schwinger equations in the above described approximation scheme (ch. 4.1.1) on a compact manifold. The choice of a finite volume setting for the QCD investigations is motivated by the calculation of the so-called dressed Wilson loop that we will

⁹Private Communication with J. Lücker.

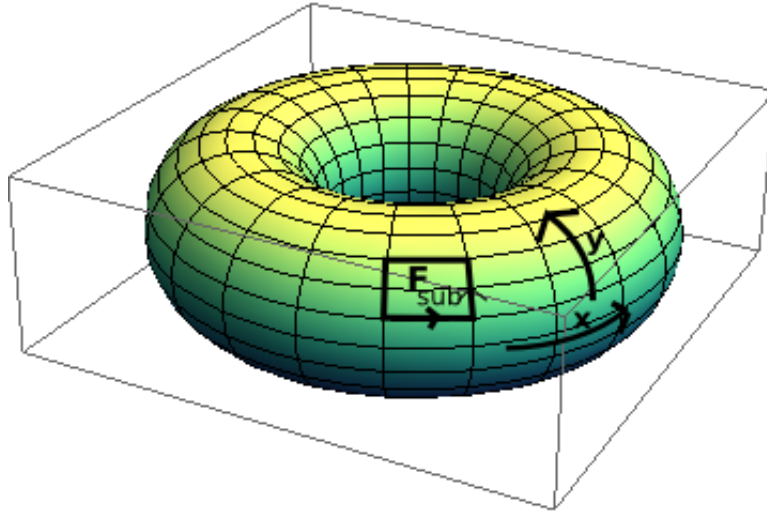


Figure 4.D: Sketch of the compactified x-y plane and the partial area F_{sub} .

discuss in detail in the next section. In a continuum approach, this observable is not accessible.

To this end, we confine the quarks into a four dimensional 'box' in Euclidean coordinate space. We denote the box length by L_μ in the directions $\mu = (0, 1, 2, 3)$. However, in subsequent calculations, we will always choose an equal boxlength in spatial directions, $L_1 = L_2 = L_3 = L$. For vanishing temperature settings in torus calculations, the box lengths in time- and space directions are equal, such that we have only one box parameter denoted by L . For finite temperature calculations, we need to take care of the aspect ratio between the box length in time direction L_0 and in space direction L . In the following, we will only point out the most important aspects of the finite volume setting for the QCD calculations. We compactify the underlying Euclidean spacetime by application of antiperiodic/periodic boundary conditions for quarks/gluons. These guarantee that we respect the KMS-relation for the timelike momentum component. For the spacelike momentum components, we are free to choose periodic boundary conditions for fermions as well as for bosons. This leads to a replacement of the integral over the timelike momentum component q_0 and of the momentum component parallel to the magnetic field by Matsubara(-like) sums, *i.e.*

$$\int \frac{dq_3 dq_0}{(2\pi)^2} (\dots) \longrightarrow \frac{T}{L} \sum_{n_1, n_3} (\dots). \quad (4.20)$$

In the plane perpendicular to the magnetic field direction, in our case the $x - y$ plane, the limited volume leads to a quantization of the magnetic field. This can be understood picturing the magnetic flux through a partial area of our $x - y$ -plane, F_{sub} , and through the complement area, $F_{sub} - L_1 L_2 = F_{sub} - L^2$. For an illustration, see Fig. 4.D.

A charged particle circling F_{sub} must pick up the same phase shift no matter if we consider the magnetic flux through F_{sub} or through its complement, since it describes the same physical

situation. Considering this constraint for the particles' wave functions, we end up with

$$\begin{aligned} \exp(i\mathcal{B}F) &\stackrel{!}{=} \exp(i\mathcal{B}(F - L^2)) \\ \Rightarrow e\mathcal{B} &= \frac{2\pi}{L^2}b, \end{aligned} \tag{4.21}$$

as quantization condition. Consequently, the magnetic field can only take distinct values with the integer field 'quantum' $b = 0, 1, \dots, \infty$. The momenta, previously defined in continuous momentum space by Eq. (4.4), are now counted by

$$\vec{p} = \left(2\pi T(n_0 + 1/2), 0, \sqrt{2\kappa \frac{2\pi}{eL^2} b}, \frac{2\pi}{L} n_3 \right)^T.$$

The magnetic field strength, as well as the Landau levels and the momenta p_0 and p_3 are unbound from above. However, to perform the actual calculations we need to introduce an artificial cutoff for each momentum component in order to make the sums finite and numerically tractable. The particles' wave functions in coordinate spacetime then become coarser, since we encode the information obtained in momentum space in less Fourier modes than necessary. However, the associated coordinate spacetime and the functions defined in coordinate space are and stay continuous¹⁰. This fact distinguishes our setting from a lattice gauge theory setting. The difference becomes crucial for some of the results presented in the following sections.

¹⁰We emphasize this point since one might easily mistake the pure existence of a p_{max} as a sufficient indicator for a discretization of coordinate space.

4.1.2. Chiral condensate

The chiral condensate, $\langle \bar{\psi}\psi \rangle$, is the order parameter associated with chiral symmetry breaking. It measures the affinity of the vacuum to create a quark-antiquark pair and is defined in terms of the generating functional by

$$\langle \bar{\psi}\psi \rangle = -\frac{T}{V} \frac{\partial}{\partial m} \ln Z.$$

It can equivalently be recovered by a Dirac trace over the full quark propagator,

$$\langle \bar{\psi}\psi \rangle = \text{Tr}(S_F(p)) \quad (4.22)$$

Once we know the quarks' dressing functions, and thus the full quark propagator Eq. (4.10), we proceed to determine the chiral condensate with the help of Eq. (4.22). The four dimensional chiral condensate then reads

$$\langle \bar{\psi}\psi \rangle(b) = \frac{4Z_2 N_c}{L^2} \sum_{n_0, n_3, \kappa} \frac{d(\kappa) B(\bar{p})}{B(\bar{p})^2 + \sum_i (A_i(\bar{p}) \bar{p}_i)^2}, \quad (4.23)$$

with the index i running over $\{0, 2, 3\}$. In the following sections, we will additionally calculate the condensate from a quasi two dimensional setting. To this end, we will collapse the temporal and the 3-component of our momenta in Eq. (4.11) by additional Dirac delta functions $\delta(p_0)\delta(p_3)$ in the integrand. We determine the solution to the previously four dimensional equations and subsequently recover the chiral condensate in the plane perpendicular to the magnetic field. This is done by tracing over the remaining momentum components and yields

$$\langle \bar{\psi}\psi \rangle_{2d}(b) = \frac{4Z_2 N_c}{L^2} \sum_{\kappa} \frac{d(\kappa) B(\bar{p})}{B(\bar{p})^2 + (A_{\perp}(\bar{p}) p_{\perp})^2}. \quad (4.24)$$

The condensate in four- and also in two dimensions is divergent with the UV Cutoff Λ . To remove these quadratic (4d), respectively logarithmic (2d) divergences, we define the subtracted chiral condensate, that is recovered from the chiral condensate for a light and a heavy bare quark mass,

$$\langle \bar{\psi}\psi \rangle(b)_{sub} = \langle \bar{\psi}\psi \rangle(b, m_{light}) - \frac{m_{light}}{m_{heavy}} \langle \bar{\psi}\psi \rangle(b, m_{heavy}). \quad (4.25)$$

In general, the cutoff Λ is also depending on the magnetic field b . We compensate this dependence by adjusting the number of included Landau levels for each field strength separately as will be explained in more detail in the following section. The main point is that the momenta obey the condition

$$(p_2)_{\kappa}^2 \leq \Lambda^2 \leftrightarrow \kappa_{max} \leq \frac{b_{max}}{b},$$

that leads to more or less the same cutoff for every b . Small variations are caused by the fact that we can only consider integer numbers of Landau levels (see *e.g.* Eq. (4.30)). However, generally speaking the subtracted chiral condensate as defined in Eq. (4.25) should serve its purpose and cancel the largest part of the UV divergences.

4.2. The dual condensate from external magnetic fields

Understanding the mechanisms of dynamical mass generation and confinement are the central objectives of research related to the QCD phase diagram. While dynamical mass generation is tied to the breaking of chiral symmetry, already the exact definition of confinement is controversial. Respectively, there are several scenarios in discussion how to describe confinement from a fundamental point of view. One of these is motivated by a mutual order parameter, the Polyakov loop. Its expectation value is sensitive to center symmetry breaking and likewise indicates deconfinement [163]. Additionally, Gattringer [164] found that the Polyakov loop can be related to the spectrum of the Dirac operator, if the boundary conditions are generalized. This relation is important since it can be seen in analogy to the Banks–Casher relation [165] that connects the chiral condensate to the infrared eigenvalues of the Dirac operator. Thus, the eigenvalues of the Dirac operator could serve as the connecting degrees of freedom between confinement and chiral symmetry breaking. In the course of research for a better understanding of the contribution of the separate eigenvalues [166–169], yet another observable connected to the Polyakov loop was discovered, the dressed Polyakov loop [170, 171]. This observable can be pictured as a collection of loops winding once around the temporal direction of the spacetime manifold. While the winding number is fixed by projection, in principle all possible detours in spatial directions contribute¹¹. In the limit of infinitely heavy quarks, the dressed Polyakov loop reduces to the conventional, or ‘thin’ Polyakov loop. Due to the connection to the Dirac operator’s eigenvalues, it can be computed by Fourier transforming the chiral condensate with respect to generalized boundary conditions. These boundary conditions are controlled with the angle φ . The expectation value of the dressed Polyakov loop is equally well suited to investigate center symmetry breaking, respectively confinement, as the expectation value of the thin Polyakov loop. However, the (thin) Polyakov loop, identically to the Wilson loop, is an observable primarily defined on the lattice. Since there is no straight forward connection between the Polyakov- or Wilson loop and an n -point function, as there is one for *e.g.* the chiral condensate, there is no direct way to address their expectation values in a functional methods framework. With the connection to the chiral condensate however, the introduction of the dual condensate opened a new way to obtain complementary results from the functional method approach¹².

In analogy to the dressed Polyakov loop, Bruckmann and Endrödi [156] introduced a second dual condensate, the dressed Wilson loop. The dual observable can be seen as a collection of loops in a spatial plane, having the same area but different circumferences. The loops of different areas can be distinguished from each other by their response to an external, constant Abelian magnetic field. In the limit of infinitely heavy quarks, the authors of [156] have shown that the dressed Wilson loop connects to the conventional Wilson loop. The conventional Wilson loop is sensitive to confinement and decays with an area-law in the confining phase. This connection allows to extract the string tension also from the dual observable. For certain, the extraction of the string tension from the dressed Wilson loop is an unnecessary effort for lattice calculations. Nevertheless, the dual condensate might once again turn out to be a valuable observable for functional methods. Since there is no straight forward relation between the Wilson loop and an n -point function, it is not possible to extract the string tension from a Wilson loop, or a Wilson loop-like quantity in *e.g.* a Dyson–

¹¹Although these are weighted according to their length and spatial detours therefore are suppressed.

¹²For more information on the dressed Polyakov loop from a DSE point of view, refer to [172, 173]

Schwinger framework to date. After the successful study of the dressed Polyakov loop with the Dyson–Schwinger method (*e.g.*[160]), the following section presents a feasibility study to extract the string tension from the dressed Wilson loop.

The dressed Wilson loop from the lattice

The dual condensate associated with the dressed Wilson loop is the Fourier transform of the chiral condensate. One of the dual variables is given by the area $S_{(\mu\nu)}$ that is enclosed by a loop in the μ - ν -plane and pierced by the magnetic flux $\phi_{\mathcal{B}}$. The second is the magnetic field strength \mathcal{B} that is linked with the area by the magnetic flux. In a lattice gauge theory framework as well as in our finite volume DSE setting, the magnetic field strength is discretized. The dual condensate is therefore obtained by a discrete Fourier transform of the chiral condensate depending on \mathcal{B} ,

$$\langle \widetilde{\bar{\psi}\psi} \rangle(S) = \frac{1}{S_{(\mu\nu)}} \sum_{b \in \mathbb{Z}} \langle \bar{\psi}\psi \rangle(b) e^{-i\mathcal{B}(b)S}. \quad (4.26)$$

For quenched QCD and in the limit of infinitely heavy quarks, this dual condensate is associated with the conventional Wilson loop. Therefore, we expect the dual condensate to follow an area-law decay in the confined phase that allows to extract the string tension σ_s ,

$$\langle \widetilde{\bar{\psi}\psi} \rangle(s)_{m \rightarrow \infty} \sim \exp(-\sigma_s A_s). \quad (4.27)$$

The enclosed area is denoted by A_s . We would like to comment on the fact that the proportionality factor σ_s describes the spatial string tension, while the common definition of the Wilson loop includes a loop winding around one spatial and one temporal direction. First of all, since we are working in a zero temperature setting, Lorentz-invariance guarantees that we still extract the string tension in its strict sense. However, even if we consider finite temperature, the spatial string tension still is an important quantity. Working with finite explicit quark masses, we still expect to recover the area law from the dressed Wilson loop. However, we have to account for the fact that this string tension can depend on the seed mass, $\sigma_s(m)$. Thus, a seed-mass study is mandatory in order to classify the obtained results.

Let us now proceed with some aspects of the simulation. In the lattice gauge theory framework, coordinate space can be decomposed into smallest area units, the plaquettes. The existence of the plaquette translates into a maximum representable magnetic flux and therefore into a maximum value for the dual variable, the magnetic field strength [137, 174]. The connection can easily be seen from the additional phase caused by the external field and introduced into the link variable via the shift in the vector potential. The plaquette should be equal with and without the external field. This leads to the condition

$$\begin{aligned} \bar{U}^{\mathcal{B}}(x) &= \bar{U}(x) \\ \Leftrightarrow 1 &= e^{i\mathcal{B}xa} e^{-i\mathcal{B}(x+a)a} \\ 2\pi &= \mathcal{B}_{max} a^2, \end{aligned}$$

that defines the maximum magnetic field strength $\mathcal{B}_{max} = 2\pi/a^2$. a denotes the lattice spacing and results from the ratio of the boxlength and the number of spacetime points N_μ/L_μ in a certain direction μ . We rearrange the equation after plugging in the discretized form of \mathcal{B}_{max}

from Eq. (4.21). Thus we obtain $b_{max} = N_{(\mu\nu)}$, with the maximum number of points in the μ - ν -plane denoted by $N_{(\mu\nu)} = N_\mu \cdot N_\nu$. The quantized magnetic field strength Eq. (4.21) is therefore limited to the interval $b \in [0, N_{(\mu\nu)}]$. The restriction of the magnetic field automatically leads to a periodicity of all b -depending observables, especially of the chiral condensate. Furthermore, the dual condensate (Eq. (4.26)) is now obtained from a finite, discrete Fourier transformation of the chiral condensate,

$$\langle \widetilde{\bar{\psi}\psi} \rangle(s) = \frac{1}{S_{(\mu\nu)}} \sum_{b=0}^{b_{max}} e^{-2i\pi bs/N_{\mu\nu}} \langle \bar{\psi}\psi \rangle(b). \quad (4.28)$$

Here, we additionally replaced the previously continuous area S with the quantized area in the μ - ν -plane, $S = s \frac{L^2}{N_{(\mu\nu)}}$. This relation arises naturally due to the lattice spacing a in each direction.

In the DSE framework, several of these definitions need to be adjusted to the basic setting of our manifold in order to use a similar relation to obtain the dressed Wilson loop.

The dressed Wilson loop from DSEs

In the finite volume setting as introduced in section 4.1, we firstly solve the Dyson–Schwinger equations with a finite UV momentum cutoff. This cutoff is chosen such that we fix a maximal momentum in the direction parallel to the magnetic field, $\Lambda_z^2 = (2\pi/LN_z)^2$. The momentum cutoff in the direction perpendicular to the magnetic field is defined to be symmetric, $\Lambda_z^2 \stackrel{!}{=} \Lambda_{xy}^2$. From the definition of the momenta p_2 from Ritus' method and the demand that only the lowest Landau level should be inside the momentum cutoff, a maximum value for the magnetic field strength is fixed:

$$b_{max} = \lfloor \pi N_z^2 \rfloor, \quad (4.29)$$

with $\lfloor \rfloor$ being the Gauss brackets, *i.e.* the floor function. However, this b_{max} is a technical cutoff, introduced not by the formalism itself but by the necessity to make the equations numerically manageable. By definition of our finite volume itself, the momenta p_μ and therefore also the magnetic field b are infinite. Thus, we do not expect observables to be periodic in the magnetic field, as we do within the framework of lattice gauge theory. In addition, this means that the maximum magnetic field in Eq. (4.29) does not imply that we can lay hands on a minimum area. The area in coordinate space still is a continuous quantity $S \in [0, L^2]$, limited only by the box area. In fact, the consequence of our momentum cutoffs is that the functions we want to represent in coordinate space become somewhat unsharp and 'noisy'. This is due to the fact that we use less modes in Fourier space than necessary to preserve full information. With the cutoff prescription at hand, we proceed to solve the DSEs for the dressing functions 4.12 for each magnetic field strength $b \in [0, b_{max}]$. For each value of b , we determine the number of included Landau levels according to

$$\begin{aligned} p_2(\kappa, b)^2 &\leq \Lambda_{xy}^2 \\ \kappa(b) &\leq \left\lfloor \frac{b_{max}}{b} \right\rfloor, \end{aligned} \quad (4.30)$$

with $\lfloor \cdot \rfloor$ again indicating the floor function. With the quark dressing functions and the chiral condensate at hand, we will then determine the dual condensate with the help of

$$\langle \widetilde{\bar{\psi}\psi} \rangle(s) = \frac{1}{L^2} \sum_{b=0}^{b_{max}} e^{-2i\pi b s/L^2} \langle \bar{\psi}\psi \rangle(b), \quad (4.31)$$

where s is now a continuous variable.

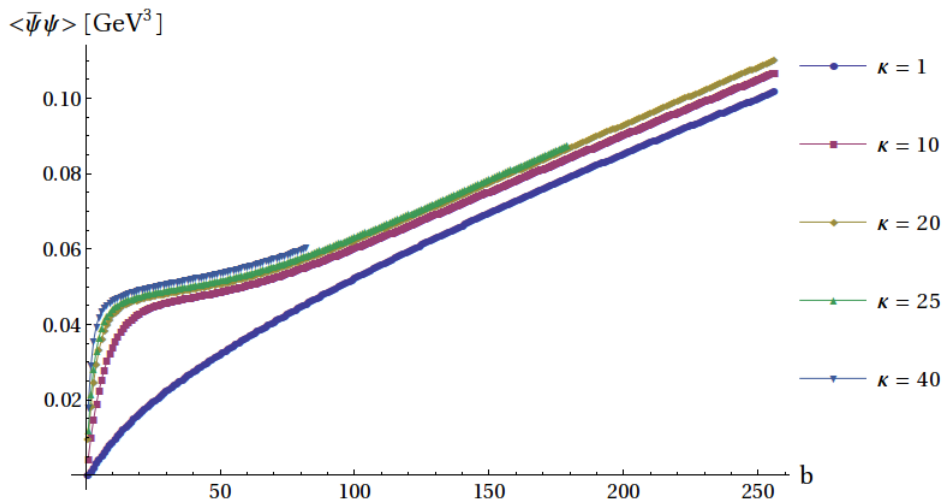


Figure 4.E: The chiral condensate recovered from the four dimensional propagator as a function of the magnetic field strength b and the number of included Landau levels κ . The bare mass is given by $m = 5$ MeV at $\mu = 3.3$ GeV.

4.2.1. Numerical Results

Four dimensional studies: fixed number of Landau levels

We start our investigations by considering a fixed number of Landau levels for all magnetic field strengths. This implies a magnetic field dependent UV cutoff that complicates the comparison of observables. It is nevertheless instructive to study the influence of a subsequently increasing number of Landau levels. For instance, the lowest Landau level is dominant for low energies as long as the quark mass is smaller than the magnetic scale, $m \ll \sqrt{|e\mathcal{B}|}$ and leads to a dimensional reduction of the theory describing the spectrum of low-energy excitations. Beyond this lowest Landau level approximation (LLLA), we are interested in how the chiral and the dual condensate behave for fixed numbers of Landau levels.

To this end we solve the Dyson–Schwinger equations, with the truncations and approximations specified in section 4.1, on a $(N_T = 8) \times (N_z = 33)$ torus. The magnetic field takes values $b \in [1, 16^2] \hat{=} |e\mathcal{B}| \approx 2$ GeV. The underlying box lengths is $(6\text{fm})^4$ and the bare quark mass $m = 5$ MeV at the renormalization point $\mu = 3.3$ GeV. From the quarks’ dressing functions, we calculate the chiral condensate according to Eq. (4.23). Figure 4.E displays the renormalized chiral condensate for a varying maximum number of Landau levels κ as a function of the magnetic field b . Notice that the chiral condensate is trivially zero at $b = 0$ due to the (degeneracy) prefactor proportional to b (see Eq. (4.9)). We find that the lowest Landau level monotonically increases with the magnetic field strengths. Including higher Landau levels leads to a larger absolute value of the chiral condensate on the one hand. On the other hand, the higher Landau levels lead to a non-monotonic behavior of the chiral condensate: after a steep rise for low to intermediate magnetic fields, the condensate saturates and then decreases before it increases again. It is remarkable that the chiral condensate converges for strong magnetic fields with an increasing number of Landau levels, what is in accordance with the expected dominance of the lowest Landau level at large magnetic fields. However,

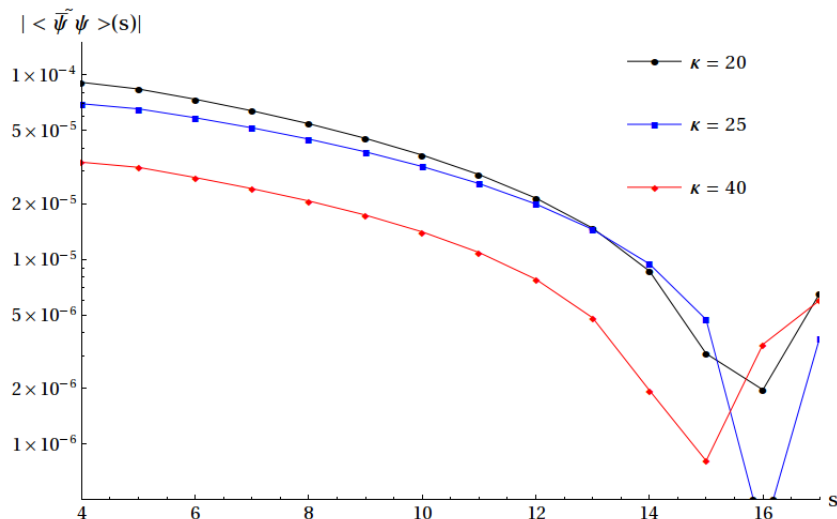


Figure 4.F: The dressed Wilson loop as a function of the enclosed area s and the number of Landau levels κ .

for small and intermediate magnetic fields, the chiral condensate converges only very slowly, if at all, with an increasing number of Landau levels.

From the chiral condensates in Fig. 4.E we compute the dual condensate by performing the Fourier transformation defined in Eq. (4.31) for several chosen numbers of Landau levels. The resulting dual condensates for $\kappa = 20, 25$ and 40 are displayed in Fig. 4.F. All dual condensates show a region at small to intermediate area units where we can identify an area-law decay. This region increases with an increasing number of Landau levels. At the same time, the slope of the decay gets smaller. Due to the finite number of summands in the Fourier

| κ | $\sqrt{\sigma}$ [GeV] |
|----------|-----------------------|
| 1 | 1.02 |
| 10 | 0.47 |
| 20 | 0.35 |
| 25 | 0.31 |
| 40 | 0.31 |

Table 4.1: The string tension $\sqrt{\sigma}$ for a different number of Landau levels κ extracted from the dual condensates displayed in Fig. 4.F.

transformation, the dual condensate crosses zero at some area s . The size, for which this zero crossing happens, is influenced by numerical artifacts. Scanning the dual condensates for a larger range of Landau levels¹³, we find that the more Landau levels and the more magnetic fields b we include and thus the better the quality of the Fourier transformation, the more the zero shifts to larger areas s . The slope of the linear fall-off can be identified with

¹³Not included in Fig. 4.F for reasons of clarity in presentation.

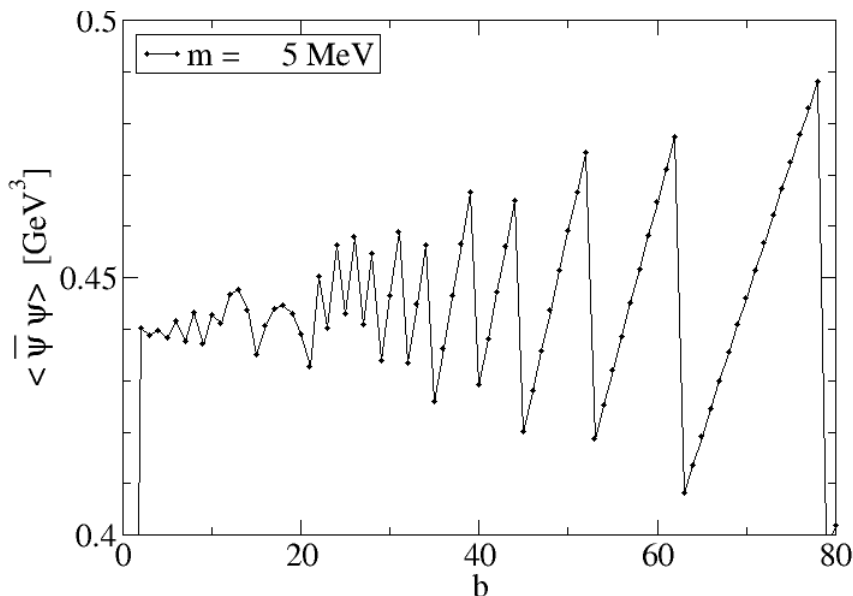


Figure 4.G: The chiral condensate recovered from the four dimensional propagator depending on the magnetic field strength b . It was recovered from a torus with $N_T \times N_X = 20 \times 20$ points, a four volume of $L_0 \times L^3 = (6\text{fm})^4$, a magnetic field strengths $b \leq 314 \hat{=} |e\mathcal{B}| \approx 2.2 \text{ GeV}^2$ and a seed mass of 5 MeV. The plot displays the window up to $0 < |e\mathcal{B}| \lesssim 1 \text{ GeV}^2$.

the string tension of a static quark-antiquark pair, according to Eq. (4.27). The extracted string tensions are listed in table 4.1. We find a decreasing string tension that converges to a value of 0.31 GeV for approximately twenty Landau levels included.

Although this convergence is encouraging, we expect the results for the chiral and in consequence also the dual condensate to be affected by the differing UV cutoffs per magnetic field strength. We therefore improve our numerical setting in the way that we impose a magnetic field independent cutoff. The results of these investigations are discussed in the following sections.

Four dimensional studies: fixed UV cutoff

We begin our investigations with the solution of the four dimensional DSEs for the quark dressing functions derived from Eq. (4.12). To this end, we confine our system into a box of length $L = 30\text{GeV} = 6\text{fm}$ in all four dimensions. In terms of a torus finite volume setting, this effective zero temperature calculation corresponds to an absolute temperature of $T = 33 \text{ MeV}$. We choose the same number of points in temporal as in spatial direction, that is $N_T = N_X = 20$ points. With the truncations and approximations specified in section 4.1, we evaluate the chiral condensate according to Eq. (4.23). The first result for a bare quark mass of $m = 5 \text{ MeV}$ is depicted in Fig. 4.G. The figure displays the (unrenormalized) chiral condensate depending on the magnetic field quantum b . For lower to intermediate field strengths, the chiral condensate shows an oscillatory behavior that changes into a stepwise

linearly increasing condensate with increasing b . This behavior resembles, to our best knowledge, a quantum field analogon to the quantum mechanical De Haas–Van Alphen effect. The De Haas–Van Alphen effect is originally defined for a quantum system in a finite volume under an external magnetic field. It describes the oscillation of the free energy as a function of the external field until a distinct field strength where all particles occupy the lowest energy state. The overall energy of the particles then increases linearly with the increasing magnetic field. The oscillations in the free energy arise due to two competing effects: A particle 'living' on a certain Landau level is pushed to higher energies, since the Landau level energy is proportional to the increasing magnetic field (see Eq. (4.5)). Thus the overall free energy increases. On the other hand, the next lower Landau level can contain more and more particle states, since with an increasing magnetic field also the degeneracy per Landau level increases (see Eq. (4.9)). So from a certain field strength on, it is energetically preferable for the particle to occupy the next lower Landau level. This results in a decrease of the free energy, when the particles change Landau levels from n to $n - 1$. As soon as all the particles are assembled in the lowest Landau level, the free energy increases linearly as there is no lower energy state available.

In the quantum field theoretic setting, we first of all deal with the chiral condensate instead of the free energy. However, the quantum field theoretical analogue of the free energy is the Schwinger functional,

$$F \leftrightarrow 1/\beta \ln(Z),$$

with the inverse temperature β . The relation between chiral condensate and generating functional is given by

$$\langle \bar{\psi}\psi \rangle = -\frac{\partial}{\partial m} \ln(Z).$$

Neither the inverse temperature nor the derivative with respect to the seed mass m changes the dependence of the generating functional on the magnetic field. Therefore, we expect the chiral condensate to depend on b in the same way as the generating functional and to show an analogous behavior to the free energy.

However, the ray pattern at intermediate to high magnetic field strengths displays a peculiar behavior: with every 'step', the next ray starts at lower values for the chiral condensate. This can be understood by going back to the way we set our finite volume and how we imposed the momentum cutoff. In analogy to the quantum mechanical scenario, we see the competing effects of occupation of higher energy states and the degeneracy of lower Landau levels for lower to intermediate external field strengths. Since we assume a fixed momentum cutoff also perpendicular to the magnetic field, the number of Landau levels still inside the plane is adjusted for each b . We therefore reach the field strength b_{full} , where all -in our finite volume- available energy states are filled. The chiral condensate increases linearly until the highest included (and fully occupied) Landau level increases beyond our energy limit. It therefore drops out of the considered contributions for the chiral condensate: We see the first decrease in the chiral condensate. Going to higher external field strengths, the total amount of the chiral condensate increases again linearly, since still all available Landau levels are occupied. The increase proceeds until the next Landau level is energetically pushed beyond our momentum cutoff. In that way the ray pattern emerges until we have only one -the lowest- Landau level inside our volume, what defines our maximum magnetic field b_{max}

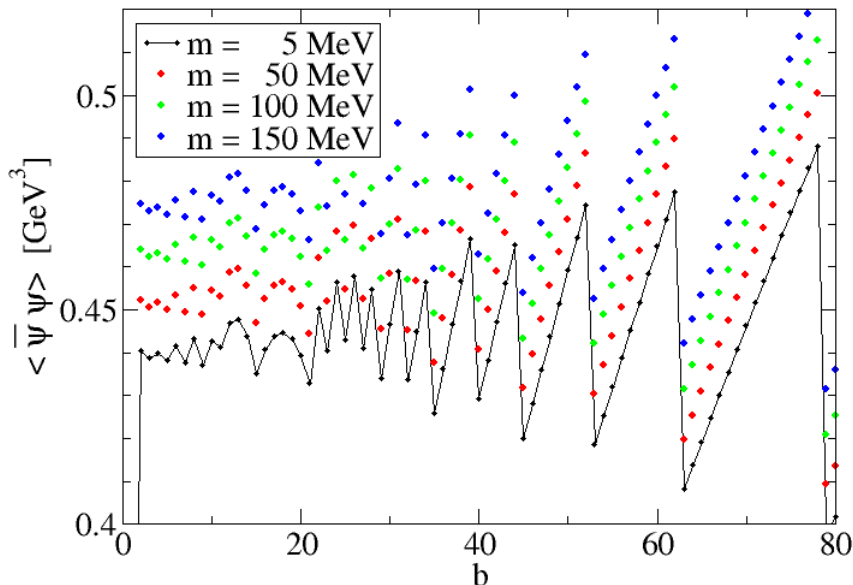


Figure 4.H: The figure shows the chiral condensate at fixed cutoff and volume, but with varying bare quark masses. We only find a quantitative shift, but no obvious qualitative changes in the chiral condensate.

(compare sec. 4.2). Going to larger fields, $b > b_{max}$, already the lowest energy state, respectively the lowest Landau level, lies outside of the considered momentum space volume. It is not available for our quarks and no dynamical mass is generated. In consequence, the chiral condensate vanishes for magnetic fields with $b > b_{max}$ by definition of our four torus.

Figure 4.H furthermore shows the chiral condensate for varying bare quark masses. There are no qualitative changes for different quark masses. We find a simple shift to larger values of the chiral condensate.

Let us now proceed to the discussion of the dual condensate. Considering Fig. 4.G and Figs. 4.H, we anticipate that the calculation of the dual condensate according to Eq. (4.31) will not be straight forward. The reason for this suspicion lies in the behavior of the chiral condensate at b_{max} , which is physically well understandable and expected (discussion see above), but problematic from the mathematical point of view. Let us discuss this point in more detail: we used the hybrid Fourier transformation to change from finite, but continuous coordinate space to an infinite, but discrete momentum space. We had to reduce momentum space to make the sums appearing in our DSEs finite. This we did in the most convenient way by cutting the modes outside of a symmetric cutoff in all four momentum components. This procedure can be pictured as forcing the momentum states into an infinitely high potential well, or mathematically speaking as the convolution of the dressing functions with a step function. In the chiral condensate, this convolution leads to a jump at $b = b_{max}$, that is clearly visible in Figs. 4.H. By calculating the dual condensate to the chiral condensate, we change again to coordinate space. This time however, our setting resembles more that of a discrete than a hybrid Fourier transformation, since we have only a finite number of

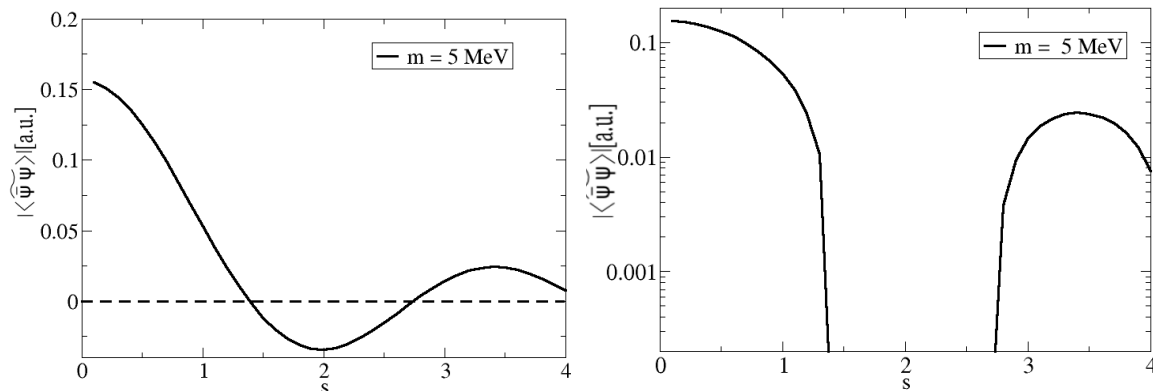


Figure 4.I: The dressed Wilson loop recovered from a four dimensional chiral condensate as a function of the continuous area s . We only show the dressed Wilson loop in the range of small areas. Already these first results show that the loops around the different areas are too noisy to be distinguishable in the current setting.

Fourier modes left. By definition of the momentum space box we additionally introduced the *leakage effect* into our dual condensate¹⁴. We therefore expect the dual condensate to behave like a modified sinc-function, hopefully with still strong enough signatures of the contained physical information.

Figure 4.I shows that our expectations prove to be true. We find indeed a sinc-function with slope, frequency and amount of undershooting depending on the underlying chiral condensate. However, it is now not clear how or if we can extract the string tension from this dual condensate. We therefore wish to include some investigations on the qualitative behavior of this dual condensate under the variation of external parameters. Although we cannot immediately identify a region with a well-defined area-law, we believe it to be interesting if and how much the dual condensate responds to variations. We investigate the behavior of the dual quark condensate with a variation of the bare quark mass, since the dual condensate is supposed to make contact to the conventional Wilson loop for infinitely heavy quarks. Figure 4.J displays the results of our investigations, that is only minimal changes of the dual condensate as a function of the bare quark mass. Still, there is hardly a region where the dual condensate develops an area-law like behavior.

We conclude that although we are working in a finite volume with the above described similarities to the lattice setting, it is not straightforward to extract the same information. One possibility to improve the discrete Fourier transformation of the chiral condensate could be a rethinking of the implementation of our momentum space cutoff. As described above, we use a hard cutoff and assume all (dressing) functions to vanish outside of our momentum space box. In analogy to *e.g.* signal processing theory, utilizing a window function instead of a step function for the dressing function's cutoff might improve the signal strength in our dual condensate. Consequently, an encoded area-law might become more visible.

Besides this possibility, it is, on a more basic level, an open question if the dual condensate with respect to the external magnetic field contains information on the string tension also in a non-lattice setting. This is clearly an issue that needs further attention. However, this subject

¹⁴ The effect describes the modification of the Fourier transformed chiral condensate, compared to the 'original' dual condensate, due to a limited observation time, *i.e.* our limited number of momentum modes.

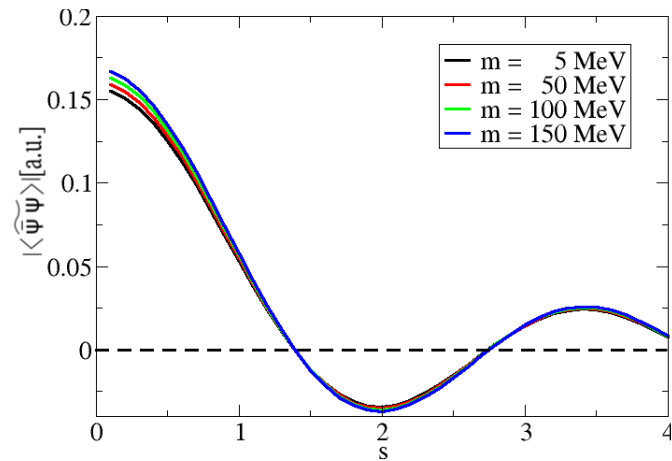


Figure 4.J: The dressed Wilson loop recovered from a four dimensional chiral condensate depending on the continuous area s for different values of the seed mass m . We only show the dressed Wilson loop in the range of small areas.

of research lies beyond the scope of this work and is to be addressed in a future project. In the following, we will stay in the above described setting and investigate the chiral condensate in the two dimensional plane perpendicular to the magnetic field.

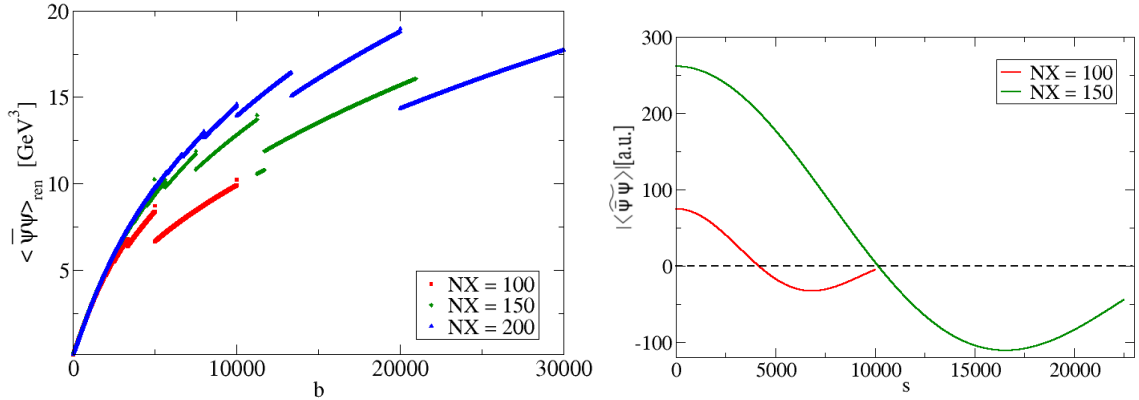


Figure 4.K: The dressed Wilson loop (right panel) recovered from a two dimensional chiral condensate (left panel) in dependence on the continuous area s . We only show the dressed Wilson loop in the range of small areas.

Two dimensional study: Scenario I

In this section we will proceed to discuss a slightly different setting than described previously. In lattice gauge theory, the dual condensate is recovered in the two dimensional plane perpendicular to the magnetic field only. In ref. [156], the authors state that the four dimensional dual condensate is qualitatively the same as in two dimensions in lattice gauge theory calculations. However, it is harder to recover the signal of the dressed Wilson loop, since non-planar loop contributions worsen the signal-to-noise ratio significantly. In that sense we would like to probe the two dimensional plane, as outlined in sec. 4.1.2, in order to compare the results to our four dimensional findings (see above) and to lattice results.

It is important to note that this is an effective reduction of dimensions. We do not switch to a theory defined in two dimensions but carry over features of the four dimensional setting. We wish to emphasize this point, since otherwise, in two dimensions only, the theorem of Mermin, Wagner and Coleman [175, 176] would forbid chiral symmetry breaking right from the start. With $\langle \bar{\psi}\psi \rangle_{2d}$, we then calculate the dual condensate according to Eq. (4.31). We solve the DSEs in the compactified $p_x - p_y$ plane for magnetic fields in the range of $b \in [1, NX^2]$. Note that for the 'dimensionally reduced' problem, we can solve the DSEs for much larger UV cutoffs and volumes than in four dimensions. We can therefore use artificially large strong magnetic fields to probe the chiral, respectively the dual condensate in two dimensions in still reasonable CPU times. With the obtained quark dressing functions for bare masses of $m_{light} = 5 \text{ MeV}$ and $m_{heavy} = 50 \text{ MeV}$, we compute the chiral condensate. From these two condensates we calculate the subtracted chiral condensate according to Eq. (4.25). The results for the subtracted chiral condensate are depicted in the left panel of Fig. 4.K.

The chiral condensate is monotonically increasing in the lower range of the computed magnetic field strengths. We do not observe the De Haas–Van Alphen oscillations at small magnetic field strengths. We assign this to the extremely large UV-cutoff that allows the inclusion of an extremely large number of Landau levels at small b ($\mathcal{O}(\kappa) = 10000$). Increasing the magnetic field strengths, there are supposed to be transitions between different Landau levels at practically all times. Thus on average, we do not expect to be able to resolve the

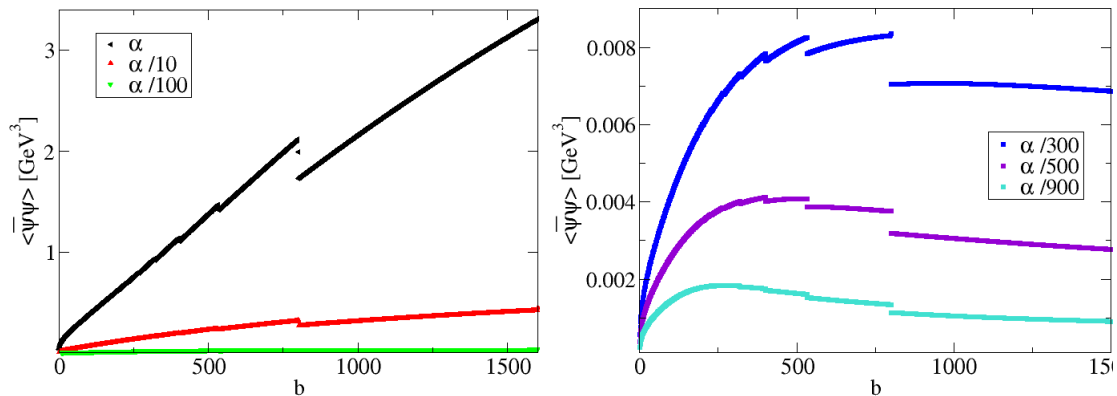


Figure 4.L: The chiral condensate for varying effective couplings g_{eff} obtained from the two dimensional setting.

oscillations on an integer magnetic field 'grid'. However, we still observe a ray-pattern as soon as the number of Landau levels inside our UV cutoff is considerably reduced for very large values of b . Thus, the chiral condensate in two dimensions is still overall an increasing function of the magnetic field and thus qualitatively unchanged compared to the four dimensional condensate. We therefore expect a similar behavior of the dual condensate, too. We compute the (subtracted) dual condensate with the Fourier transformation Eq. (4.31) from the subtracted chiral condensates. The results are displayed in the right panel of Fig. 4.K and confirm our expectations, since we still see a modified sinc-function with no obvious area-law decay as expected for the dressed Wilson loop.

Two dimensional study: Scenario II

It can be questioned if our two dimensional chiral condensate from the quenched DSEs is really equivalent to the definition in the lattice framework. Firstly, there is the discussion if 'quenched' has the identical meaning in the lattice and the DSE framework. Though a detailed study of this question is still pending, agreements in previous investigations [177] suggest that the equivalence of definitions indeed holds. Secondly, it is not clear if our computation of the two dimensional propagator is equivalent to the lattice calculation. Another possibility to recover the two dimensional chiral condensate would be to *e.g.* solve the full set of the four dimensional DSEs and to only compute the chiral condensate in the plane perpendicular to the magnetic field.

In the following, we address one last point that is related to different interpretations of *the* two dimensional chiral condensate in the Dyson–Schwinger framework. That is, we'd like to ask if the coupling between quarks and gluons stays unchanged in the dimensionally reduced truncation/approximation scheme in use. We do not want to argue the general form of the gluonic lattice input. However, when we evaluate our equations in the finite volume, only distinct gluon momenta contribute due to the discrete quark momenta. The number of those is again reduced when we solve the two dimensional system. It might therefore be more

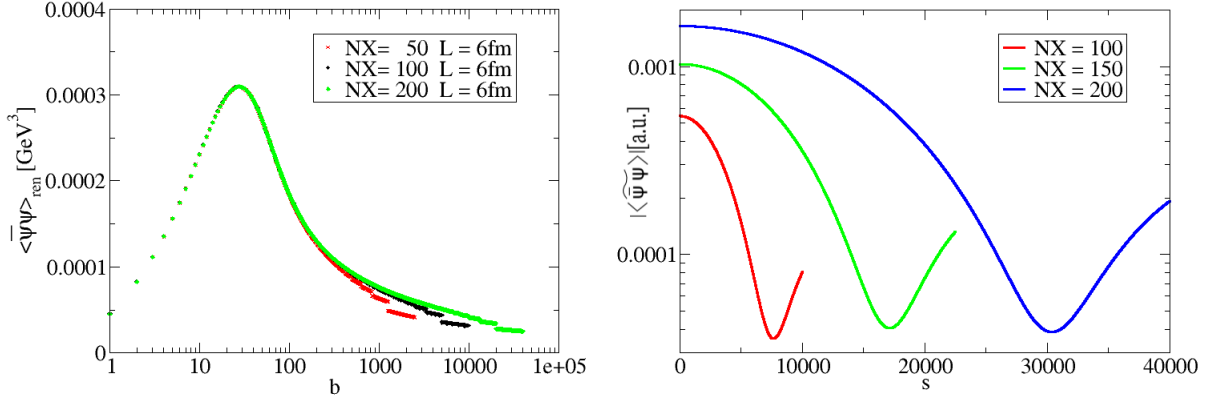


Figure 4.M: The left panel shows the chiral condensate for the smallest coupling g_{eff} in use for different UV-Cutoffs. The right panel displays the dual condensate that is obtained from the two dimensional setting for a small coupling $g_{eff} = \alpha/900$ and different UV-Cutoffs.

appropriate to introduce an effective coupling between quarks and gluons in order to account for discretization and dimensional reduction effects.

In any case, it is interesting to study the influence of such an effective coupling onto the solution of the DSEs and in consequence on the chiral and dual condensate. In order to get a very first idea of the influence of an effective coupling, we evaluate the effectively two dimensional DSEs for different values of g_{eff} . The Dyson–Schwinger equation for the quark propagator in this scenario is given by

$$S_F^{-1}(\bar{p}) = Z_2^{-1}(\bar{p}) - C_F g_{eff}^2 \frac{Z_2}{Z_3} \sum_{\kappa} d(\kappa) \int \frac{dq_3 dq_0}{(2\pi)^2} \left(\gamma_{\mu} S_F(\bar{q}) \Gamma_{\nu}(\bar{q}, \bar{p}) D_{\mu\nu}(\bar{p} - \bar{q}) \delta(q_0) \delta(q_3) \right).$$

We solve the DSEs for the quarks' dressing functions in a 'box' of side length $L = 6\text{ fm}$ and $b \in [1, 40^2]$. Figure 4.M displays the chiral condensate for different values of the effective coupling $g_{eff} \sim \alpha$. We find a decreasing condensate with a decreasing quark-gluon coupling, which, in general, is to be expected. However, we also note that the condensate becomes non-monotonous for very small effective couplings. The left panel of Fig. 4.M shows that this behavior is persistent also for larger UV cutoffs.

We interpret these findings as an artifact of our approximation scheme (see section 4.1). Neglecting in particular the exponential damping factor of the gluon momentum in the $p_x - p_y$ plane (see App. B.3) amplifies the gluon contributions to the fermion self-energy and thus the chiral condensate. We suspect that this additional contribution might prevent the strong increase of the chiral condensate for large magnetic fields. In consequence, this might even help to recover the signal of the dressed Wilson loop in the dual condensate.

Due to the vanishing of the chiral condensate for large magnetic fields (see Fig. 4.M), our continuation (of the dressing functions) by zero to larger momenta is smoother than in the previously discussed cases. We therefore expect the dual condensate to show a stronger signal of the chiral condensate than of the boundary condition.

The right panel of Fig. 4.M confirms that this is indeed true. The dual condensate now

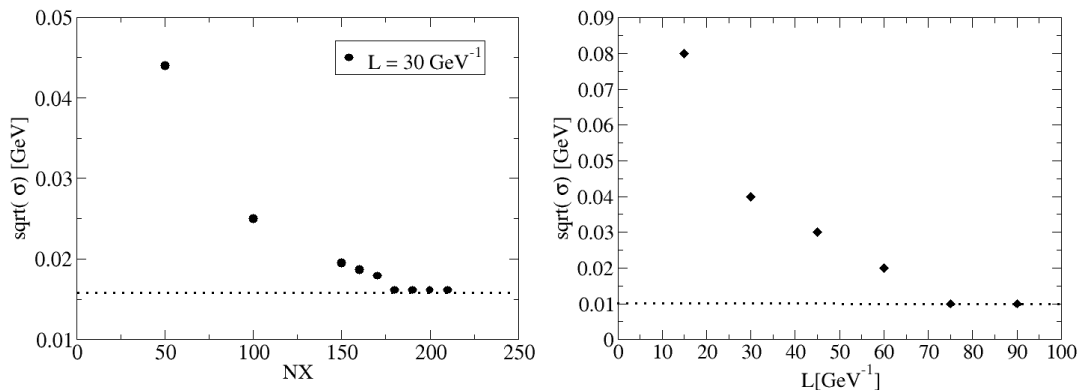


Figure 4.N: The string tension for varying external parameters: cutoff (left panel), volume (right panel). The string tension is extracted from the dual condensate, computed in the plane perpendicular to the magnetic field only, with an effective quark-gluon coupling g_{eff} .

displays an area law decay with an increasing area s , from which we extract the associated string tension. To this end, we further analyze the dependence of the equations with the effective coupling on our setting parameters. The results for the string tension for different UV cutoffs are displayed in the left panel of Fig. 4.N, for different volumes in the right panel. For both, the increasing volume and UV cutoff, we find a converging string tension. This leads us to the conclusion that it is in principle possible to extract a string tension via the dressed Wilson loop in a DSE setting. However, as the various discussions in this chapter have shown, our current approximation scheme needs to be improved in future investigations. Furthermore, more work needs to be invested in order to clarify on the details of the effective coupling, the possibility of a 'better' Fourier transform by different UV cutoffs and finally, on the best way of solving the DSEs for a discrete coordinate space.

4.2.2. Summary

In this chapter, we investigated the accessibility of a recently introduced lattice observable, the dressed Wilson loop, in a finite volume Dyson–Schwinger framework. This work aimed to evaluate if it is possible to extract the string tension from the dual condensate although functional methods in general do not have direct access to the Wilson loop. One could also reformulate this task, namely if the information about the string tension is indeed only encoded in the gauge fields. Or if this information is also extractable from fermionic observables and especially if our finite volume setting is apt to grant us access to this information. To this end, we introduced an external magnetic field along the lines of Ritus’ method and chose a finite volume framework resembling the lattice conditions in [156]. In this very first approach, we chose a rather strong approximation scheme in solving the ‘standard’ DSE for the Ritus propagator with a bare (spin summed) vertex *ansatz*. Our analysis encompassed the computation of the dual condensate from four different scenarios.

In the first approach, we solved the four dimensional DSEs for a fixed number of Landau levels for all magnetic field strengths. While we found a monotonically increasing chiral condensate for the lowest Landau level, the inclusion of more Landau levels led to a non-monotonicity of the chiral condensate for small to intermediate magnetic field strengths. We could recover the dressed Wilson loop and extract the string tension as a function of the number of Landau levels. However, this approach has the caveat that the UV cutoff depends on the magnetic field strengths.

In the second scenario, we therefore imposed a largely magnetic field independent UV cutoff by adjusting the number of included Landau levels with b . This led to De Haas–Van Alphen oscillations in the condensate for small magnetic fields and an increasing behavior for intermediate to large external fields. Due to the increasing chiral condensate for large magnetic fields, we cannot extract a definite value for the string tension in this setting. The reason for this is the hard cutoff at a certain value b_{max} . This cutoff signal dominates the Fourier transform and we cannot identify the clear area law decay that is needed for an extraction of the string tension.

We therefore switched to the third scenario, that is closer to the lattice gauge theory setting of [156] in the way that we compute the two dimensional chiral condensate. To this end we solved the effectively two dimensional DSEs and calculated the planar chiral condensate perpendicular to the magnetic field. As expected from lattice results, the two dimensional results for the chiral condensate are qualitatively the same as for the four dimensions: the overall increasing chiral condensate for an increasing magnetic field. In consequence, there is no possibility to extract the string tension from the dual condensate.

Finally, in the fourth approach, we solved the DSEs for an effective coupling between quarks and gluons in an effectively two dimensional setting. Our results show that there exists an effective coupling strength for which we can minimize the cutoff effects in our dual condensate. For this case, the dual condensate displays an area law decay and we could extract a string tension that converges for large volumes and large cutoffs. This finding furthermore suggests that the approximation/truncation scheme of the DSEs is too strong, since the omitted exponential damping of the gluon momentum would have a similar effect as the effective

coupling.

In summary, the findings of this chapter have shown that the computation of the dressed Wilson loop in a Dyson–Schwinger framework suffers from more technical problems than the dressed Polyakov loop. It turned out to be a delicate task to identify a finite volume setting that allows to extract an area law decay in the dual condensate. The reasons for this are on the one hand technical aspects and on the other hand assigned to our approximation scheme.

Regarding the technical aspects, we firstly miss the periodicity of our observables with respect to the magnetic field b that makes the dual condensate accessible in a lattice framework. Furthermore, our chiral condensate is increasing for large magnetic fields close to the cutoff. This is in principle in agreement with the phenomenon of magnetic catalysis in quenched QCD¹⁵. However, this also means that our dual condensate is spoiled by cutoff effects, and that we do not see a clear area law decay. Our results for an effective coupling and for a fixed number of Landau levels for all b however suggest, that the dual condensate might nevertheless be an accessible quantity in a Dyson–Schwinger framework. However, also regarding technical aspects, more investigations are needed in order to establish a reliable setting that allows to extract the true QCD string tension.

To this end, we propose two different starting points. Firstly, based on the above presented results, we suggest to stay in the basic approximation/truncation scheme, but to modify the cutoff procedure in the magnetic field. It might be sufficient to introduce a damping factor for the dressing functions outside the momentum space volume. Although this is clearly an artificial ingredient, it might permit a minimization of the cutoff effects in the chiral and dual condensate¹⁶. Secondly, one could choose a momentum space configuration such that the coordinate space is discretized, too¹⁷. This would lead to a lattice-like theory that is automatically periodic. However, this second alternative represents a formidable task and an, in principle, independent project.

However, the most important point for future investigations is certainly the improvement of our approximation scheme. The effective coupling study suggest that the additional gluonic damping functions are essential for the recovery of the dual condensate. Including this factor as well as the spin-dependent vertex will be subject of a future investigation.

¹⁵We therefore do not attribute the failure of the string tension extraction to our approximation scheme only

¹⁶Note that the periodicity of the chiral condensate from lattice calculation is also 'artificial' in the sense that it is inherent to the theory, but not a physical feature of the quarks.

¹⁷This procedure would probably be in analogy to condensed matter techniques that allow to change between coordinate and reciprocal space.

4.3. Physical Magnetic Field Strengths

In this chapter, we will present first results for the implementation of magnetic field strength as realized in physical systems. In contrast to the previous chapter, we will limit the field strength itself to 2GeV^2 . This is a common value estimated to be produced in peripheral heavy-ion collisions [144]. We will consider the four dimensional equations and chiral condensates only. Before we discuss our numerical results in section 4.3.2, we need to redefine the cutoff in the plane perpendicular to the magnetic field direction in the following section.

4.3.1. Cutoff Scheme

We start our investigations for vanishing temperature and the truncation scheme as discussed in section 4.1. We wish to impose a symmetric momentum cutoff in all four momentum directions, and firstly fix Λ_z^2 to some value depending on the torus size. Since the range of the external magnetic field strength has an upper limit for physically realized situations, we use this $\mathcal{B}_{max} = 2\text{GeV}^2$ to determine the maximum number of Landau levels κ_{max} in order to obtain Λ_{xy}^2 ,

$$\begin{aligned}\Lambda_z^2 &\stackrel{!}{=} \Lambda_{xy}^2, \\ \kappa_{max} &= \left\lfloor \left(\frac{2\pi n_3}{L} \right)^2 \frac{1}{2|e\mathcal{B}_{max}|} \right\rfloor.\end{aligned}\quad (4.32)$$

In contrast to the previous cutoff scheme for the dual condensate, we still have more than the lowest Landau level inside our momentum space box at maximum magnetic field strengths. The magnetic field strength itself is regulated by the integer b that is limited to $b_{max} = \left\lfloor \frac{|e\mathcal{B}_{max}|L^2}{2\pi} \right\rfloor$. Finally, we obtain the number of included Landau levels per magnetic field b from the relation

$$\begin{aligned}(p_2)_{\kappa_b}^2 &\leq \Lambda_{xy}^2 \\ \kappa_b &\leq \left\lfloor \frac{\kappa_{max} b_{max}}{b} \right\rfloor.\end{aligned}\quad (4.33)$$

With the adjusted cutoff in the plane perpendicular to the magnetic field we can start to solve the Dyson–Schwinger equations for the quarks’ dressing functions.

4.3.2. Numerical Results at zero T

In this section we present the numerical results obtained from solving the equations Eq. (4.11) in the truncation scheme from sec. 4.1 with the above (see sec. 4.3.1) specified cutoff scheme. We solve the DSEs for the dressing functions in a four dimensional volume with a box length of $L_0 = L = 30\text{GeV}^{-1} = 6\text{fm}$ and a momentum space grid of $N_t = N_x = 2 \times N$ points¹⁸. The magnetic field strengths is limited to 2GeV^2 , which means that we are always beyond the lowest Landau level approximation, even for maximum external field strengths. We solve the DSEs under varying external parameters and calculate the (four dimensional) chiral condensate according to Eq. (4.23). Figure 4.O displays the results of our investigations for varying

¹⁸ N will be further specified in Figs. 4.O

bare quark masses (upper panel of Fig. 4.O), varying UV cutoffs (left lower panel) and two test volumes. Remember that we cannot compute the limit $b \rightarrow 0$ in the Ritus formalism as introduced in sec. 4.1. Due to the degeneracy factor in front of the integral, the chiral condensate is trivially zero.

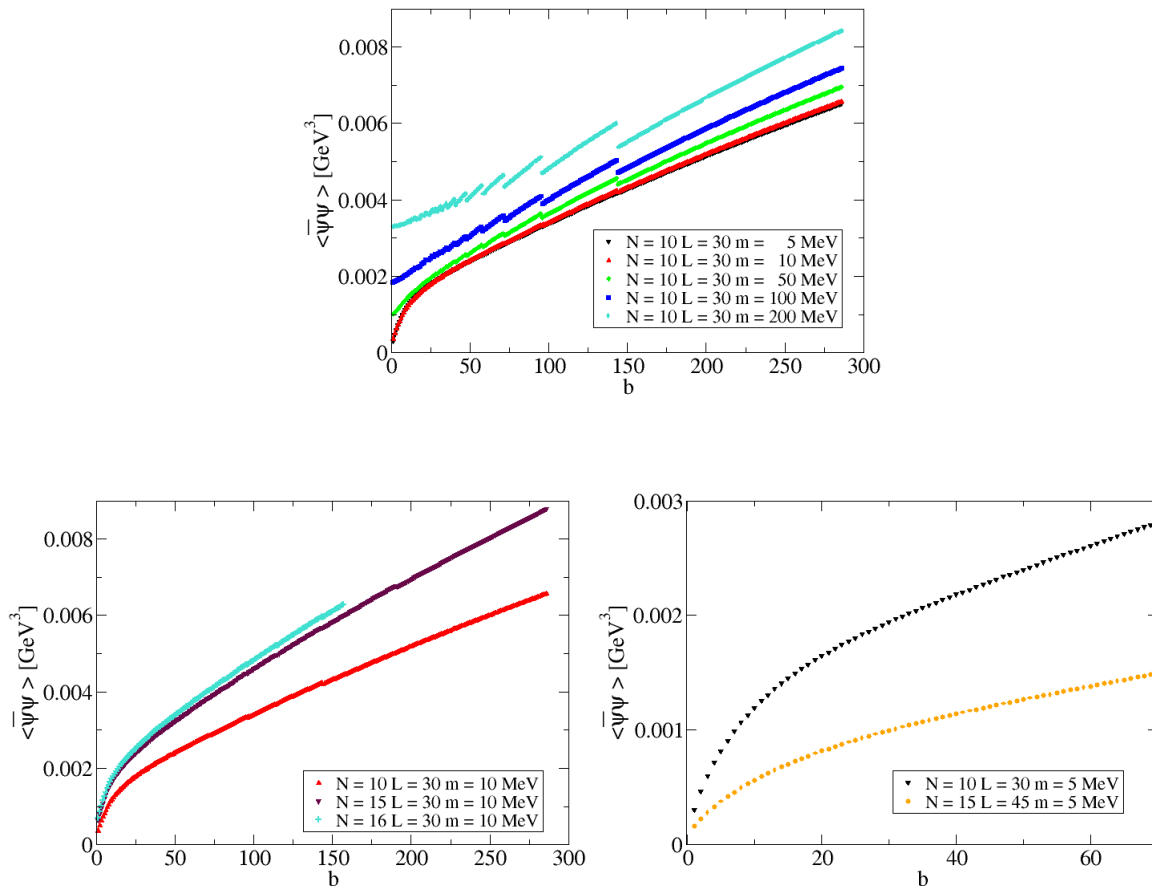


Figure 4.O: The chiral condensate as a function of the magnetic field b at zero temperature. The upper panel displays a study of the seed mass dependence of the chiral condensate. The lower panel shows the chiral condensate for varying UV cutoffs (left) and volume (right).

The chiral condensate for different bare quark masses nicely shows the transition between the smoothly increasing condensate for small masses and the ray pattern for large bare masses. We observed these two behaviors before in the dressed Wilson loop calculations: the chiral condensate was smoothly increasing in the two dimensional setting, where we could impose large UV cutoffs and where the dominant Landau levels were far away from the cutoff. The ray pattern emerged for intermediate and large magnetic fields in two and in four dimensions, as soon as the dominant Landau levels start to be shifted beyond the UV cutoff.

For small masses, the number of Landau levels that lie below our UV cutoff is so large that transitions between the levels happen more or less at every b , washing out the oscillations. Since the UV cutoff is for small masses large enough that the dominant (lower) Landau levels are still inside our momentum space volume, there is no ray pattern observable. An

increasing bare quark mass however naturally increases the chiral condensate. The quark momenta, especially the Landau levels are shifted to higher energies and thus the dominant (lower) Landau levels are earlier, that is at lower magnetic field strengths, sensitive to the UV cutoff and therefore the ray pattern is observable.

The left hand side of the lower panel shows the chiral condensate for varying UV cutoffs. As we would expect from our previous findings, there are no qualitative changes in the behavior of the chiral condensate. However, the value of the chiral condensate increases for an increasing cutoff. Note, that the UV cutoffs employed in these calculations are rather small in comparison to the large cutoffs employed for the two dimensional calculations. The reason for this is the large demand of computational resources: our cutoff prescription allows a comparably large number of Landau levels up to intermediate magnetic field strengths. Together with the four dimensional setting, that is three quark dressing functions, this represents a considerable amount of necessary CPU time.

A similar reasoning applies to the chiral condensate for different volumes. We therefore chose only two representative volumes. The resulting chiral condensates are displayed on the right hand side of the lower panel of Fig. 4.O. For a larger volume but at fixed UV cutoff, we find a slightly smaller chiral condensate.

4.3.3. Summary

In this chapter, we investigated the four dimensional chiral condensate under the influence of physical magnetic field strengths. In comparison to chapter 4.2, this results in a modified cutoff prescription in the plane perpendicular to the magnetic field.

We analyzed the condensate as a function of bare quark masses, the UV cutoff and the size of the volume. For all variations, we found an overall increasing chiral condensate with an increasing magnetic field strength. This finding is in accordance with the phenomenon of magnetic catalysis, that was also found in other approaches.

However, we are aware that the presented investigations were performed in a very strong approximation scheme. This approximation scheme needs to be improved before it is reasonable to proceed with investigations at finite temperature or even for the unquenched equations. Nevertheless, we consider the results of this chapter to be a very first step towards a Dyson–Schwinger study of the effects of physical magnetic fields on QCD.

5. Conclusions and Outlook

In the work at hand, we employed a finite volume Dyson–Schwinger framework to investigate primarily the chiral phase transition in both, QED_3 and QCD. Both of these studies were carried out in an anisotropic environment.

We considered QED_3 in an incarnation that was derived to serve as a low-energy effective theory for high-temperature superconductors. In this form, QED_3 also includes the experimentally found anisotropy of the high-temperature superconducting materials. With this starting point, we investigated the effects of the anisotropic spacetime on the critical number of fermion flavors for chiral symmetry breaking. This transition is associated with the breakdown of the so-called pseudo-gap phase of high temperature superconductors and the transition to the antiferromagnetic (non-superconducting) phase. Our analysis at vanishing temperature was the first study including an arbitrary amount of anisotropy and to go beyond the large- N_f approximation in a functional methods framework. To this end, we employed an *ansatz* for the gauge-boson vacuum polarization that accounts for the anomalous dimension of the fermion vector dressing function in isotropic spacetime. Although our results are affected by finite volume artifacts, they give a qualitative picture of the phase diagram for the critical number of fermion flavors in the full anisotropic plane. Our phase diagram agreed (on a qualitative level) with results from photon-exchange and lattice calculations, at the points where these approaches provided results.

Furthermore, we included finite temperatures in our considerations of QED_3 in an anisotropic spacetime. Besides the extension of the QED_3 phase diagram by a thermal axis, this scenario offers the possibility to study the critical scaling behavior close to the pseudo-conformal window of QED_3 . That is, close to the merger of the thermal phase transition line with the quantum critical point, two generic scaling behaviors can emerge, dominated either by exponential scaling or power-law contributions. From our finite temperature phase diagram, we found that the spacetime anisotropy provides a parameter to tune the generic scaling behavior of QED_3 . While the power-law contributions are dominant for small anisotropies, we found a dominant exponential scaling with only small power-law corrections around the isotropic point.

Another aspect of this work was to investigate the anisotropic environment created in QCD by introducing external magnetic fields, *i.e.* to study the effects of the magnetic fields onto the chiral phase transition. With this information, our investigations aimed at a feasibility study of the calculation of the dressed Wilson loop from Dyson–Schwinger equations. The dressed Wilson loop is a dual variable to the chiral condensate and was originally introduced in a lattice framework. This observable is of great interest, since it potentially offers functional methods access to a direct calculation of the string tension. However, our studies found considerable technical problems due to the quantized, but still continuous magnetic field in

the DSE framework. Although we found certain finite volume settings where we observed an area-law decay of the dressed Wilson loop and extracted a string tension, these settings were highly sensitive to the choice of parameters. We could assign this sensitivity on the one hand to an unfortunate choice of boundary conditions for our finite volume and on the other hand to the shortcomings of our very strong approximation scheme.

Finally, we employed our finite volume DSE setting with external magnetic fields to evaluate the chiral condensate at physical magnetic field strengths. In the context of these investigations, we found magnetic catalysis, what is in accordance with lattice and effective model calculations. These findings represent first steps towards a satisfying analysis of the effects of magnetic fields on the QCD vacuum due to the already mentioned strong approximation scheme that we employed throughout a part of this work.

Outlook

Already in the course of this work, many new questions and ideas for new projects arose. In the following, we strive to address the most important ones.

In zero temperature QED_3 , it is desirable to improve our truncation/approximation scheme beyond our gauge boson vacuum-polarization *ansatz* to a fully self-consistent treatment of the gauge boson sector. Furthermore, a detailed study of more sophisticated vertex *ansätze* and of finite volume effects is necessary to obtain also quantitatively reliable predictions for the phase diagram of the critical number of fermion flavors as a function of the anisotropic velocities.

The finite temperature QED_3 setting furthermore lends itself for a continuum study in the case of equal anisotropic velocities. Since we can exploit the cylindrical symmetry, the computational demand of a continuum study should be manageable, if not reduced in comparison to our finite volume torus setting. If we could access the anisotropic plane, or certain regions of it, in a continuum calculation it should furthermore be possible to resolve the exponential scaling region in the close vicinity of the quantum critical point.

In the course of our studies of QCD with external magnetic fields, one recurring question concerned the definition of 'quenched' in a lattice gauge theory and a Dyson–Schwinger setting. On the one hand, results from *e.g.* dressed Polyakov loop calculations [178] suggest that both definitions are equal. However, there is no systematic study to prove the equivalence of both realizations of a 'quenched' system. To exclude all possibility of doubt, it would be desirable to have such a systematic study.

Another aspect that arises in the context of the comparison with the dressed Wilson loop from lattice gauge theory calculations, concerns a Dyson–Schwinger setting for a discrete coordinate spacetime. Put in a different way, one could also ask for what happens if one applies the Dyson–Schwinger machinery to a lattice gauge theory.

Finally, a crucial next step¹ for any Dyson–Schwinger calculation including magnetic fields, is the inclusion of the fully-fledged Ritus *eigenfunctions*, including the gluon damping- and vertex spin functions. Furthermore, it may be necessary to include higher spin structures in the dressed propagator. With these improvements, one could extend the Dyson–Schwinger setting to finite temperatures and even begin to unquench the DSEs. As we already mentioned at the very beginning of the QCD chapters, unquenching the equations would be crucial to contribute to the ongoing debate over (inverse) magnetic catalysis at finite temperatures.

¹currently work in progress

Acknowledgements

I am indebted to my supervisor C. S. Fischer for countless fruitful discussions, his support and encouragement through the years of my PhD project. Furthermore, I am grateful to a number of persons for many helpful discussions, advice and collaboration while working on this thesis. I acknowledge the support of Richard Williams, Jan Lücker, Jürgen Berges, Jan M. Pawlowski, Falk Bruckmann, Gergely Endrödi, Bernd-Jochen Schaefer, Lorenz von Smekal, Jens Braun and Tobias Goecke.

Financial Support

I acknowledge the support by the *Studienstiftung des deutschen Volkes* for providing financial and conceptual support throughout my PhD time.

I furthermore acknowledge financial support for conferences and research stays, as well as the professional support by the Helmholtz graduate school HIRe.

A. Aspects of QED₃

A.1. Derivation of the QED₃ Lagrangian

In this appendix we follow the derivation of the QED₃ Lagrangian presented under different aspects in [53–55, 57, 179].

The starting point is a BCS-like Hamiltonian in Nambu form,

$$H = \sum_{\vec{k}} \Psi_{\vec{k}}^\dagger \mathcal{H} \Psi_{\vec{k}}, \quad (\text{A.1})$$

where the index \vec{k} denotes the quasiparticles' momentum. The Nambu spinors $\Psi_{\vec{k}}$ contain the creation operators for particles ($c_{-\vec{k}\downarrow}^\dagger$) and holes ($c_{\vec{k}\uparrow}$). They are denoted as

$$\Psi_{\vec{k}} = \begin{pmatrix} c_{\vec{k}\uparrow} \\ c_{-\vec{k}\downarrow}^\dagger \end{pmatrix}, \quad (\text{A.2})$$

where the arrows \uparrow, \downarrow additionally indicate the spin of the electron, respectively the hole. The Hamilton matrix \mathcal{H} in Eq. (A.1) can be decomposed into particle-particle (pp) and particle-hole (ph) interactions [56]. Under the assumption, that the energy-gap function is dominated by pp-interactions, one neglects the ph-interactions as 'residual' $\mathcal{H}_{ph} \simeq \mathcal{H}_{res}$, thus leading to

$$\mathcal{H} = \mathcal{H}_{pp} + \mathcal{H}_{ph} = \begin{pmatrix} \epsilon_{\vec{k}} & \Delta_{\vec{k}} \\ \Delta_{\vec{k}}^* & -\epsilon_{\vec{k}}^* \end{pmatrix} + \mathcal{H}_{res}, \quad (\text{A.3})$$

with the “*” indicating complex conjugation. The contribution of interest, \mathcal{H}_{pp} , contains kinetic and pairing energy and can be further rewritten to [63],

$$H_{BCS-like} = \sum_{\vec{k}\sigma} \epsilon_{\vec{k}} c_{\vec{k}\sigma}^\dagger c_{\vec{k}\sigma} + \sum_{\vec{k}} \Delta_{\vec{k}} c_{\vec{k}\uparrow}^\dagger c_{-\vec{k}\downarrow}^\dagger + \sum_{\vec{k}} \Delta_{\vec{k}}^* c_{\vec{k}\uparrow} c_{-\vec{k}\downarrow}. \quad (\text{A.4})$$

Here, we sum over σ , denoting all possible spin directions of particles/holes in the first term. The kinetic energy $\epsilon_{\vec{k}}$ of a quasi-particle is expressed in reference to the chemical potential μ and given by

$$\epsilon_{\vec{k}} = \frac{\vec{k}^2}{2m} - \mu, \quad (\text{A.5})$$

where m is the quasiparticles' mass and \vec{k} its momentum.

The pairing energy contribution is represented by the energy-gap function $\Delta_{\vec{k}}$. It is characterized by an amplitude Δ and a phase field $\varphi_{\vec{k}}$

$$\Delta_{\vec{k}} = |\Delta| \exp(i\varphi_{\vec{k}}). \quad (\text{A.6})$$

The amplitude $\Delta_o := |\Delta|$ is assumed to be constant over the considered sample, which is a valid assumption for regions in the phase diagram with $T \ll T^*$ and $H \ll H_{c2}$ (London limit).

Before we proceed in the derivation, the d-wave symmetry of the energy-gap function needs to be considered. The symmetry implies that the gap function has zeroes. Experiments show that these 'nodes' lie on the Fermi surface of the electrons and holes that are the building blocks of the quasiparticles [64]. Since we will concentrate on low-energy excitations, these quasiparticles close to the nodes of the energy-gap function are the relevant degrees of freedom for our investigations. We therefore switch into a more suitable coordinate system located at these nodes (as indicated in Fig. A.A). For low energy excitations, we expand the particles' energy contributions in terms of their momenta denoted as q_1 and q_2 ,

$$\epsilon_{\vec{k}} = v_F q_1 + \mathcal{O}(q^2), \quad (\text{A.7})$$

$$\Delta_{\vec{k}} = (v_\Delta q_2 + \mathcal{O}(q^2)) \exp(i\varphi_{\vec{k}}). \quad (\text{A.8})$$

The first order expansion coefficients are denoted by v_F and v_Δ . They describe the velocity of the quasiparticles orthogonal and parallel to the Fermi surface and introduce the anisotropy on a formal level. The linearized Hamiltonian matrix \mathcal{H}_{lin} now takes the form

$$\mathcal{H}_{lin} = \begin{pmatrix} v_F q_1 & v_\Delta q_2 \exp(i\varphi_{\vec{k}}) \\ v_\Delta q_2 \exp(-i\varphi_{\vec{k}}) & -v_F q_1 \end{pmatrix}. \quad (\text{A.9})$$

The standard approach to describe a quasi-particle spectrum in a spatially inhomogeneous system [58] is to solve the eigenvalue problem of the linearized Hamiltonian, also known as the Bogoliubov-de Gennes (BdG) equation,

$$\mathcal{H}_{lin} \Psi = \mathcal{E} \Psi. \quad (\text{A.10})$$

However, with the present form of the Hamiltonian, this is still a formidable task. Since we restricted ourselves to the pseudogap phase with $H \ll H_{c2}$ and $T < T^*$, vortices (magnetic flux tubes) pierce the material in a hexagonal lattice structure [55, 56]. While the vortices are bound in the superconducting phase, they start to fluctuate and interact with the quasiparticles. In particular, the phase field of the energy-gap function picks up a 2π shift when winding around such a vortex. This leads to a non single valued gap function. Ways to avoid this are for example to diagonalize the linearized Hamiltonian with the constraint that the wave function remains single-valued. This is quite a formidable task as branch cuts would have to be introduced, which complicate the calculations significantly [54]. To circumvent this problem, Franz and Tešanović proposed a single-valued phase transformation (FT transformation)[53].

The idea of this transformation is to map the original Hamiltonian onto a Hamiltonian without phase field contributions in the off-diagonal parts via the singular phase transformation. This phase transformation acts differently on the singular and on the regular parts of the phase field of the gap function [53].

Singular FT transformation

We will follow the main steps of the FT transformation in the next lines. Firstly, the phase field $\varphi_{\vec{k}}$ is decomposed into groups of singular (s) and of regular (r) phase contributions,

$$\varphi_{\vec{k}} = \varphi_r + \varphi_s. \quad (\text{A.11})$$

Both of these groups contain vortices. Therefore a second, different grouping redistributes the vortices into the two groups A and B ,

$$\begin{aligned}\varphi_A &= \frac{\varphi_r}{2} + \varphi_{s,A}, \\ \varphi_B &= \frac{\varphi_r}{2} + \varphi_{s,B}.\end{aligned}\tag{A.12}$$

These phase fields contain both a regular contribution and an integer number of vortices. Notice that we have only grouped the phase contributions differently; their renaming and ordering is only for further convenience in calculations. From the two groups of phase fields A and B , one can build a local gauge transformation $\mathcal{U}_{\vec{k}}$ that acts differently on the particle and hole wave functions contained in the Nambu spinor,

$$\mathcal{U}_{\vec{k}} = \begin{pmatrix} \exp(i\varphi_A) & 0 \\ 0 & \exp(-i\varphi_B) \end{pmatrix},\tag{A.13}$$

Carrying out the transformation,

$$\Psi'_{\vec{k}} = \mathcal{U}_{\vec{k}} \Psi_{\vec{k}}\tag{A.14}$$

and Fourier transforming the Hamiltonian \mathcal{H}_{lin} , we obtain the Hamiltonian \mathcal{H}' , which is then given in coordinate space by

$$\mathcal{H}' = \mathcal{U}^{-1} \mathcal{H}_{lin} \mathcal{U} = \begin{pmatrix} i\hbar v_F [i(\partial_1 \varphi_A) + \partial_1] & -i\hbar v_\Delta [i(\partial_2 \varphi_A) + \partial_2] \\ -i\hbar v_F [-i(\partial_2 \varphi_B) + \partial_2] & -i\hbar v_F [-i(\partial_1 \varphi_B) + \partial_1] \end{pmatrix}.\tag{A.15}$$

The phase field contributions define two new fields a_μ and v_μ that represent the gauge fields of the theory,

$$a_\mu = \frac{1}{2} \partial_\mu (\varphi_A - \varphi_B),\tag{A.16}$$

$$v_\mu = \frac{1}{2} \partial_\mu (\varphi_A + \varphi_B).\tag{A.17}$$

While eq. (A.17) still contains singular and regular parts of the phase field φ , eq. (A.16) is built only of singular contributions of φ . Introducing these gauge fields into eq. (A.15), the Hamiltonian \mathcal{H}' changes to

$$\mathcal{H}' = \begin{pmatrix} i\hbar v_F [\partial_1 + ia_1] & -i\hbar v_\Delta [\partial_2 + ia_2] \\ -i\hbar v_\Delta [\partial_2 + ia_2] & -i\hbar v_F [\partial_1 + ia_1] \end{pmatrix} + v_\mu\text{-terms}.\tag{A.18}$$

The contributions of the gauge field v_μ are not specified in eq. (A.18), as these terms will lead to a source term representing charged current interactions. The quasi-particle fields do not carry charge, which legitimizes the focus on the a_μ -field contributions.

Recombination into spinorial representation

As a next step, we combine the four nodes of the energy-gap function on the Fermi surface into four spinors. The reason for this is that we can easily rotate opposite lying nodes into each other and only need to consider the dynamics at two different nodes [63].

$$\Psi_1(\vec{x}) = \begin{pmatrix} \Psi_1(\vec{x}) \\ \Psi_{\bar{1}}(\vec{x}) \end{pmatrix},\tag{A.19}$$

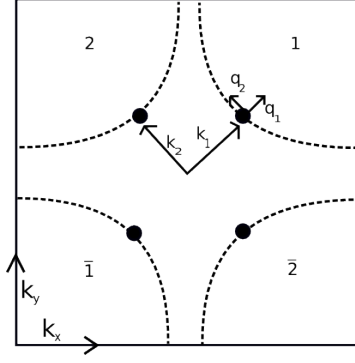


Figure A.A: The Fermi surface is indicated by dashed lines. The dots represent the nodes of the gap function [63].

This simplifies the notation considerably, if we now recast the Hamiltonian into the new form,

$$\mathcal{H}'' = \begin{pmatrix} \mathcal{H}' & 0 \\ 0 & -\mathcal{H}' \end{pmatrix}. \quad (\text{A.20})$$

Further rewriting of the Hamiltonian with the help of Dirac γ -matrices in natural units brings us closer to the effective QED₃ Lagrangian as can be seen from

$$H'' = \int d^2x \bar{\Psi}(\vec{x}) \mathcal{H}'' \Psi(\vec{x}) = \int d^2x \bar{\Psi}(\vec{x}) \{ \gamma_1 v_F (\partial_1 + ia_1) + \gamma_2 v_\Delta (\partial_2 + ia_2) \} \Psi(\vec{x}). \quad (\text{A.21})$$

The Dirac γ -matrices obey the Clifford algebra $\{ \gamma_\mu, \gamma_\nu \} = 2\delta_{\mu\nu}$, which were further specified in chapter 2.

The final step is to include possible time dependencies that we neglected so far. A way to do this is to switch to the path integral formalism [14] by introduction of the generating functional \mathcal{Z} ,

$$\mathcal{Z} = \int \mathcal{D}\Psi^\dagger \mathcal{D}\Psi \exp(-\mathcal{S}), \quad (\text{A.22})$$

wherein the action \mathcal{S} is defined by

$$\mathcal{S} = \int_0^\beta d\tau \int d^2x \Psi^\dagger(\vec{x}, \tau) (\partial'_0 + \mathcal{H}) \Psi(\vec{x}, \tau), \quad (\text{A.23})$$

with $\beta = \frac{1}{T}$, the inverse temperature. In momentum space, the creation operators contained in the Nambu spinors (Eq. (A.2)) obtain an energy dependence ($c_{\vec{k}} \rightarrow c_{\vec{k}}(\omega_n)$).

The frequencies ω_n , known as the Matsubara frequencies, naturally result from the finite time interval on which we evaluate the path integral. They contain the boundary conditions for fermions and bosons and are given by

$$\omega_n = \begin{cases} \frac{2\pi}{\beta} \left(n + \frac{1}{2} \right) & \text{for fermions} \\ \frac{2\pi}{\beta} n & \text{for bosons,} \end{cases} \quad (\text{A.24})$$

where n denotes an integer number $n \in \mathbb{Z}_0$. The time derivative ∂'_0 is the transformed time derivative

$$\partial'_0 = \mathcal{U}^{-1} \partial_0 \mathcal{U} = (\partial_0 + ia_0) + v_\mu\text{-terms}. \quad (\text{A.25})$$

The v_μ -terms are again omitted. To cast the action (A.23) into its final and most elegant form, eqs. (A.21), (A.23) and (A.25) are combined. This yields:

$$\mathcal{S} = \int d\tau \int d^2x \left\{ \bar{\Psi}_1(\vec{x}, \tau) (\gamma_0 (\partial_0 + ia_0) + \gamma_1 v_F (\partial_1 + ia_1) + \gamma_2 v_\Delta (\partial_2 + ia_2)) \Psi_1(\vec{x}, \tau) \right. \\ \left. + \bar{\Psi}_2(\vec{x}, \tau) (\gamma_0 (\partial_0 + ia_0) + \gamma_1 v_\Delta (\partial_1 + ia_1) + \gamma_2 v_F (\partial_2 + ia_2)) \Psi_2(\vec{x}, \tau) \right\}, \quad (\text{A.26})$$

which contains the desired QED₃ Lagrangian¹.

It is important to recognize the influence of the two different speeds of the quasiparticles (v_F, v_Δ) close to the Fermi surface in the action given above. They display an inherent anisotropy of the theory, if $v_F \neq v_\Delta$ is valid. Experiments showed [81] that for HTSs (e.g. YBCO) the so called anisotropy $\alpha = \frac{v_F}{v_\Delta}$ is about 14. This evidence clearly prohibits the neglect of anisotropy motivates its investigation.

¹For more detailed information on the intermediate steps see *e.g.* [180].

A.2. Renormalization Point Dependencies in QED₃

The renormalization factors of QED₃ appear as additional factors in the DSEs. In particular, only the fermion wave function renormalization Z_2 remains in the final version of the equations. In this section, we state the main results of the analysis of the renormalization point dependence of the solutions for the fermionic dressing functions obtained in [181].

To probe the qualitative dependence of the fermion dressing function on the choice of the renormalization point, we solve the DSEs for several values of Z_2 . The results are displayed in Figs.A.B and A.C.

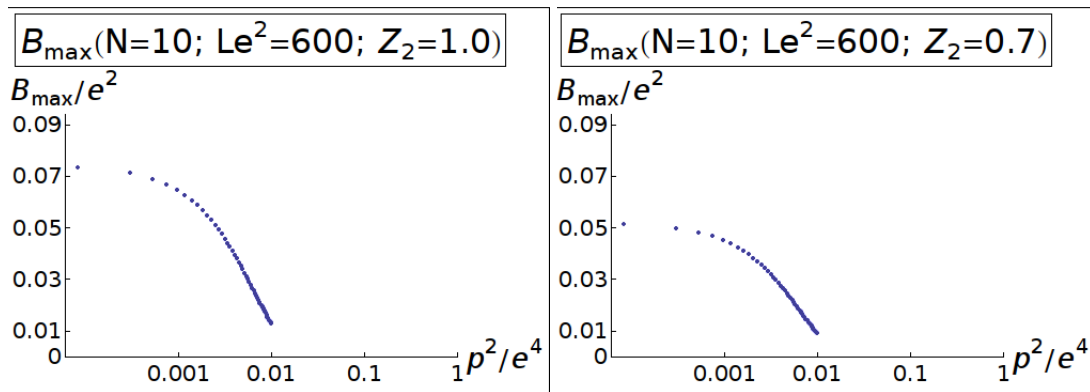


Figure A.B: The scalar fermion dressing function for $Z_2 = 1$ and $Z_2 = 0.7$, evaluated on a momentum lattice of $(2 \times 10 - 1)^3$ points and a lattice spacing of $Le^2 = 600$.

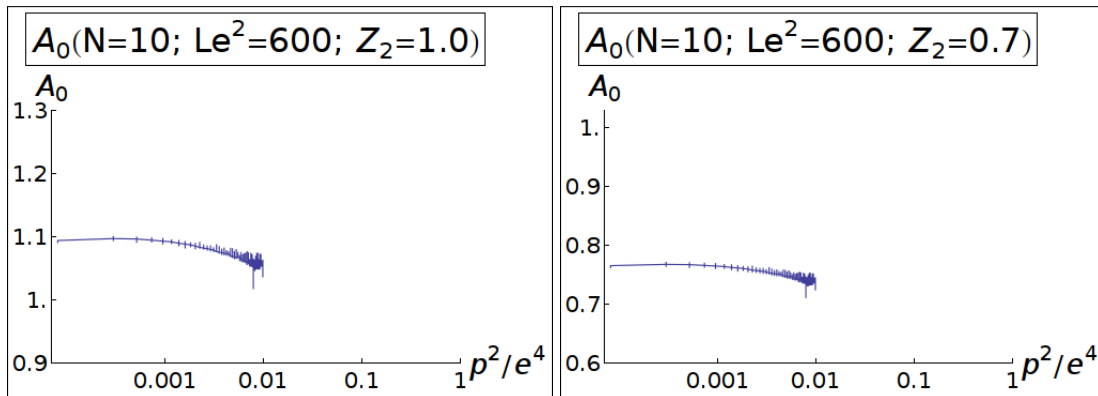


Figure A.C: The time component of the fermionic vector dressing function for $Z_2 = 1$ (lhs) and $Z_2 = 0.7$ (rhs), evaluated on a momentum lattice of $(2 \times 10 - 1)^3$ points and a lattice spacing of $Le^2 = 600$.

Qualitatively, there is no change in the dressing functions observed. We find a simple rescaling of the dressing functions. To exclude all doubts, we additionally calculate the RG-invariant mass function defined by

$$M_i(p) = \frac{B(p)}{A_i(p)}. \quad (\text{A.27})$$

The results for the time component of the M -function for different Z_2 values is shown in Fig. A.D and displays no renormalization point dependence. We therefore conclude that our choice of $Z_2 = 1$ represents a valid option and apply this choice to all following calculations.

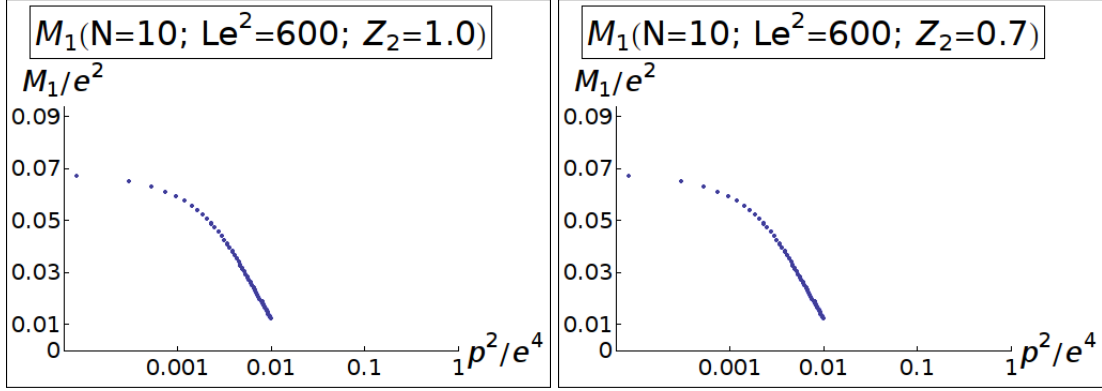


Figure A.D: The renormalization group invariant time component of the M -function. The plot on the left hand side shows the result for $Z_2 = 1$, while the right hand side displays the result for $Z_2 = 0.7$.

A.3. QED₃ :Anisotropic N_f^c in the Pisarski approximation

In the following, we provide the details of the derivation of the scalar fermion dressing function in Pisarski's approximation for anisotropic spacetime. In the case of $v_f = v_\Delta$, we insert the large- N_f vacuum polarization, Eq. (3.10), into the scalar fermion dressing function. The scalar dressing function is implicitly given in Eq. (3.3). The equal anisotropic velocities lead to an inherent cylindrical symmetry. Thus we switch to problem suited cylindrical coordinates. Given the abbreviations

$$\begin{aligned}
 \mathcal{A} &= 2v_f^6 z^4 (\sqrt{r^2 + z^2} \alpha^2 + 16z^2 (4\sqrt{r^2 + z^2} + \alpha)) + \\
 &\quad 8r^6 (8\sqrt{r^2 + z^2} + \alpha + v_f^2 (8\sqrt{r^2 + z^2} + 3\alpha)) \\
 \mathcal{B} &= r^2 v_f^2 z^2 ((1 + v_f^2) \sqrt{r^2 + z^2} \alpha^2 + 8z^2 (8\sqrt{r^2 + z^2} + 24v_f^2 \sqrt{r^2 + z^2} \\
 &\quad + 16v_f^4 \sqrt{r^2 + z^2} + (2 + 5(v_f^2 + v_f^4))\alpha)) \\
 \mathcal{C} &= 2r^4 (v_f^2 \sqrt{r^2 + z^2} \alpha^2 + 4z^2 (8\sqrt{r^2 + z^2} + \alpha + v_f^2 (16\sqrt{r^2 + z^2} + \\
 &\quad 24v_f^2 \sqrt{r^2 + z^2} + (5 + 5v_f^2 + v_f^4)\alpha)) \\
 \mathcal{D} &= N_f (r^2 + z^2) (r^2 + v_f^2 z^2)^2 (8\sqrt{r^2 + z^2} + \alpha) \\
 \mathcal{E} &= 64r^4 + r^2 (64(1 + v_f^2)z^2 + 8\sqrt{r^2 + z^2} \alpha + v_f^2 \alpha (8\sqrt{r^2 + z^2} + \alpha)) + \\
 &\quad v_f^2 z^2 (64z^2 + \alpha (16\sqrt{r^2 + z^2} + \alpha))
 \end{aligned}$$

we arrive at

$$B(\vec{p}) = \frac{1}{(2\pi)^3} \int_0^{2\pi} \int_0^\infty \int_0^\infty d\varphi dr dz \frac{16 B(\vec{p}) r \alpha (\mathcal{A} + \mathcal{B} + \mathcal{C})}{\mathcal{D}\mathcal{E}}. \quad (\text{A.28})$$

Pisarski's approximation [71] now implies that we assume the the scalar fermion dressing function $B(\vec{p})$ equal to a constant $B(\vec{p}) = m$ for all momenta in the range $\alpha \gg p \gg m$. All other momentum contributions are neglected in the integration. Since $r < \alpha$ and $q < \alpha$, we only keep terms with the largest power of α in the numerator and denominator of the integrand. The resulting equation is of a more compact form and reads

$$m = \frac{1}{(2\pi)^3} \int_0^{2\pi} d\varphi \int_m^\alpha dr \int_m^\alpha dz \frac{16mr(2r^4 + r^2(1 + v_f^2)^2 z^2 + 2v_f^4 z^4)}{N_f(r^2 + z^2)^{\frac{3}{2}}(r^2 + v_f^2 z^2)^2}. \quad (\text{A.29})$$

At this point, we perform the integration in z -direction and again neglect the terms not proportional to α . This leads us to

$$m = \frac{1}{(2\pi)^3} \int_0^{2\pi} d\varphi \int_m^\alpha dr \frac{8m \left(\sqrt{v_f^2 - 1} \alpha + (2 + \alpha) \arctan[\sqrt{v_f^2 - 1}] \right)}{N_f r \alpha \sqrt{v_f^2 - 1}}. \quad (\text{A.30})$$

As a next step, the perform the integration over r and φ , using the fact that α is the largest scale in the problem for a last time. We finally arrive at

$$m = \frac{2m \left(\sqrt{1 + v_f^2} + (2 + v_f^2) \arctan(\sqrt{1 + v_f^2}) \right)}{\pi^2 N_f \sqrt{1 + v_f^2}} \ln \left(\frac{\alpha}{m} \right), \quad (\text{A.31})$$

that can be rearranged into the form given in the main text, Eq. (3.26):

$$m = B(0) = c \alpha \exp \left[\left(-\pi^2 N_f \sqrt{v_f^2 - 1} \right) / \left(2 \sqrt{v_f^2 - 1} + 2(2 + v_f^2) \arctan(\sqrt{v_f^2 - 1}) \right) \right].$$

B. Aspects of QCD

B.1. Ritus' method for the quark propagator

Ritus' method is used to diagonalize the quark propagator in momentum space. In this appendix, we follow the steps of [157]. For a more pedagogical presentation and discussion in the light of QED applications of Ritus' method, the interested reader might also refer to [182, 183].

The quark propagator in the external magnetic field has to satisfy the Green's function identity,

$$(\not{D}_\mu - m)S(x, x') \stackrel{\dagger}{=} \delta(x - x'). \quad (\text{B.1})$$

Here, the external field couples to the charged fermion via the covariant derivative, $D_\mu = \partial_{\mu} - ieA_\mu$. The bare mass is denoted by m . Due to the external field term that does not commute with the momentum, we cannot use the standard method to extract the propagator from B.1.

The propagator has to be Lorentz- and gauge invariant, as well as invariant under charge conjugation. In consequence, only four Lorentz-scalars remain as a basis for S ,

$$S(x, x') \sim \not{D}, \sigma \cdot F, (\widetilde{F} \cdot D)^2.$$

All of these commute with the operator \not{D}^2 and therefore have simultaneous eigenbasis. Its eigenfunctions can be used to diagonalize $S(x, x')$ in momentum space. Thus, we reformulated the problem of solving the Green's function identity into solving the eigenvalue problem,

$$\not{D}^2 \mathbb{E}_p(x) = \mathbb{E}_p(x) \gamma p^2, \quad (\text{B.2})$$

For a constant magnetic field in z direction, this can be rearranged to

$$\left[D^2 + e\mathcal{B}\sigma_3 \right] \mathbb{E}_p = p^2 \mathbb{E}_p, \quad (\text{B.3})$$

where σ_3 denotes the diagonal Pauli matrix with eigenvalues $\sigma = \pm 1$. Since the eigenproblems decouple, we can solve the eigenvalue equations for the separate components,

$$D_0^2 \mathbb{E}_p = p_0^2 \mathbb{E}_p \quad D_3^2 \mathbb{E}_p = p_3^2 \mathbb{E}_p \quad (\text{B.4})$$

$$(D_1^2 + D_2^2) \mathbb{E}_p = (p^2 - p_0^2 - p_3^2) \mathbb{E}_p = k_{12}^2 \mathbb{E}_p. \quad (\text{B.5})$$

Here, we denoted the eigenvalue of the coupled equations in 1-2direction by k_{12}^2 . We proceed with a separation ansatz for the eigenfunction $\mathbb{E}_p(x) = E_{p,\sigma}(x) \omega_\sigma$. The function ω_σ is a bispinor containing the eigenvectors of σ_3 and can be written as $\text{diag}(\delta_{\sigma,1}, \delta_{\sigma,-1}, \delta_{\sigma,1}, \delta_{\sigma,-1})$. Furthermore, the $E_{p,\sigma}$ separates into the plane waves as solution for the 0 and 3-component and the eigenfunction for the 1, 2 components,

$$E_{p,\sigma}(x) = N \exp(-i(p_0 x_0 - p_3 x_3)) F_{p_1, p_2, \sigma}(x),$$

with the normalization constant N . Altogether, B.5 is nothing more than the Pauli equation without an electric field, that is basically a shifted harmonic oscillator equation,

$$\left[\partial_1 - (-\partial_2 + e\mathcal{B}x_1)^2 + \sigma e\mathcal{B} \right] F_{p_1, p_2, \sigma}(x) = k_{12}^2 F_{p_1, p_2, \sigma}(x). \quad (\text{B.6})$$

The eigenvalues are given by $k_{12} = \sqrt{e\mathcal{B}(2n+1+\sigma)}$. The quantum number n counts the quantum mechanically known Landau levels. All Landau levels, except for the lowest, are twice spin degenerate due to the contributions of the eigenvalues of the spin matrix, $\sigma = \pm 1$. Another degeneracy of the eigenenergies arises from the free momentum in 2 direction, $\partial_2 \mathbb{E}_{p, \sigma}(x) = p_2 \mathbb{E}_{p, \sigma}(x)$. From B.6, it is obvious that p_2 only shifts the center of the oscillations. The eigenenergy of the harmonic oscillator is independent of p_2 . The additional factor introduced in 4.9 accounts for these degeneracies, whenever we integrate over all possible momentum states. The eigenfunctions of the shifted harmonic oscillator are given by parabolic cylinder functions,

$$F_{k_{12}, \sigma}(x) = N(n) D_n \left(\sqrt{2e\mathcal{B}} \left(x_1 - \frac{p_2}{e\mathcal{B}} \right) \right), \quad (\text{B.7})$$

that form an orthogonal and complete basis. The normalization constant is given as $N(n) = (4\pi e\mathcal{B})^{1/4} / \sqrt{n!}$. Finally, we can return to the original eigenvalue problem of \mathcal{D} that is now solved by

$$\mathcal{D} \mathbb{E}_{p, \sigma} = \mathbb{E}_{p, \sigma} \bar{p}, \quad (\text{B.8})$$

where we introduced the momentum vector $\bar{p} = (p_0, 0, (p_2)_{n, \sigma}, p_3)$. For convenience, we renamed the momentum component $k_{12} \rightarrow (p_2)_{n, \sigma}$. This subset of momenta satisfies $\bar{p}^2 = p_0^2 + (p_2)_{n, \sigma}^2 + p_3^2 = p^2$, as it is easy to convince oneself. This brings us back to the Green's function identity that is now straight forward to solve,

$$\begin{aligned} (\mathcal{D}_\mu - m)_0(x, x') &= \int dp (\mathcal{D}_\mu - m) \mathbb{E}_p^\dagger{}_0(\bar{p}) \mathbb{E}_p \\ &= \int dp \mathbb{E}_p^\dagger (\bar{p}_\mu - m)_0(\bar{p}) \mathbb{E}_p \\ &= \int dp \mathbb{E}_p^\dagger \mathbb{E}_p \\ &= \delta(x - x'). \end{aligned} \quad (\text{B.9})$$

The last step holds due to the orthogonality property of the Ritus eigenfunctions. We find that the diagonal bare propagator in momentum space takes its 'standard' form, but now depends on the special subset of momenta,

$${}_0(p) \rightarrow_0(\bar{p}) = \frac{1}{\bar{p} - m}.$$

The eigenfunction matrix that diagonalizes the bare propagator is given by

$$\mathbb{E}_p(x) = \sum_\sigma E_{p, \sigma}(x) \omega(\sigma) \quad (\text{B.10})$$

B.2. The dressed quark propagator

Ritus originally stated in his papers that there are four possible, non-trivial Lorentz-scalar structures that the propagator can depend on. Including all of them with an according dressing function would be a formidable task. However, investigations of Leung and Wang, [184], have shown that terms proportional to $\sigma^{\mu\nu} F_{\mu\nu}$ lead to a fermionic mass that depends on the direction of the magnetic field. This structure is therefore also forbidden in the quark propagator.

In principle, the propagator can still depend on Lorentz-scalar structures of the form

$$(F \cdot D)^2 \text{ and } \gamma_5(F \cdot \tilde{F}). \quad (\text{B.11})$$

in addition to the 'standard' Lorentz-scalars $\not{D}, \not{\kappa}$. However, it is not clear if these structures are relevant for the chiral dynamics investigated in this work, or if they might even suffer from similar caveats as the term proportional to $\sigma^{\mu\nu} F_{\mu\nu}$.

In chapter 4, we therefore started our investigations with the simplest possible Lorentz structure for the propagator,

$$S_F(\bar{p})^{-1} = B(\bar{p}) + i(A_0(\bar{p})\gamma^0\omega_p + A_2(\bar{p})\gamma^2(p_2)_\kappa + A_3(\bar{p})\gamma^3 p_3). \quad (\text{B.12})$$

The investigation of an extended propagator with additional dressing functions for the terms Eq. (B.11) is relegated to future investigations.

B.3. The Dyson Schwinger equation in an external magnetic field

In the very first sections, we extracted the quark DSE from the generating functional. The derivation procedure lead us to equations in coordinate space that we Fourier transformed to momentum space, where we wish to solve them on a compact manifold. With an external magnetic field, the discussion of Ritus' method in App. B.1 showed us, that this last part needs further attention. The propagator depends on a special subset of momenta (4.4), and is only diagonal if we consider the non-plane wave eigenfunctions. Besides a manifest spin dependence of the quark propagator itself (via the eigenfunctions) and of its argument $((p_2)_{n,\sigma})$ the parabolic cylinder functions lead to a modification of the quark-gluon coupling. The detailed steps of the Fourier transformation can be found in [185], or discussed under different aspects in [184, 186–189]. In the following, we provide a summary of the most important steps and specify our approximations.

The DSE in coordinate space reads

$$S^{-1}(x, x') \stackrel{=}{=}_0^{-1}(x, x') - iZ_{1F}g^2 \int d^4u d^4w \gamma_\mu S(x, x') \Gamma_\nu(u, w, x') D_{\mu\nu}(u, x'), \quad (\text{B.13})$$

with the dressed vertex $\Gamma_\nu(u, w, x')$ and gluon function $D_{\mu\nu}(u, x')$. The color indices are suppressed. With the help of Ritus' eigenfunctions, we can write down the corresponding equation in momentum space,

$$S^{-1}(\bar{p}) \stackrel{=}{=}_0^{-1}(\bar{p}) + \int d^4x d^4x' \mathbb{E}_p(x) \Sigma(x, x') \mathbb{E}_p(x'), \quad (\text{B.14})$$

where we need to elaborate on the Fourier transform of the self-energy term $\Sigma(x, x')$. We insert the Fourier transformation of the propagator into the self-energy kernel in B.14. Additionally, we replace the dressed vertex function Γ_ν by a second bare vertex in order to better keep track of the equations. The self-energy then reads

$$\begin{aligned} \Sigma(p, p') &= \int d^4x d^4x' \mathbb{E}_p(x) \left(\gamma_\mu S(x, x') \gamma_\nu D_{\mu\nu}(x - x') \right) \mathbb{E}_p(x'), \\ &= \int d^4x d^4x' \mathbb{E}_p(x) \left(\gamma_\mu \left[\sum \frac{d^4p'}{(2\pi)^4} \mathbb{E}_{p'}(x) S(p') \mathbb{E}_{p'}(x') \right] \times \right. \\ &\quad \left. \gamma_\nu \left[\int \frac{d^4k}{(2\pi)^4} e^{-ik(x-x')} D_{\mu\nu}(k) \right] \right) \mathbb{E}_p(x'), \end{aligned} \quad (\text{B.15})$$

where $\sum d^4p' = \sum_{(p_2)_{n,\sigma}} \int dp_0 dp_1 dp_3$. To further evaluate this expression, we need to solve to integrations over coordinate spacetime. Before we concentrate on this integration, we introduce the shorthand for the spin-vertex construction $\omega(\sigma) \gamma_\mu \omega(\sigma') =: \gamma_{\sigma\nu\sigma'}$. This will simplify to keep track of the equations. Furthermore, since the integrand over x and x' are basically the same, we only consider the integration over x as an example,

$$\begin{aligned} \int_{-\infty}^{\infty} d^4x \mathbb{E}_p(x) \gamma_\mu \mathbb{E}_{p'}(x) e^{-ikx} &= (2\pi)^3 \delta(p'_0 + k_0 - p_0) \delta(p'_2 + k_2 - p_2) \delta(p'_3 + k_3 - p_3) \times \\ &\quad \sum_{\sigma} N(n) N(n') \times \\ &\quad \int dx_1 D_n \left(\sqrt{2e\mathcal{B}} \left(x_1 - \frac{p_2}{e\mathcal{B}} \right) \right) D_{n'} \left(\sqrt{2e\mathcal{B}} \left(x_1 - \frac{p_2}{e\mathcal{B}} \right) \right) e^{-ik_1 x_1} \gamma_{\sigma\mu\sigma'}. \end{aligned} \quad (\text{B.16})$$

The integration yields three Dirac δ -functions, that we would also obtain without an external field. Due to the Ritus-eigenfunctions however, the momentum transfer to the gluon, in p_2 direction is now modified by the parabolic cylinder functions. The integral in x_1 direction can be further rearranged and simplified with the help of some general properties of the cylinder functions. The integral B.16 then yields

$$\int_{-\infty}^{\infty} dx \bar{\mathbb{E}}_p(x) \gamma_\mu \mathbb{E}_{p'}(x) e^{-ikx} = (2\pi)^3 \Pi_i \delta(p'_i + k_i - p_i) e^{ik_1(p'_2+p_2)/(2e\mathcal{B})} e^{-(k_1^2+k_2^2)/(2\sqrt{2e\mathcal{B}})} \times \\ \sum_{\sigma, \sigma'} \frac{1}{\sqrt{n!n'!}} e^{i(n-n') \arctan(k_2/k_1)} J_{nn'} \left(\frac{k_1^2 + k_2^2}{2\sqrt{2e\mathcal{B}}} \right) \gamma_{\sigma\mu\sigma'}.$$

with $i = 0, 2, 3$. The function $J_{nn'}$ arises from the integral over the cylinder functions and is given by

$$J_{nn'} \left(\frac{k_1^2 + k_2^2}{2\sqrt{2e\mathcal{B}}} \right) = \sum_{m=0}^{\min(n,n')} \frac{n!n'!}{m!(n-m)!(n'-m)!} \left(i \frac{k_1^2 + k_2^2}{2\sqrt{2e\mathcal{B}}} \right)^{n+n'-2m}.$$

With a similar result for the integral over x' , we can go back to the equation for the self-energy in momentum space that reads in full glory

$$\Sigma(\bar{p}) \delta_{(p_2)_{n,\sigma}, (p_2)_{n',\sigma'}} = iZ_{1F} g^2 (2e\mathcal{B}) \sum_{(p_2)_{n',\sigma'}} \sum_{\sigma_i} \int \frac{d^4k}{(2\pi)^4} e^{-(k_1^2+k_2^2)/(2\sqrt{2e\mathcal{B}})} \frac{e^{i(n-n'+n''-n'') \arctan(k_2/k_1)}}{\sqrt{n!n'!n''!n''''!}} \times \\ J_{nn'} \left(\frac{k_1^2 + k_2^2}{2\sqrt{2e\mathcal{B}}} \right) J_{n''n'''} \left(\frac{k_1^2 + k_2^2}{2\sqrt{2e\mathcal{B}}} \right) D_{\mu\nu}(k) \gamma_{\sigma\mu\sigma'} S(\bar{p}') \gamma_{\sigma''\nu\sigma'''}.$$

Since large gluon momenta in 12 direction are damped by the exponential, the self-energy can be further simplified by only keeping small powers of $J_{nn'}(k_1, k_2)$,

$$J_{n''n'''} \left(\frac{k_1^2 + k_2^2}{2\sqrt{2e\mathcal{B}}} \right) \rightarrow \frac{[\max(n, n')]!}{|n - n'|!} \left[i \frac{k_1^2 + k_2^2}{2\sqrt{2e\mathcal{B}}} \right]^{|n-n'|} \rightarrow n! \delta_{nn'}. \quad (\text{B.17})$$

The DSE then reads

$$\Sigma(\bar{p}) \delta_{(p_2)_{n,\sigma}, (p_2)_{n',\sigma'}} = iZ_{1F} g^2 (2e\mathcal{B}) \sum_{p_2} \sum_{\sigma_i} \delta_{n,n'} \delta_{n,n''} \times \\ \int \frac{d^4\bar{q}}{(2\pi)^4} e^{-(k_1^2+k_2^2)/(2\sqrt{2e\mathcal{B}})} D_{\mu\nu}(k) \gamma_{\sigma\mu\sigma'} S(\bar{p}') \gamma_{\sigma''\nu\sigma'''}.$$

This is the result for the quark self-energy obtained in [187]. For this work, we further approximated this expression for first investigations. To this end, we imposed an artificial momentum conservation in 12 direction, thus neglecting the damping factor for large gluon momenta. Additionally, we neglected the spin-matrix modifications of the vertex, $\omega(\sigma) \gamma_\mu t^a \omega(\sigma') \sim \gamma_\mu t^a$. In consequence, our first investigations are dedicated to study the Dyson–Schwinger equation for a magnetic field modified quark propagator only. We address this approximation as the bare vertex approximation throughout this work.

$$\Sigma(\bar{p}) = iZ_{1F} g^2 (2e\mathcal{B}) \oint \frac{d^4\bar{q}}{(2\pi)^4} \gamma_\mu S(\bar{q}) \gamma_\nu D_{\mu\nu}(\bar{p} - \bar{q}),$$

where $\int d^4\bar{q} = \int dq_0 dp_1 dq_3 \sum_{\kappa}$ and the momenta are given by $k_0 = \bar{p}_0 - \bar{q}_0$, $k_3 = \bar{p}_3 - \bar{q}_3$, $\bar{p}_1 = \bar{q}_1 = 0$ and $\bar{q}_2 = \sqrt{2e\mathcal{B}\kappa}$. In a second step, we include the exponential damping of large gluon momenta, but still insert spin-summed vertices. The quark self-energy then reads

$$\Sigma(\bar{p}) = iZ_{1F}g^2(2e\mathcal{B}) \int \frac{d^4\bar{q}}{(2\pi)^2} \int \frac{dk_1 dk_2}{(2\pi)^2} e^{-(k_1^2+k_2^2)/(2\sqrt{2e\mathcal{B}})} D_{\mu\nu}(k) \gamma_{\mu} S(\bar{q}) \gamma_{\nu}.$$

The investigation of the full magnetic field DSE, including the additional Lorentz scalar structures in the dressed quark propagator (see B.2), will be subject of future studies.

Bibliography

- [1] Craig D. Roberts and Anthony G. Williams. Dyson-Schwinger equations and their application to hadronic physics. *Prog.Part.Nucl.Phys.*, 33:477–575, 1994.
- [2] Craig D. Roberts and Sebastian M. Schmidt. Dyson-Schwinger equations: Density, temperature and continuum strong QCD. *Prog.Part.Nucl.Phys.*, 45:S1–S103, 2000.
- [3] Reinhard Alkofer and Lorenz von Smekal. The Infrared behavior of QCD Green’s functions: Confinement dynamical symmetry breaking, and hadrons as relativistic bound states. *Phys.Rept.*, 353:281, 2001.
- [4] Eric S. Swanson. A Primer on Functional Methods and the Schwinger-Dyson Equations. *AIP Conf.Proc.*, 1296:75–121, 2010.
- [5] Carina Popovici. Dyson-Schwinger approach to strongly coupled theories. *Mod.Phys.Lett.*, A28:1330006, 2013.
- [6] D.J. Gross and Frank Wilczek. Ultraviolet Behavior of Nonabelian Gauge Theories. *Phys.Rev.Lett.*, 30:1343–1346, 1973.
- [7] H. David Politzer. Reliable Perturbative Results for Strong Interactions? *Phys.Rev.Lett.*, 30:1346–1349, 1973.
- [8] Francesco Sannino. Conformal Dynamics for TeV Physics and Cosmology. *Acta Phys.Polon.*, B40:3533–3743, 2009.
- [9] V.P. Gusynin, V.A. Miransky, and A.V. Shpagin. Effective action and conformal phase transition in QED(3). *Phys.Rev.*, D58:085023, 1998.
- [10] V.A. Miransky and Koichi Yamawaki. Conformal phase transition in gauge theories. *Phys.Rev.*, D55:5051–5066, 1997.
- [11] C.S. Fischer, Reinhard Alkofer, T. Dahm, and P. Maris. Dynamical chiral symmetry breaking in unquenched QED(3). *Phys.Rev.*, D70:073007, 2004.
- [12] Conrad J. Burden and Craig D. Roberts. Light cone regular vertex in quenched QED in three-dimensions. *Phys.Rev.*, D44:540–550, 1991.
- [13] Gerard ’t Hooft. Monopoles, instantons and confinement. 1999.
- [14] Michael E. Peskin and Daniel V. Schroeder. An Introduction to quantum field theory. 1995.
- [15] J.I. Kapusta and Charles Gale. Finite-temperature field theory: Principles and applications. 2006.

- [16] Jeff Greensite. An introduction to the confinement problem. *Lect.Notes Phys.*, 821:1–211, 2011.
- [17] Christof Gattringer and Christian B. Lang. Quantum chromodynamics on the lattice. *Lect.Notes Phys.*, 788:1–211, 2010.
- [18] Andreas Wipf. Statistical approach to quantum field theory. *Lect.Notes Phys.*, 864, 2013.
- [19] John M. Cornwall, R. Jackiw, and E. Tomboulis. Effective Action for Composite Operators. *Phys.Rev.*, D10:2428–2445, 1974.
- [20] Dominic J. Lee and Igor F. Herbut. The Effect of velocity anisotropy on the antiferromagnetic instability of d wave superconductors. *Phys.Rev.*, B66:094512, 2002.
- [21] L.D. Faddeev and V.N. Popov. Feynman Diagrams for the Yang-Mills Field. *Phys.Lett.*, B25:29–30, 1967.
- [22] V.N. Gribov. Quantization of Nonabelian Gauge Theories. *Nucl.Phys.*, B139:1, 1978.
- [23] Kurt Langfeld. The Gribov problem and its solution from a toy model point of view. 2003.
- [24] A. Sternbeck, E.-M. Ilgenfritz, M. Muller-Preussker, and A. Schiller. Towards the infrared limit in SU(3) Landau gauge lattice gluodynamics. *Phys.Rev.*, D72:014507, 2005.
- [25] V. L. Berezinskii. . *Zh. Eksp. Teor. Fiz*, 59, No 3:907–920, 1970.
- [26] J.M. Kosterlitz and D.J. Thouless. Ordering, metastability and phase transitions in two-dimensional systems. *J.Phys.*, C6:1181–1203, 1973.
- [27] J.M. Kosterlitz. The Critical properties of the two-dimensional x y model. *J.Phys.*, 7:1046–1060, 1974.
- [28] K.G. Wilson and John B. Kogut. The Renormalization group and the epsilon expansion. *Phys.Rept.*, 12:75–200, 1974.
- [29] Holger Gies and Joerg Jaeckel. Chiral phase structure of QCD with many flavors. *Eur.Phys.J.*, C46:433–438, 2006.
- [30] D.B. Kaplan, J.W. Lee, D.T. Son, and M.A. Stephanov. Conformality lost. *Int.J.Mod.Phys.*, A25:422–432, 2010.
- [31] William E. Caswell. Asymptotic Behavior of Nonabelian Gauge Theories to Two Loop Order. *Phys.Rev.Lett.*, 33:244, 1974.
- [32] Tom Banks and A. Zaks. On the Phase Structure of Vector-Like Gauge Theories with Massless Fermions. *Nucl.Phys.*, B196:189, 1982.
- [33] Taichiro Kugo and Izumi Ojima. Local Covariant Operator Formalism of Nonabelian Gauge Theories and Quark Confinement Problem. *Prog. Theor. Phys. Suppl.*, 66:1, 1979.

-
- [34] D. Zwanziger. Vanishing of zero momentum lattice gluon propagator and color confinement. *Nucl. Phys.*, B364:127–161, 1991.
- [35] Christian S. Fischer and Jan M. Pawłowski. Uniqueness of infrared asymptotics in Landau gauge Yang-Mills theory. *Phys.Rev.*, D75:025012, 2007.
- [36] Christian S. Fischer and Jan M. Pawłowski. Uniqueness of infrared asymptotics in Landau gauge Yang-Mills theory II. *Phys.Rev.*, D80:025023, 2009.
- [37] Reinhard Alkofer, Christian S. Fischer, Felipe J. Llanes-Estrada, and Kai Schwenzer. The Quark-gluon vertex in Landau gauge QCD: Its role in dynamical chiral symmetry breaking and quark confinement. *Annals Phys.*, 324:106–172, 2009.
- [38] Adnan Bashir and Alfredo Raya. Gauge symmetry and its implications for the Schwinger-Dyson equations. 2004.
- [39] C.J. Burden and P.C. Tjiang. Deconstructing the vertex Ansatz in three-dimensional quantum electrodynamics. *Phys.Rev.*, D58:085019, 1998.
- [40] Richard Williams. Schwinger-Dyson Equations In QED and QCD- The calculation of fermion-antifermion condensates. *PhD Thesis, Durham university*, 2007.
- [41] D.C. Curtis and M.R. Pennington. Truncating the Schwinger-Dyson equations: How multiplicative renormalizability and the Ward identity restrict the three point vertex in QED. *Phys.Rev.*, D42:4165–4169, 1990.
- [42] Christian S. Fischer and Richard Williams. Beyond the rainbow: Effects from pion back-coupling. *Phys.Rev.*, D78:074006, 2008.
- [43] Christian S. Fischer and Richard Williams. Probing the gluon self-interaction in light mesons. *Phys.Rev.Lett.*, 103:122001, 2009.
- [44] Lei Chang, Yu-Xin Liu, and Craig D. Roberts. Dressed-quark anomalous magnetic moments. *Phys.Rev.Lett.*, 106:072001, 2011.
- [45] Markus Hopfer, Andreas Windisch, and Reinhard Alkofer. The Quark-Gluon Vertex in Landau gauge QCD. *PoS, CONFINEMENTX:073*, 2013.
- [46] Thomas W. Appelquist, Mark J. Bowick, Dimitra Karabali, and L.C.R. Wijewardhana. Spontaneous Chiral Symmetry Breaking in Three-Dimensional QED. *Phys.Rev.*, D33:3704, 1986.
- [47] Julian S. Schwinger. Gauge Invariance and Mass. 2. *Phys.Rev.*, 128:2425–2429, 1962.
- [48] Julian S. Schwinger. Gauge Invariance and Mass. *Phys.Rev.*, 125:397–398, 1962.
- [49] Jacqueline A. Bonnet, Christian S. Fischer, and Richard Williams. Effects of Anisotropy in *QED*₃ from Dyson-Schwinger equations in a box. *Phys.Rev.*, B84:024520, 2011.
- [50] Jacqueline A. Bonnet and Christian S. Fischer. Critical scaling of finite temperature *QED*₃ in anisotropic space-time. *Phys.Lett.*, B718:532–537, 2012.

- [51] K. S. Novoselov, A. K. Geim, S. V. Morozov, D. Jiang, Y. Zhang, S. V. Dubonos, I. V. Grigorieva, and A. A. Firsov. Electric Field Effect in Atomically Thin Carbon Films. *Science*, 306:666–669, October 2004.
- [52] K.S. Novoselov, A.K. Geim, S.V. Morozov, D. Jiang, M.I. Katsnelson, et al. Two-dimensional gas of massless Dirac fermions in graphene. *Nature*, 438:197, 2005.
- [53] M. Franz and Z. Tešanović. Quasiparticles in the vortex lattice of unconventional superconductors: Bloch waves or Landau levels? *Phys. Rev. Lett.*, 84:554–557, Jan 2000.
- [54] O. Vafek, A. Melikyan, M. Franz, and Z. Tešanović. Quasiparticles and vortices in unconventional superconductors. *Phys. Rev. B*, 63:134509, Mar 2001.
- [55] M. Franz and Z. Teseanovic. Algebraic Fermi Liquid from Phase Fluctuations: 'Topological' Fermions, Vortex 'Berryons,' and QED(3) Theory of Cuprate Superconductors. *Phys.Rev.Lett.*, 87:257003, 2001.
- [56] M. Franz, Z. Teseanovic, and O. Vafek. QED(3) theory of pairing pseudogap in cuprates. 1. From D wave superconductor to antiferromagnet via 'algebraic' Fermi liquid. *Phys.Rev.*, B66:054535, 2002.
- [57] Igor F. Herbut and Dominic J. Lee. Theory of phase fluctuating d wave superconductors and the spin response in underdoped cuprates. 2002.
- [58] Luca Marinelli, B. I. Halperin, and S. H. Simon. Quasiparticle spectrum of d-wave superconductors in the mixed state. *Phys. Rev. B*, 62:3488–3501, Aug 2000.
- [59] A. Concha, V. Stanev, and Z. Teseanovic. A Criterion for the Critical Number of Fermions and Chiral Symmetry Breaking in Anisotropic QED(2+1). *Phys.Rev.*, B79:214525, 2009.
- [60] J.G. Bednorz and K.A. Müller. Possible high temperature superconductivity in the Ba-La-Cu-O system. 64(2):189–193.
- [61] John Bardeen, L.N. Cooper, and J.R. Schrieffer. Theory of superconductivity. *Phys.Rev.*, 108:1175–1204, 1957.
- [62] John Bardeen, L.N. Cooper, and J.R. Schrieffer. Microscopic theory of superconductivity. *Phys.Rev.*, 106:162, 1957.
- [63] Igor F. Herbut. QED(3) theory of underdoped high temperature superconductors. *Phys.Rev.*, B66:094504, 2002.
- [64] H. Ding, M. R. Norman, J. C. Campuzano, M. Randeria, A. F. Bellman, T. Yokoya, T. Takahashi, T. Mochiku, and K. Kadowaki. Angle-resolved photoemission spectroscopy study of the superconducting gap anisotropy in Bi₂Sr₂CaCu₂O_{8+x}. *Phys. Rev. B*, 54:R9678–R9681, Oct 1996.
- [65] Leon Balents, Matthew P.A. Fisher, and Chetan Nayak. Dual order parameter for the nodal liquid. *Phys.Rev.*, B60:1654–1667, 1999.

-
- [66] Simon Hands and Iorwerth Owain Thomas. Lattice study of anisotropic QED(3). *Phys.Rev.*, B72:054526, 2005.
- [67] A. Bashir, A. Kizilersu, and M.R. Pennington. Analytic form of the one loop vertex and of the two loop fermion propagator in three-dimensional massless QED. 1999.
- [68] A. Kizilersu and M.R. Pennington. Building the Full Fermion-Photon Vertex of QED by Imposing Multiplicative Renormalizability of the Schwinger-Dyson Equations for the Fermion and Photon Propagators. *Phys.Rev.*, D79:125020, 2009.
- [69] James S. Ball and Ting-Wai Chiu. Analytic Properties of the Vertex Function in Gauge Theories. 1. *Phys.Rev.*, D22:2542, 1980.
- [70] P. Maris. The Influence of the full vertex and vacuum polarization on the fermion propagator in QED in three-dimensions. *Phys.Rev.*, D54:4049–4058, 1996.
- [71] Robert D. Pisarski. Chiral Symmetry Breaking in Three-Dimensional Electrodynamics. *Phys.Rev.*, D29:2423, 1984.
- [72] Thomas Appelquist, Daniel Nash, and L.C.R. Wijewardhana. Critical Behavior in (2+1)-Dimensional QED. *Phys.Rev.Lett.*, 60:2575, 1988.
- [73] Daniel Nash. Higher Order Corrections in (2+1)-Dimensional QED. *Phys.Rev.Lett.*, 62:3024, 1989.
- [74] Christian S. Fischer. Nonperturbative propagators, running coupling and dynamical mass generation in ghost - anti-ghost symmetric gauges in QCD. 2003.
- [75] Tobias Goecke, Christian S. Fischer, and Richard Williams. Finite volume effects and dynamical chiral symmetry breaking in QED3. *Phys.Rev.*, B79:064513, 2009.
- [76] C.S. Fischer, Reinhard Alkofer, and H. Reinhardt. The Elusiveness of infrared critical exponents in Landau gauge Yang-Mills theories. *Phys.Rev.*, D65:094008, 2002.
- [77] C.S. Fischer and M.R. Pennington. Finite volume effects in a quenched lattice-QCD quark propagator. *Phys.Rev.*, D73:034029, 2006.
- [78] Iorwerth Owain Thomas and Simon Hands. Fermion propagators in QED(3) with velocity anisotropies. *PoS*, LAT2005:249, 2006.
- [79] Iorwerth Owain Thomas and Simon Hands. Chiral symmetry restoration in anisotropic QED(3). *Phys.Rev.*, B75:134516, 2007.
- [80] V.A. Miransky and K. Yamawaki. On Gauge Theories with Additional Four Fermion Interaction. *Mod.Phys.Lett.*, A4:129–135, 1989.
- [81] May Chiao, R. W. Hill, Christian Lupien, Louis Taillefer, P. Lambert, R. Gagnon, and P. Fournier. Low-energy quasiparticles in cuprate superconductors: A quantitative analysis. *Phys. Rev. B*, 62:3554–3558, Aug 2000.
- [82] Jens Braun and Holger Gies. Running coupling at finite temperature and chiral symmetry restoration in QCD. *Phys.Lett.*, B645:53–58, 2007.
-

- [83] Jens Braun and Holger Gies. Chiral phase boundary of QCD at finite temperature. *JHEP*, 0606:024, 2006.
- [84] Jens Braun and Holger Gies. Scaling laws near the conformal window of many-flavor QCD. *JHEP*, 1005:060, 2010.
- [85] David B. Kaplan, Jong-Wan Lee, Dam T. Son, and Mikhail A. Stephanov. Conformality Lost. *Phys.Rev.*, D80:125005, 2009.
- [86] Jens Braun, Christian S. Fischer, and Holger Gies. Beyond Miransky Scaling. *Phys.Rev.*, D84:034045, 2011.
- [87] Jens Braun. Thermodynamics of QCD low-energy models and the derivative expansion of the effective action. *Phys.Rev.*, D81:016008, 2010.
- [88] Jens Braun. Fermion Interactions and Universal Behavior in Strongly Interacting Theories. *J.Phys.*, G39:033001, 2012.
- [89] Kenji Fukushima and Tetsuo Hatsuda. The phase diagram of dense QCD. *Rept.Prog.Phys.*, 74:014001, 2011.
- [90] Ana Julia Mizher, M.N. Chernodub, and Eduardo S. Fraga. Phase diagram of hot QCD in an external magnetic field: possible splitting of deconfinement and chiral transitions. *Phys.Rev.*, D82:105016, 2010.
- [91] Kenji Fukushima. Chiral effective model with the Polyakov loop. *Phys.Lett.*, B591:277–284, 2004.
- [92] Claudia Ratti, Michael A. Thaler, and Wolfram Weise. Phases of QCD: Lattice thermodynamics and a field theoretical model. *Phys.Rev.*, D73:014019, 2006.
- [93] Bernd-Jochen Schaefer, Jan M. Pawłowski, and Jochen Wambach. The Phase Structure of the Polyakov–Quark–Meson Model. *Phys.Rev.*, D76:074023, 2007.
- [94] V. Skokov, B. Stokic, B. Friman, and K. Redlich. Meson fluctuations and thermodynamics of the Polyakov loop extended quark-meson model. *Phys.Rev.*, C82:015206, 2010.
- [95] Tina Katharina Herbst, Jan M. Pawłowski, and Bernd-Jochen Schaefer. The phase structure of the Polyakov–quark-meson model beyond mean field. *Phys.Lett.*, B696:58–67, 2011.
- [96] N. Cabibbo and G. Parisi. Exponential Hadronic Spectrum and Quark Liberation. *Phys.Lett.*, B59:67–69, 1975.
- [97] Julian S. Schwinger. On gauge invariance and vacuum polarization. *Phys.Rev.*, 82:664–679, 1951.
- [98] V.P. Gusynin, V.A. Miransky, and I.A. Shovkovy. Catalysis of dynamical flavor symmetry breaking by a magnetic field in (2+1)-dimensions. *Phys.Rev.Lett.*, 73:3499–3502, 1994.

-
- [99] V.P. Gusynin, V.A. Miransky, and I.A. Shovkovy. Dynamical chiral symmetry breaking by a magnetic field in QED. *Phys.Rev.*, D52:4747–4751, 1995.
- [100] V.P. Gusynin, V.A. Miransky, and I.A. Shovkovy. Dimensional reduction and dynamical chiral symmetry breaking by a magnetic field in (3+1)-dimensions. *Phys.Lett.*, B349:477–483, 1995.
- [101] V.P. Gusynin, V.A. Miransky, and I.A. Shovkovy. Dimensional reduction and catalysis of dynamical symmetry breaking by a magnetic field. *Nucl.Phys.*, B462:249–290, 1996.
- [102] K.G. Klimenko. Three-dimensional Gross-Neveu model in an external magnetic field. *Theor.Math.Phys.*, 89:1161–1168, 1992.
- [103] K.G. Klimenko. Three-dimensional Gross-Neveu model at nonzero temperature and in an external magnetic field. *Theor.Math.Phys.*, 90:1–6, 1992.
- [104] I.A. Shushpanov and Andrei V. Smilga. Quark condensate in a magnetic field. *Phys.Lett.*, B402:351–358, 1997.
- [105] Igor A. Shovkovy. Magnetic Catalysis: A Review. *Lect.Notes Phys.*, 871:13–49, 2013.
- [106] Kenji Fukushima. Chiral Symmetry and Heavy-Ion Collisions. *J.Phys.*, G35:104020, 2008.
- [107] Kenji Fukushima. QCD matter in extreme environments. *J.Phys.*, G39:013101, 2012.
- [108] Nikita O. Agasian and I.A. Shushpanov. The Quark and gluon condensates and low-energy QCD theorems in a magnetic field. *Phys.Lett.*, B472:143–149, 2000.
- [109] Nikita O. Agasian. Chiral thermodynamics in a magnetic field. *Phys.Atom.Nucl.*, 64:554–560, 2001.
- [110] Thomas D. Cohen, David A. McGady, and Elizabeth S. Werbos. The Chiral condensate in a constant electromagnetic field. *Phys.Rev.*, C76:055201, 2007.
- [111] Jens O. Andersen. Thermal pions in a magnetic background. *Phys.Rev.*, D86:025020, 2012.
- [112] Jens O. Andersen. Chiral perturbation theory in a magnetic background - finite-temperature effects. *JHEP*, 1210:005, 2012.
- [113] S.P. Klevansky and Richard H. Lemmer. Chiral symmetry restoration in the Nambu-Jona-Lasinio model with a constant electromagnetic field. *Phys.Rev.*, D39:3478–3489, 1989.
- [114] D.P. Menezes, M. Benghi Pinto, S.S. Avancini, and C. Providencia. Quark matter under strong magnetic fields in the su(3) Nambu-Jona-Lasinio Model. *Phys.Rev.*, C80:065805, 2009.

- [115] Raoul Gatto and Marco Ruggieri. Deconfinement and Chiral Symmetry Restoration in a Strong Magnetic Background. *Phys.Rev.*, D83:034016, 2011.
- [116] Raoul Gatto and Marco Ruggieri. Dressed Polyakov loop and phase diagram of hot quark matter under magnetic field. *Phys.Rev.*, D82:054027, 2010.
- [117] Kouji Kashiwa. Entanglement between chiral and deconfinement transitions under strong uniform magnetic background field. *Phys.Rev.*, D83:117901, 2011.
- [118] Jens O. Andersen and Rashid Khan. Chiral transition in a magnetic field and at finite baryon density. *Phys.Rev.*, D85:065026, 2012.
- [119] Sidney S. Avancini, Debora P. Menezes, Marcus B. Pinto, and Constanca Providencia. The QCD Critical End Point Under Strong Magnetic Fields. *Phys.Rev.*, D85:091901, 2012.
- [120] Kenji Fukushima and Jan M. Pawłowski. Magnetic catalysis in hot and dense quark matter and quantum fluctuations. *Phys.Rev.*, D86:076013, 2012.
- [121] Jens O. Andersen and Anders Tranberg. The Chiral transition in a magnetic background: Finite density effects and the functional renormalization group. *JHEP*, 1208:002, 2012.
- [122] Shinya Kanemura, Haru-Tada Sato, and Hiroshi Tochimura. Thermodynamic Gross-Neveu model under constant electromagnetic field. *Nucl.Phys.*, B517:567–598, 1998.
- [123] J. Alexandre, K. Farakos, and G. Koutsoumbas. Magnetic catalysis in QED(3) at finite temperature: Beyond the constant mass approximation. *Phys.Rev.*, D63:065015, 2001.
- [124] Daniel D. Scherer and Holger Gies. Renormalization Group Study of Magnetic Catalysis in the 3d Gross-Neveu Model. *Phys.Rev.*, B85:195417, 2012.
- [125] Clifford V. Johnson and Arnab Kundu. External Fields and Chiral Symmetry Breaking in the Sakai-Sugimoto Model. *JHEP*, 0812:053, 2008.
- [126] Florian Preis, Anton Rebhan, and Andreas Schmitt. Inverse magnetic catalysis in dense holographic matter. *JHEP*, 1103:033, 2011.
- [127] Ana Julia Mizher, Eduardo S. Fraga, and M.N. Chernodub. Phase Diagram of Strong Interactions in an External Magnetic Field. *PoS*, FACESQCD:020, 2010.
- [128] J. Gasser and H. Leutwyler. Light Quarks at Low Temperatures. *Phys.Lett.*, B184:83, 1987.
- [129] J. Gasser and H. Leutwyler. Thermodynamics of Chiral Symmetry. *Phys.Lett.*, B188:477, 1987.
- [130] P. Gerber and H. Leutwyler. Hadrons Below the Chiral Phase Transition. *Nucl.Phys.*, B321:387, 1989.
- [131] Eduardo S. Fraga and Ana Julia Mizher. Can a strong magnetic background modify the nature of the chiral transition in QCD? *Nucl.Phys.*, A820:103C–106C, 2009.

- [132] Raoul Gatto and Marco Ruggieri. Hot Quark Matter with an Axial Chemical Potential. *Phys.Rev.*, D85:054013, 2012.
- [133] V. Skokov. Phase diagram in an external magnetic field beyond a mean-field approximation. *Phys.Rev.*, D85:034026, 2012.
- [134] P.V. Buividovich, M.N. Chernodub, E.V. Luschevskaya, and M.I. Polikarpov. Numerical study of chiral symmetry breaking in non-Abelian gauge theory with background magnetic field. *Phys.Lett.*, B682:484–489, 2010.
- [135] V.V. Braguta, P.V. Buividovich, T. Kalaydzhyan, S.V. Kuznetsov, and M.I. Polikarpov. The Chiral Magnetic Effect and chiral symmetry breaking in SU(3) quenched lattice gauge theory. *Phys.Atom.Nucl.*, 75:488–492, 2012.
- [136] Massimo D’Elia, Swagato Mukherjee, and Francesco Sanfilippo. QCD Phase Transition in a Strong Magnetic Background. *Phys.Rev.*, D82:051501, 2010.
- [137] Massimo D’Elia and Francesco Negro. Chiral Properties of Strong Interactions in a Magnetic Background. *Phys.Rev.*, D83:114028, 2011.
- [138] G.S. Bali, F. Bruckmann, G. Endrodi, Z. Fodor, S.D. Katz, et al. The QCD phase diagram for external magnetic fields. *JHEP*, 1202:044, 2012.
- [139] Kenji Fukushima and Yoshimasa Hidaka. Magnetic Catalysis vs Magnetic Inhibition. *Phys.Rev.Lett.*, 110:031601, 2013.
- [140] Márcio Ferreira, Pedro Costa, Débora P. Menezes, Constança Providência, and Norberto Scoccola. Deconfinement and chiral restoration within the SU(3) PNJL and EPNJL models in an external magnetic field. 2013.
- [141] Falk Bruckmann, Gergely Endrodi, and Tamas G. Kovacs. Inverse magnetic catalysis and the Polyakov loop. *JHEP*, 1304:112, 2013.
- [142] Christian S. Fischer and Jan Luecker. Propagators and phase structure of Nf=2 and Nf=2+1 QCD. *Phys.Lett.*, B718:1036–1043, 2013.
- [143] Dmitri E. Kharzeev, Larry D. McLerran, and Harmen J. Warringa. The Effects of topological charge change in heavy ion collisions: ‘Event by event P and CP violation’. *Nucl.Phys.*, A803:227–253, 2008.
- [144] V. Skokov, A. Yu. Illarionov, and V. Toneev. Estimate of the magnetic field strength in heavy-ion collisions. *Int.J.Mod.Phys.*, A24:5925–5932, 2009.
- [145] Adam Bzdak and Vladimir Skokov. Event-by-event fluctuations of magnetic and electric fields in heavy ion collisions. *Phys.Lett.*, B710:171–174, 2012.
- [146] Robert C. Duncan and Christopher Thompson. Formation of very strongly magnetized neutron stars - implications for gamma-ray bursts. *Astrophys.J.*, 392:L9, 1992.
- [147] K. Enqvist and P. Olesen. On primordial magnetic fields of electroweak origin. *Phys.Lett.*, B319:178–185, 1993.

- [148] T. Vachaspati. Magnetic fields from cosmological phase transitions. *Phys.Lett.*, B265:258–261, 1991.
- [149] Berndt Muller and James L. Nagle. Results from the relativistic heavy ion collider. *Ann.Rev.Nucl.Part.Sci.*, 56:93–135, 2006.
- [150] Berndt Muller. From Quark-Gluon Plasma to the Perfect Liquid. *Acta Phys.Polon.*, B38:3705–3730, 2007.
- [151] Kenji Fukushima, Dmitri E. Kharzeev, and Harmen J. Warringa. The Chiral Magnetic Effect. *Phys.Rev.*, D78:074033, 2008.
- [152] L.F. Palhares, E.S. Fraga, and T. Kodama. Chiral transition in a finite system and possible use of finite size scaling in relativistic heavy ion collisions. *J.Phys.*, 38:085101, 2011.
- [153] Eduardo S. Fraga, Leticia F. Palhares, and Paul Sorensen. Finite-size scaling as a tool in the search for the QCD critical point in heavy ion data. *Phys.Rev.*, C84:011903, 2011.
- [154] L. McLerran and V. Skokov. Comments About the Electromagnetic Field in Heavy-Ion Collisions. 2013.
- [155] Kirill Tuchin. Time and space dependence of electromagnetic field in relativistic heavy-ion collisions. 2013.
- [156] Falk Bruckmann and Gergely Endrodi. Dressed Wilson loops as dual condensates in response to magnetic and electric fields. *Phys.Rev.*, D84:074506, 2011.
- [157] V.I. Ritus. Method of Eigenfunctions in Quantum Electrodynamics of an Arbitrary Constant Field. 1977.
- [158] V.I. Ritus. Method of eigenfunctions and mass operator in quantum electrodynamics of a constant field. *Sov.Phys.JETP*, 48:788, 1978.
- [159] V.I. Ritus. Radiative corrections in quantum electrodynamics with intense field and their analytical properties. *Annals Phys.*, 69:555–582, 1972.
- [160] Christian S. Fischer, Jan Luecker, and Jens A. Mueller. Chiral and deconfinement phase transitions of two-flavour QCD at finite temperature and chemical potential. *Phys.Lett.*, B702:438–441, 2011.
- [161] Pieter Maris, Craig D. Roberts, and Peter C. Tandy. Pion mass and decay constant. *Phys.Lett.*, B420:267–273, 1998.
- [162] Heinz Pagels and Saul Stokar. The Pion Decay Constant, Electromagnetic Form-Factor and Quark Electromagnetic Selfenergy in QCD. *Phys.Rev.*, D20:2947, 1979.
- [163] Larry D. McLerran and Benjamin Svetitsky. Quark Liberation at High Temperature: A Monte Carlo Study of SU(2) Gauge Theory. *Phys.Rev.*, D24:450, 1981.

-
- [164] Christof Gattringer. Linking confinement to spectral properties of the Dirac operator. *Phys.Rev.Lett.*, 97:032003, 2006.
- [165] Tom Banks and A. Casher. Chiral Symmetry Breaking in Confining Theories. *Nucl.Phys.*, B169:103, 1980.
- [166] Falk Bruckmann, Christof Gattringer, and Christian Hagen. Complete spectra of the Dirac operator and their relation to confinement. *Phys.Lett.*, B647:56–61, 2007.
- [167] Franziska Synatschke, Andreas Wipf, and Christian Wozar. Spectral sums of the Dirac-Wilson operator and their relation to the Polyakov loop. *Phys.Rev.*, D75:114003, 2007.
- [168] Wolfgang Soldner. The Polyakov Loop and the Eigenvalues of the Dirac Operator. *PoS*, LAT2007:222, 2007.
- [169] Franziska Synatschke, Andreas Wipf, and Kurt Langfeld. Relation between chiral symmetry breaking and confinement in YM-theories. *Phys.Rev.*, D77:114018, 2008.
- [170] Christian Hagen, Falk Bruckmann, Erek Bilgici, and Christof Gattringer. Thin and dressed Polyakov loops from spectral sums of lattice differential operators. *PoS*, LAT2007:289, 2007.
- [171] Erek Bilgici, Falk Bruckmann, Christof Gattringer, and Christian Hagen. Dual quark condensate and dressed Polyakov loops. *Phys.Rev.*, D77:094007, 2008.
- [172] Jens A. Müller. A Dyson–Schwinger approach to finite temperature QCD. *PhD Thesis, TU Darmstadt*, 2013.
- [173] Jan Lücker. Chiral and Deconfinement Phase Transitions in $N_f = 2$ and $N_f = 2 + 1$ Quantum Chromodynamics . *PhD Thesis, JLU Giessen*, 2013.
- [174] M.H. Al-Hashimi and U.-J. Wiese. Discrete Accidental Symmetry for a Particle in a Constant Magnetic Field on a Torus. *Annals Phys.*, 324:343–360, 2009.
- [175] N.D. Mermin and H. Wagner. Absence of ferromagnetism or antiferromagnetism in one-dimensional or two-dimensional isotropic Heisenberg models. *Phys.Rev.Lett.*, 17:1133–1136, 1966.
- [176] Sidney R. Coleman. There are no Goldstone bosons in two-dimensions. *Commun.Math.Phys.*, 31:259–264, 1973.
- [177] Jan Luecker, Christian S. Fischer, and Richard Williams. Volume behaviour of quark condensate, pion mass and decay constant from Dyson-Schwinger equations. *Phys.Rev.*, D81:094005, 2010.
- [178] Jan Luecker and Christian S. Fischer. Two-flavor QCD at finite temperature and chemical potential in a functional approach. *Prog.Part.Nucl.Phys.*, 67:200–205, 2012.
- [179] M. Franz, Z. Tesanovic, and O. Vafek. Gauge invariant fermion propagator in QED(3). 2002.

- [180] Tobias Goecke. On the critical number of flavours in QED_3 as an effective theory of Cuprate superconductors. *diploma thesis, TU Darmstadt*, 2008.
- [181] J.A.Bonnet. Effects of anisotropy in (2+1) dimensional QED. *Master's Thesis, TU Darmstadt*, 2010.
- [182] Gabriela Murguia, Alfredo Raya, Angel Sanchez, and Edward Reyes. The Electron Propagator in External Electromagnetic Fields in Lower Dimensions. *Am.J.Phys.*, 78:700–707, 2010.
- [183] Kaushik Bhattacharya. Solution of the Dirac equation in presence of an uniform magnetic field. 2007.
- [184] Chung Ngoc Leung and Shang-Yung Wang. Gauge independent approach to chiral symmetry breaking in a strong magnetic field. *Nucl.Phys.*, B747:266–293, 2006.
- [185] Chung Ngoc Leung, Y.J. Ng, and A.W. Ackley. Schwinger-Dyson equation approach to chiral symmetry breaking in an external magnetic field. *Phys.Rev.*, D54:4181–4184, 1996.
- [186] D.S. Lee, Chung Ngoc Leung, and Y.J. Ng. Chiral symmetry breaking in a uniform external magnetic field. 2. Symmetry restoration at high temperatures and chemical potentials. *Phys.Rev.*, D57:5224–5229, 1998.
- [187] D.S. Lee, Chung Ngoc Leung, and Y.J. Ng. Chiral symmetry breaking in a uniform external magnetic field. *Phys.Rev.*, D55:6504–6513, 1997.
- [188] Y. Jack Ng. Magnetic catalysis of chiral symmetry breaking and the Pauli problem. pages 557–563, 1998.
- [189] Chung Ngoc Leung and Shang-Yung Wang. Gauge independence and chiral symmetry breaking in a strong magnetic field. *Annals Phys.*, 322:701–708, 2007.

Eigenständigkeitserklärung

Ich erkläre:

Ich habe die vorgelegte Dissertation selbstständig und ohne unerlaubte fremde Hilfe und nur mit den Hilfen angefertigt, die ich in der Dissertation angegeben habe. Alle Textstellen, die wörtlich oder sinngemäß aus veröffentlichten Schriften entnommen sind, und alle Angaben, die auf mündlichen Auskünften beruhen, sind als solche kenntlich gemacht. Bei den von mir durchgeführten und in der Dissertation erwähnten Untersuchungen habe ich die Grundsätze guter wissenschaftlicher Praxis, wie sie in der "Satzung der Justus-Liebig-Universität Gießen zur Sicherung guter wissenschaftlicher Praxis" niedergelegt sind, eingehalten.

(J.A. Bonnet)

Ort

Datum

Unterschrift